ADVANCED ELECTRIC PROPULSION RESEARCH

prepared for

NATIONAL AERONAUTICS AND SPACE ADMINISTRATION

GRANT NGR06-002-032

REPORT NO. 3

SPACE PROPULSION PROGRAM

ENERGY CONVERSION PROGRAM

COLLEGE OF ENGINEERING

COLORADO STATE UNIVERSITY

FORT COLLINS, COLORADO

MER 66-67WRM-6

MASSACHUSETTS INSTITUTE OF TECHNOLOGY

RESEARCH LABORATORY OF ELECTRONICS

QUARTERLY PROGRESS REPORT No. 63

October 15, 1961

Submitted by: H. J. Zimmermann
G. G. Harvey
W. B. Davenport, Jr.

ANNUAL REPORT

For the period January 1, 1966 to December 31, 1966

ADVANCED ELECTRIC PROPULSION RESEARCH

Prepared for

NATIONAL AERONAUTICS AND SPACE ADMINISTRATION

January 1967

Grant NGR06-002-032

Technical Management

James Lazar
Chief, Electric Thruster Systems
Nuclear Electric Systems
Office of Advanced Research and Technology
NASA Headquarters
Washington, D. C. 20546

Prepared by: William R. Mickelsen

W. R. Mickelsen, principal investigator
Professor of Mechanical Engineering
and Professor of Electrical Engineering
Engineering Center
Colorado State University
Fort Collins, Colorado 80521

CONTENTS

ELECTRIC PROPULSION FOR PAYLOAD TRANSPORT FROM MOON TO EARTH

by W. R. Mickelsen and T. D. Fehr

A number of Earth-Moon mission profiles with combinations of high-thrust and low-thrust propulsion systems have been explored for their effect on payload capacity. Round trip performance for various mission profiles were investigated in terms of payload to the Lunar surface and payload returned to Earth orbit. The electric propulsion phases of the mission profiles were evaluated for constant thrust-to-mass ratio utilizing a modified Sauer-Melbourne correlation, and for constant thrust utilizing the Zola characteristic length method.

For payloads delivered to the Moon with electric propulsion starting from a low parking orbit at Earth, electric spacecraft would be superior to all-chemical propulsion if the electric-propulsion system specific mass is less than 44 lb/Kwj for one-way trips and less than 55 lb/Kwj for multiple round trips. These results are in agreement with previous literature.

For payloads delivered to Earth from the Moon in 100 days, electric spacecraft would be superior to all-chemical propulsion if the electric-propulsion system specific mass is less than 66 lb/Kwj. These results have significance in analysis of electric propulsion missions for economic uses of the Moon.

A new mission profile has been found in this study which includes a hovering maneuver above the lunar surface. This profile appears to be feasible if low-specific-impulse electric thruster systems can be developed.

Complete details of these analyses have been reported [1.1]. Only the analysis of the mission for payloads delivered to Earth from the Moon is described here.

Constant-Thrust Mission Analysis

The transfer from a specified Earth satellite orbit to a specified Lunar satellite orbit is a restricted three-body problem. An exact analytic solution to this problem is not available and the better approximations require considerable computer time. However, for the purpose of preliminary mission analysis, this degree of accuracy is not required to obtain acceptable results. Therefore, the approximate method [1.2, 1.3] of the Zola characteristic length has been used in this analysis. Constant-thrust trajectories were assumed so the analysis could be done with relative ease.

Validity of the Zola characteristic length method has been verified [1.1] by comparison of results with those of a more exact analysis [1.4]. This comparison was made for one-way missions for transporting payloads from Earth to the Moon. The launch vehicle was assumed to be the Saturn V which boosts 220,000 lb into a 300 n.m. parking orbit at Earth. Electric spacecraft then propel the payload to a 50 n.m. parking orbit at the Moon. Calculations of the payload mass delivered to Lunar parking orbit were made using the Zola characteristic length method. These calculations are compared with the results of the more exact analysis in the following table:

Propulsion System Specific Mass, kg/kwj (lbm/kwj)	Payload into Lunar-Parking Orbit, lb	
	Reference 1.4	Present Analysis
9.06 (20)	138,000	134,000
13.6 (30)	125,000	123,000
18.1 (40)	116,000	113,000

The agreement between these two sets of results is excellent, and it is concluded that the Zola characteristic length method is adequate for approximate analyses of Lunar missions.

Characteristic length L for Earth-Moon transfers can be determined from the relation:

$$L = (JT^3/16)^{\frac{1}{2}} \tag{1.1}$$

Where J is Melbourne's parameter [1.5], and T is trip time. The parameter J is defined by:

$$J = \int_0^T (F/M)^2 \, dt \tag{1.2}$$

In the present analysis, the value of J was found from a modified version of the Sauer-Melbourne correlation [1.6].

Stephenson [1.7] has used a correction factor of 0.92 to trip times, and found that calculations of Earth escape trajectories by London [1.8] could be used to determine payloads for Earth-parking to Lunar-parking orbit transfers. This same correction factor of 0.92 has been used in the present analysis to convert the Sauer-Melbourne escape-trajectory correlation to an Earth-Moon transfer.

The modified Sauer-Melbourne correlation which relates J to escape time T_e is:

$$J = K' T_e^{-0.913} \tag{1.3}$$

The coefficient K' is a function of radius r_p of the central body, radius r_o of the starting orbit, gravitational acceleration g_p at the central body surface, and the force constant μ_p of the central body:

$$K = .394\, g_p^2 \left(\frac{r_p}{r_o}\right)^4 \left(\frac{r_o}{\sqrt{\mu_p / r_o}}\right)^{1.913} \tag{1.4}$$

When the Stephenson correction is used, then $T_p = 0.92\, T_e$ and a new constant K can be defined which absorbs the factor 0.92 (ie, $K = K'/.92^{.913}$):

$$J = K T_p^{-0.913} \tag{1.5}$$

Where T_p is the time spent in the field of the central body. In this way, the total J and total T for the Earth-Moon transfer are:

$$T = T_E + T_M \tag{1.6}$$

$$J = J_E + J_M \tag{1.7}$$

Where the subscripts E and M refer to Earth and Moon respectively. Noting that for a maximum final mass fraction:

$$dJ = dJ_E + dJ_M = 0 \tag{1.8}$$

and that for a fixed transit time:

$$dT = dT_E + dT_M = 0 \tag{1.9}$$

By combining equations (1.8) and (1.9):

$$\frac{dJ_E}{dT_E} = \frac{dJ_M}{dT_M} \tag{1.10}$$

Equations (1.5) and (1.10) can be used to obtain the ratio of T_M/T_E:

$$T_M/T_E = (K_M/K_E)^{0.523} \tag{1.11}$$

Total J can be defined by combining equations (1.5) and (1.7):

$$J = K_E T_E^{-0.913} + K_M T_M^{-0.913} \tag{1.12}$$

This expression can be combined with equation (1.10) to obtain:

$$J = \left[1 + (K_M/K_E)^{0.523}\right]^{1.913} K_E T^{-0.913} \tag{1.13}$$

For a 300 n.m. Earth parking orbit, and a 50 n.m. Lunar parking orbit, equation (1.13) becomes:

$$J = KT^{-0.913} \tag{1.14}$$

where J has the units watts/kg, T is in seconds, and $K = 1.81 \times 10^7$. Characteristic length L can be calculated from equation (1.1) by using values of J found from equation (1.14) for various values of T. Results of these calculations are shown in Figure 1.1.

Analysis of an Earth-Moon transfer can begin by specifying a starting mass M_o in Earth parking orbit, by specifying a transfer time T, and by specifying a specific impulse I. The expression for initial thrust-to-mass ratio F/M_o is[1.2]:

$$\frac{F}{M_o} = \frac{4L}{T^2} \frac{v^2}{(v + L/T)^2} \tag{1.15}$$

where v is effective exhaust velocity defined by:

$$v = g_c I$$

where g_c is the gravitational conversion factor (9.806 m/sec^2). Characteristic velocity ΔV can be calculated from [1.2]:

$$\Delta V = 2v \ln\left(\frac{v + L/T}{v - L/T}\right) \tag{1.16}$$

Final mass fraction for the constant-thrust Earth-Moon transfer is:

$$M_f/M_o = \exp(-\Delta V/v) \tag{1.17}$$

where M_f is the mass delivered to Lunar parking orbit. For maximum payload, the final mass fraction is[1.5]:

$$M_f/M_o = 1 - \beta \tag{1.18}$$

The parameter β is[1.5]:

$$\beta = (\alpha J/2)^{\frac{1}{2}} \tag{1.19}$$

where α is the specific mass (kg/watt) of the electric propulsion system. Since M_f/M_o and J are known from the preceding analysis, then the value of α can be found from combining equations (1.18) and (1.19):

$$\alpha = (1 - M_f/M_o)^2 (2/J) \tag{1.20}$$

In other words, this is the value of α necessary to satisfy the conditions of maximum payload and specified M_o, T, and I. Initial power-to-mass ratio

P/M_o can be found from:

$$P/M_o = (F/M_o)(v/2) \tag{1.21}$$

so that the propulsion-system mass fraction M_{ps}/M_o is simply the product of α and P/M_o:

$$M_{ps}/M_o = \alpha\,(F/M_o)(v/2) \tag{1.22}$$

One-way transfers from Earth-parking to Lunar-parking orbit can be calculated by the following procedure:

1. Specify M_o, T, and I.
2. Find L from Figure 1-1.
3. Calculate ΔV from equation (1.16).
4. Calculate M_f from equation (1.17).
5. Calculate F/M_o from equation (1.15).
6. Calculate α from equation (1.20)
7. Calculate M_{ps}/M_o from equation (1.22)

Mass M_L delivered to Lunar parking orbit is the difference between M_f and M_{ps} :

$$M_L = M_f - M_{ps} \tag{1.23}$$

If this is as far as the mission goes, then M_L is the payload into Lunar-parking orbit. For example, the tabulation at the beginning of this section listed values of M_L for several values of α. As noted previously, the method outlined above provides results that are in close agreement with a more accurate analysis.

Analysis of Payload Transport from Moon to Earth

Potential performance of electric spacecraft for transporting payloads from the Lunar surface to Earth can be studied by assuming various mission profiles. As an initial step in this examination, the following profile was assumed:

1. The Saturn V boosts M_o = 220,000 lb. into a 300 n.m. Earth parking orbit. The mass M_o consists of:

(a) electric propulsion system of mass M_{ps} which includes powerplant, thruster, tank, and structures. This propulsion system performs the transfers from Earth-parking to Lunar-parking orbit, and return.

(b) propellant mass $M_{pr,o}$ for the outbound transfer from 300 n.m. Earth-parking to 50 n.m. Lunar-parking orbit with the constant-thrust electric propulsion system

(c) a Lunar-lander chemical rocket of mass M_c = 7,500 lb. which includes a chemical-rocket engine, structure, and tank; the lander has a specific impulse of 300 sec.

(d) propellant mass $M_{c,d}$ for the chemical-rocket lander descent from 50 n.m. Lunar-parking orbit to the Lunar surface; for descent, ΔV = 1.72 km/sec.

(e) propellant mass $M_{c,a}$ for the chemical-rocket lander ascent from the lunar surface to the 50 n.m. Lunar-parking orbit; for ascent, ΔV = 1.72 km/sec.

(f) propellant mass $M_{pr,R}$ for the return transfer from 50 n.m. Lunar-parking to 300 n.m. Earth-parking orbit with the constant-thrust electric propulsion system.

2. Upon arrival in the 50 n.m. Lunar-parking orbit, the electric propulsion system of mass M_{ps} and return-transfer propellant of mass $M_{pr,R}$ remain in the Lunar-parking orbit awaiting the payload.

3. Upon arrival in the 50 n.m. Lunar-parking orbit, the chemical-rocket lander descends to the Lunar surface, acquires the payload mass M_{pay}, and ascends to rendezvous with the waiting electric spacecraft.

4. After rendezvous, the chemical-rocket lander remains in Lunar-parking orbit.

5. After acquiring the payload mass M_{pay}, the electric spacecraft of total mass M_R transfers from 50 n.m. Lunar-parking to 300 n.m. Earth-parking orbit.
6. Final mass delivered to Earth-parking orbit is the electric propulsion system mass M_{ps} and the payload mass M_{pay}.
7. Delivery of payload mass to Earth surface is done by atmospheric entry methods, which are assumed to involve negligible mass.
8. If multiple round-trips are to be made, and if the electric propulsion system has adequate durability, then subsequent boosters would not have to carry the masses M_{ps} and M_c, thereby allowing greater payloads delivered to Earth.

Analysis of this mission can be based on two mass summations:

$$M_o = M_{ps} + M_{pr,o} + M_c + M_{c,d} + M_{c,a} + M_{pr,R} \tag{1.24}$$

$$M_R = M_{pay} + M_{ps} + M_{pr,R} \tag{1.25}$$

Propellant masses $M_{c,d}$ and $M_{c,a}$ for the lander can be determined with the standard rocket equation for propellant mass fraction b:

$$b = 1 - \exp(-\Delta V_M/v_L) \tag{1.26}$$

For $\Delta V_M = 1.723$ km/sec (either descent or ascent), and a chemical rocket specific impulse of 300 sec, $b = .444$. Propellant masses $M_{c,d}$ and $M_{c,a}$ are:

$$M_{c,d} = b(M_c + M_{c,a}) \tag{1.27}$$

$$M_{c,a} = b(M_c + M_{pay}) \tag{1.28}$$

The other masses in equations (1.24) and 1.25) can be determined from:

$$M_{ps} = \frac{\alpha v}{2} F \tag{1.29}$$

$$M_{pr,o} = \frac{T_o}{v} F \tag{1.30}$$

$$M_{pr,R} = \frac{T_R}{v} F \tag{1.31}$$

where α is the specific mass of the electric propulsion system (kg/watt), v is the effective exhaust velocity of the electric thruster ($v = g_c I$, m/sec), F is thrust (newtons), T_o is outbound transfer time, and T_R is return transfer time. Equations (1.27) to (1.31) can be used in equations (1.24) and (1.25) to obtain:

$$\frac{M_{pay}}{M_o} = \frac{1-(1-b)^2 M_c/M_o}{b(1+b)} - \left(\frac{\alpha v/2 + T_o/v + T_R/v}{b(1+b)}\right)\frac{F}{M_o} \tag{1.32}$$

$$\frac{M_{pay}}{M_o} = \left(\frac{1}{F/M_R} - \frac{\alpha v}{2} - \frac{T_R}{v}\right)\frac{F}{M_o} \tag{1.33}$$

Thrust-to-mass ratios F/M_R and F/M_o can be determined from equations (1.1), (1.5), and (1.15):

$$\frac{F}{M_o} = \frac{K^{\frac{1}{2}} v^2}{T_o .952 (v + K^{\frac{1}{2}} T_o .048/4)^2} \tag{1.34}$$

$$\frac{F}{M_R} = \frac{K^{\frac{1}{2}} v^2}{T_R .952 (v + K^{\frac{1}{2}} T_R .048/4)^2} \tag{1.35}$$

With equations (1.34) and (1.35), the two payload equations (1.32) and (1.33) can be equated to form a relation between the two transfer times T_o and T_R:

$$T_R\left[\frac{(v + K^{\frac{1}{2}} T_R .048/4)^2}{K^{\frac{1}{2}} v T_R .048} + .56\right] = T_o\left[\frac{1.54(v + K^{\frac{1}{2}} T_o .048)^2}{K^{\frac{1}{2}} v T_o .048} - 1.56\right] - .28\alpha v^2 \tag{1.36}$$

Functions $f(T_R)$ and $f(T_o)$ can be defined to replace the respective terms containing T_R and T_o in equation (1.36) so that:

$$f(T_R) = f(T_o) - .28\alpha v^2 \tag{1.37}$$

The functions $f(T_R)$ and $f(T_o)$ are plotted in Figures 1.2 and 1.3 respectively for a range of specific impulse, I.

With the preceding relations and graphs, the payload mass M_{pay} can be found for specified values of M_o, v, α, and T_o. Calculation procedure is as follows:

1. For specified time T_o, find $f(T_o)$ from Figure 1.3.
2. For specified v and α, and with $f(T_o)$, calculate $f(T_R)$ from equation (1.37).
3. With calculated $f(T_R)$, find T_R from Figure 1.2.
4. Calculate F/M_o and F/M_R from equations (1.34) and (1.35) respectively.
5. Calculate M_{pay}/M_o from equation (1.33).
6. Total mission time is $T = T_o + T_R$

Typical results obtained with this procedure are shown in Figure 1.4. As expected, there is an optimum specific impulse for each combination of propulsion-system specific mass α, and trip time T. Also notable is the sensitivity of payload fraction to off-optimum specific impulse.

The effect of propulsion-system specific mass on payload transport from Moon to Earth is shown in Figure 1.5. Also shown in this figure is the payload capacity of an all-chemical-rocket transport, having a specific impulse of 300 seconds. By comparison, it is evident that electric spacecraft would be superior to all-chemical-rocket spacecraft for 100-day missions if the electric-propulsion-system specific mass is less than 66lb/kwj.

All results shown here have been calculated by hand, so their accuracy is not good, particularly for the short trip times. Multiple round trips with a given electric spacecraft are of interest in assessing the economic

advantages of Moon-to-Earth transport. For acceptable accuracy in this further multiple-round-trip analysis, greater accuracy in calculation will be required. A fast and simple digital computer program will be written to serve these needs.

REFERENCES

1.1 Fehr, T.D.: Electric Propulsion for Lunar Missions. Master of Science Thesis, Colorado State University, December, 1966. (Printed in entirety in Report No. 2, Space Propulsion Program, Colorado State University, as a part of NASA Grant NGR06-002-032. November 22, 1966.)

1.2 Zola, C.L.: Trajectory Methods in Mission Analysis for Low-Thrust Vehicles. AIAA Paper No. 64-51. January, 1964.

1.3 Zola, C.L.: A Method of Approximating Propellant Requirements of Low-Thrust Trajectories. NASA TN D-3400. April, 1966.

1.4 Larson, J.W.: Electrically-Propelled Cargo Vehicle for Sustained Lunar Supply Operations. General Electric, Missile and Space Division Report 655 D 4361. June 28, 1965.

1.5 Melbourne, W.G.: Interplanetary Trajectories and Payload Capabilities of Advanced Propulsion Vehicles. TR 32-68, Jet Propulsion Laboratory, California Institute of Technology. March, 1961.

1.6 Sauer, C.G. and Melbourne, W.G.: Optimum Earth-to-Mars Roundtrip Trajectories Utilizing a Low-Thrust Power-Limited Propulsion System. TR 32-376, Jet Propulsion Laboratory, California Institute of Technology. March, 1963.

1.7 Stephenson, R.R.: The Electrically Propelled Lunar Logistic Vehicle. AIAA Paper No. 64-497. July, 1964.

1.8 London, H.S.: A Study of Earth-Satellite to Moon-Satellite Transfers Using Nonchemical Propulsion Systems. United Aircraft Corporation Report R-1383-1. May, 1964.

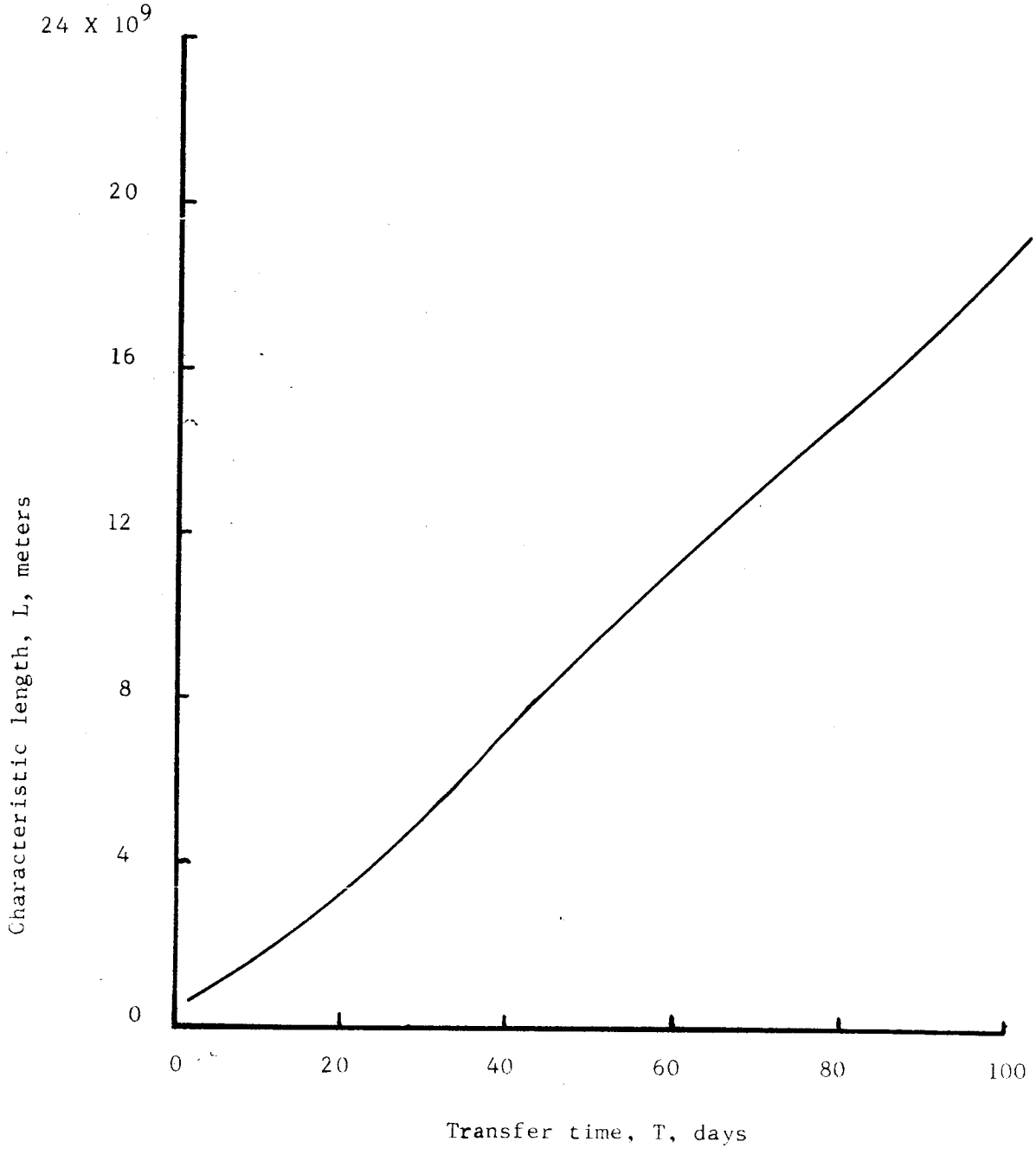

Figure 1.1. Characteristic length for constant-thrust transfer from 300 n.m. Earth parking orbit to 50 n.m. Lunar parking orbit. (Calculated from modified Sauer-Melbourne correlation).

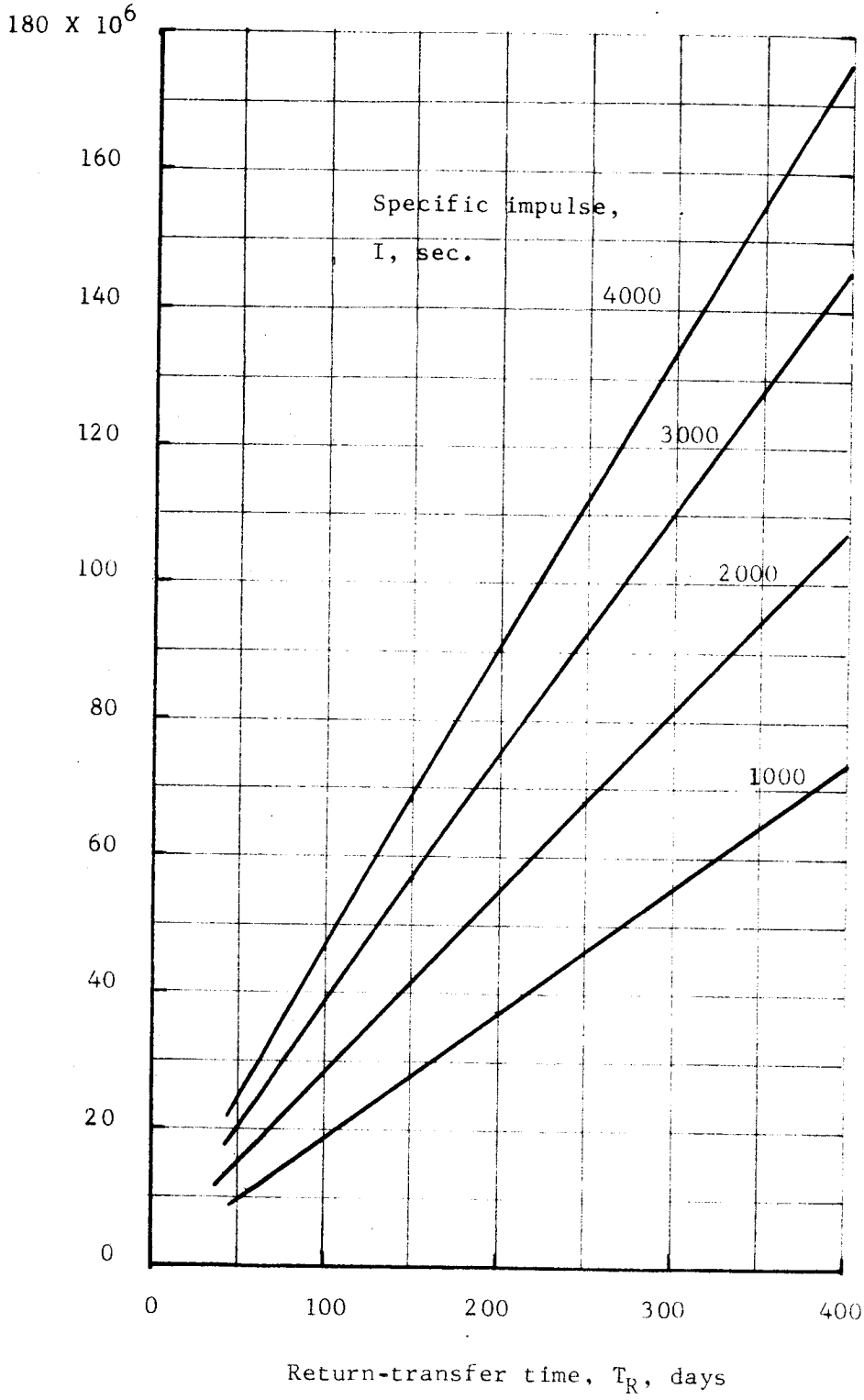

$$f(T_R) = T_R \left[\frac{(v + K^{\frac{1}{2}} T_R^{.048}/4)^2}{K^{\frac{1}{2}} v T_R^{.048}} + .56 \right] \text{, seconds}$$

Figure 1.2. Function $f(T_R)$ for return-transfer time from 50 n.m. Lunar-parking orbit to 300 n.m. Earth-parking orbit.

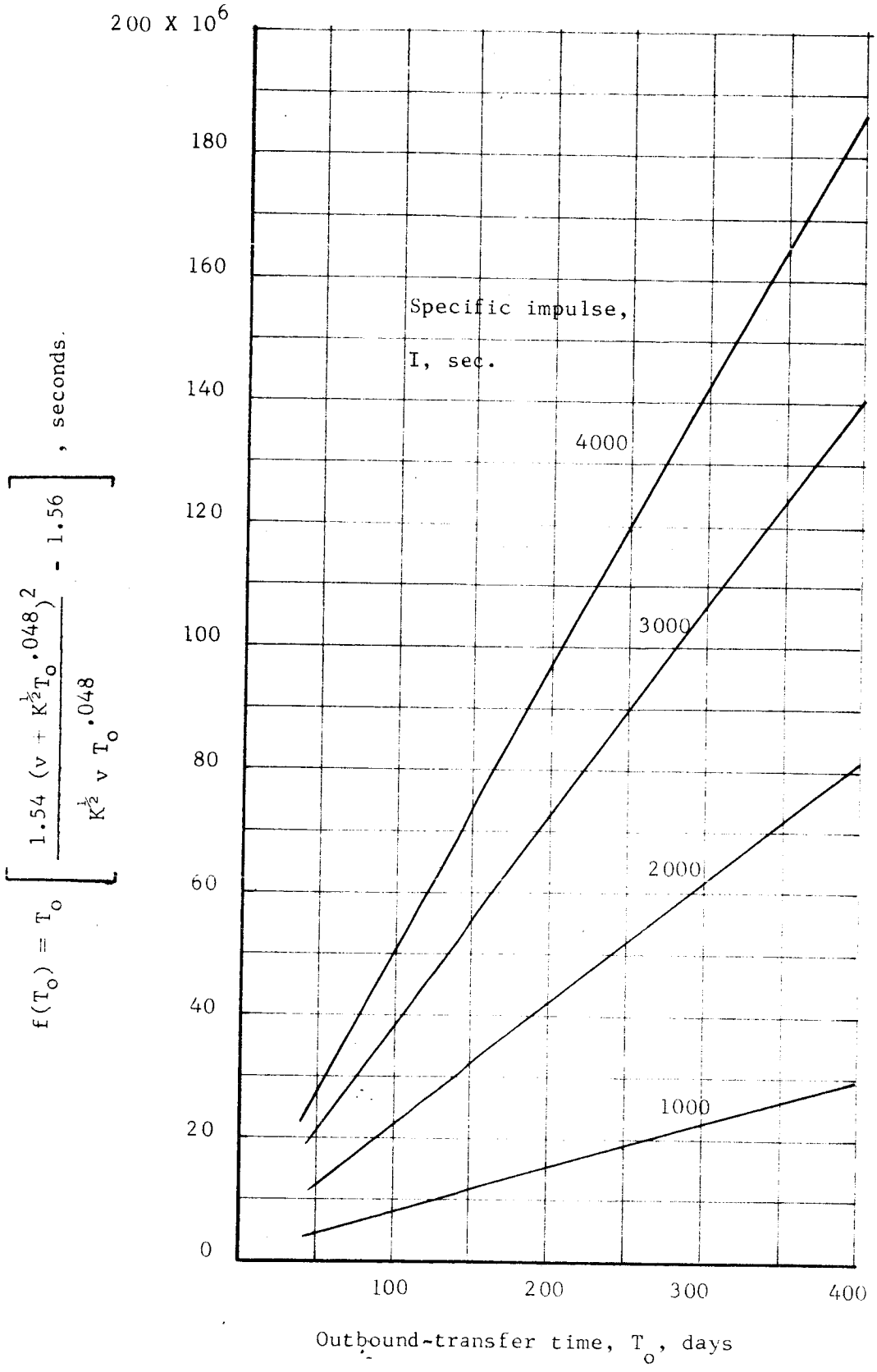

Figure 1.3. Function $f(T_o)$ for outbound transfer time from 300 n.m. Moon-parking orbit to 50 n.m. Earth-parking orbit.

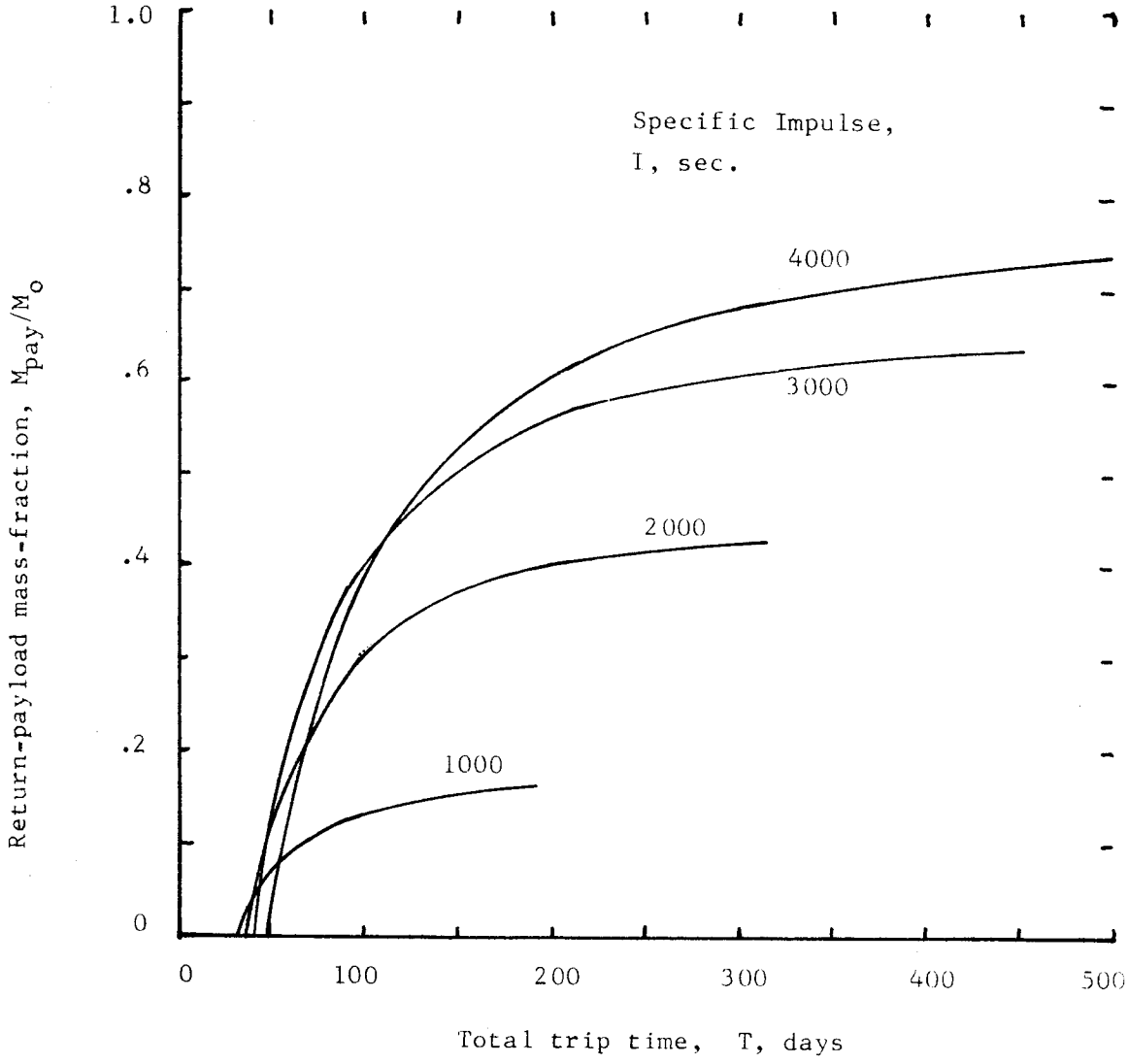

(a) Electric-propulsion-system specific mass, α 22 lb/Kwj

Figure 1.4. Payload mass-fractions for payload transferred from Moon to Earth with electric spacecraft. Earth-parking orbit, 300 n.m., Lunar-parking orbit, 50 n.m. Lander chemical rocket; 7500 lb, 300 sec. specific impulse

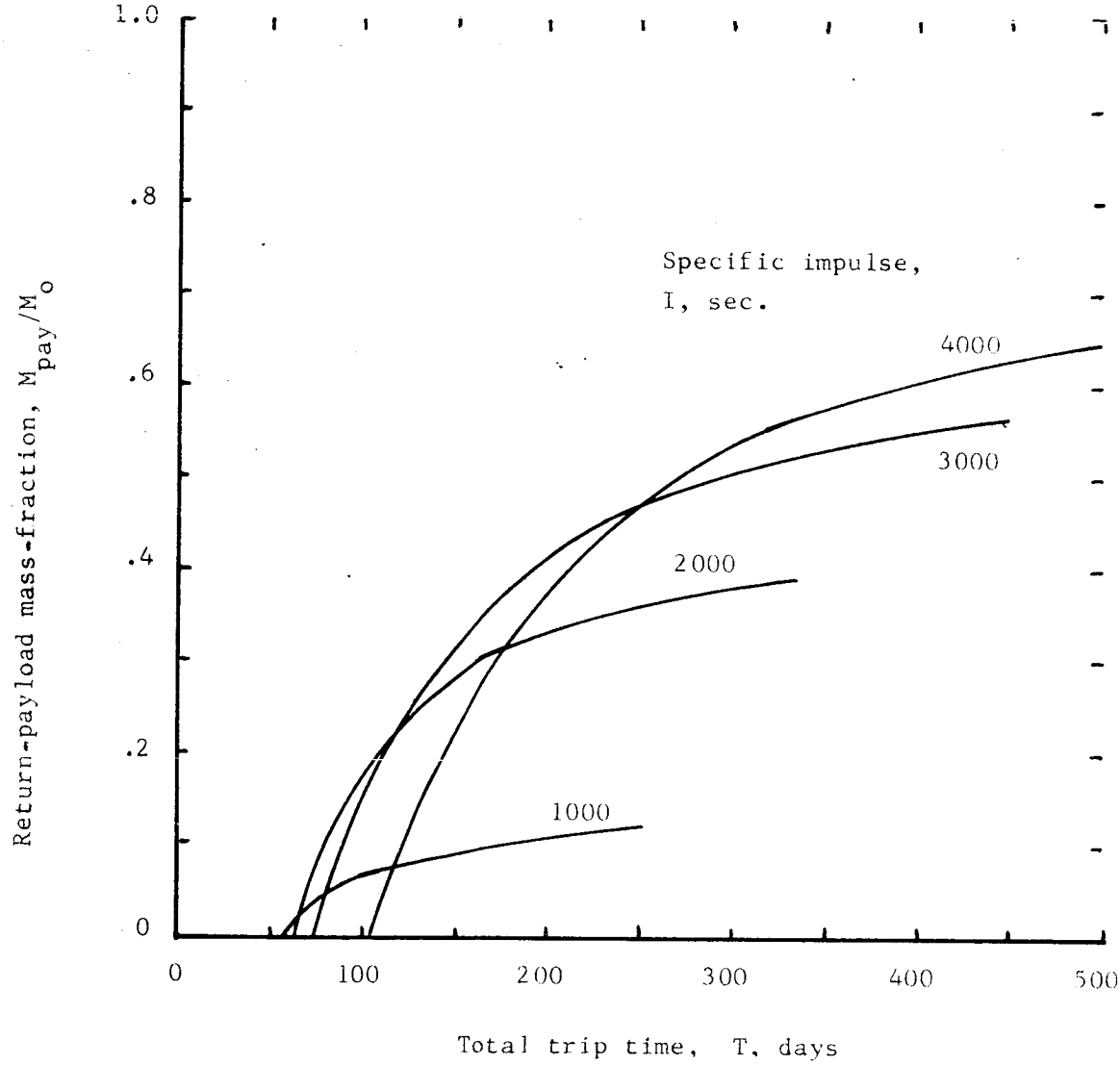

(b) Electric-propulsion-system specific mass, α = 44.1 lb/Kwj

Figure 1.4. continued

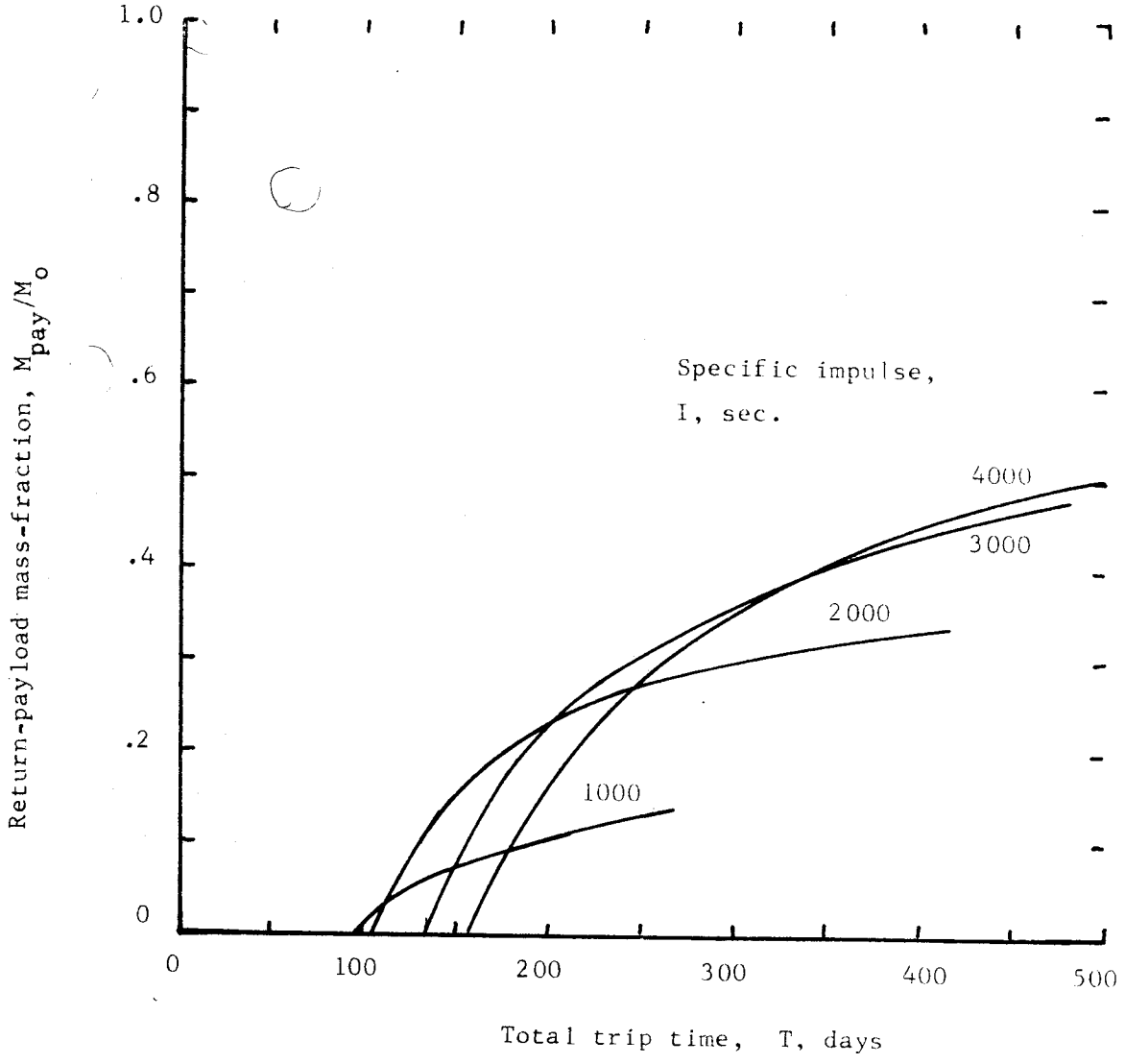

(c) Electric-propulsion-system specific mass, α = 66.2 lb/Kwj

Figure 1.4. continued

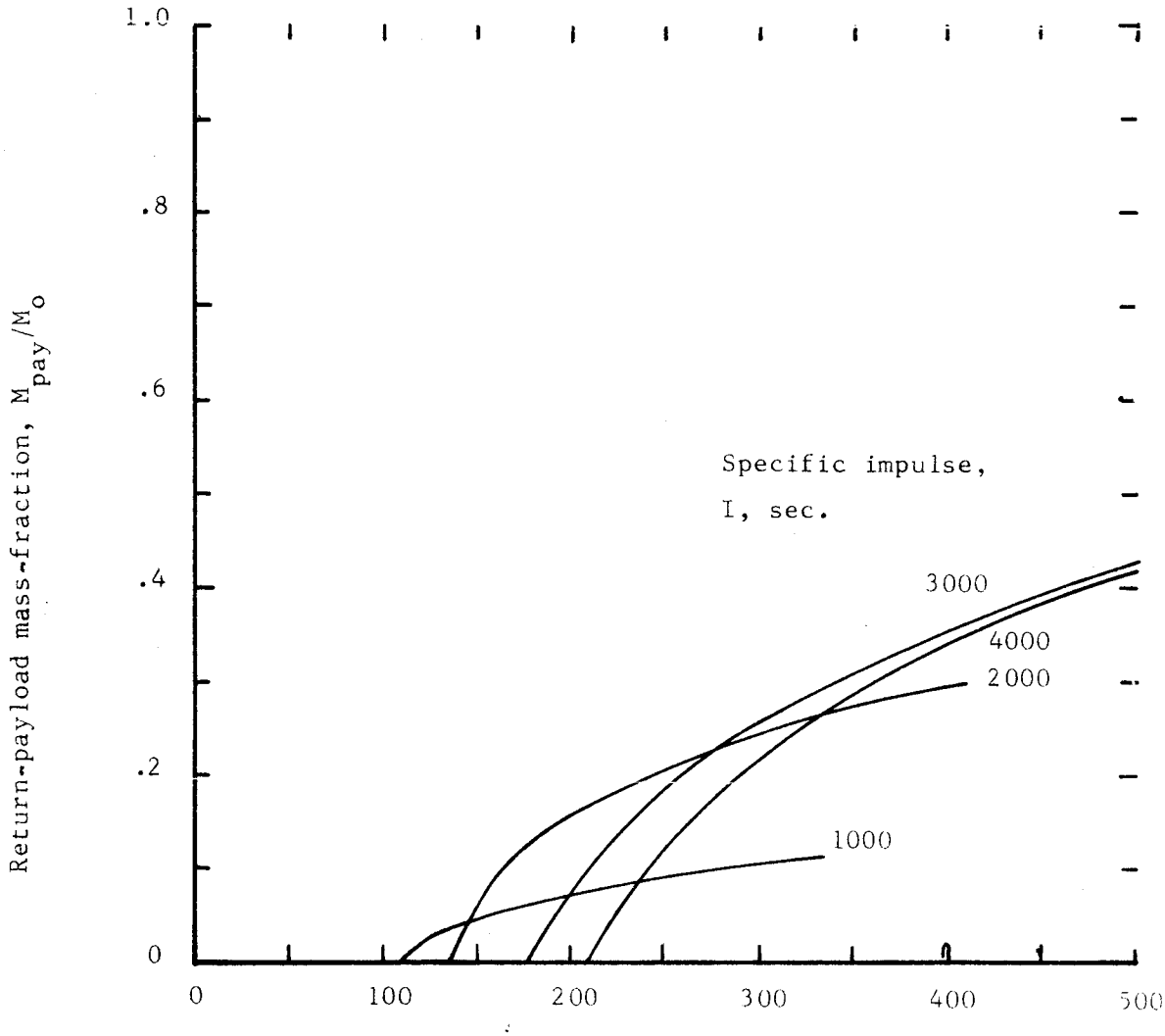

(d) Electric-propulsion-system specific mass, α = 88.2 lb/Kwj

Figure 1.4. continued

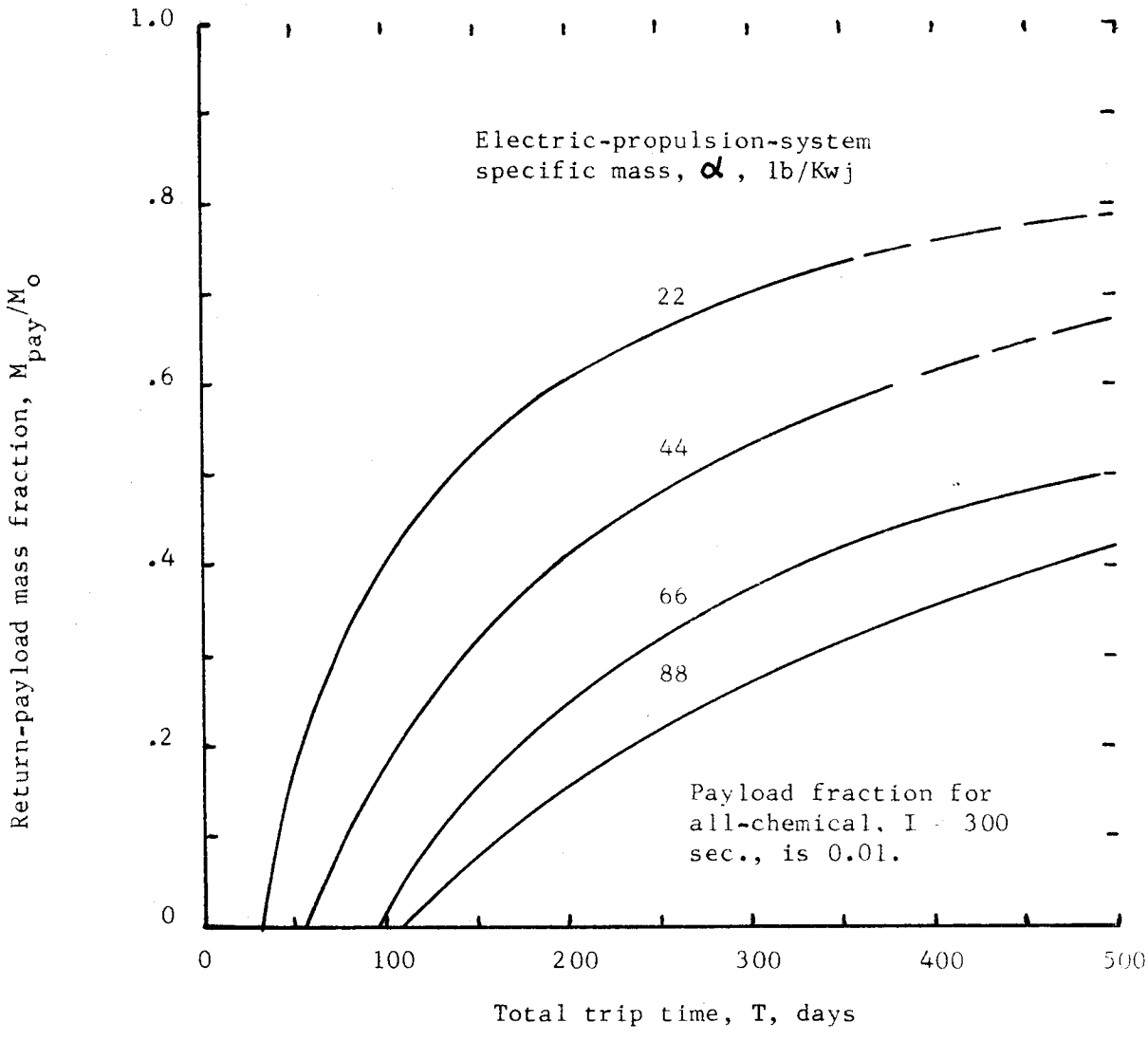

Figure 1.5. Effect of electric-propulsion-system specific mass on payloads transferred from Moon to Earth. Under chemical rocket; 7500 lb., 300 sec. specific impulse.

RADIOISOTOPE HEATING OF CONTACT IONIZERS

by W.R. Mickelsen

The use of radioisotopes for heating ionizers in contact-ionization thrusters has been suggested at least as early as March, 1963.* More recently, the subject has been raised again, with the intent of improving the performance of the contact-ionization thruster with respect to the mercury-discharge and cesium-discharge thrusters. Feasibility and possible gains in performance can be assessed on simple and fundamental grounds as described in the following analysis.

Required power levels are of first importance because radioisotope production is limited. Annual production rates of most radioisotopes is related directly to nuclear-electric power generation, since most radioisotopes are fission products. Electric-spacecraft effective jet power $P_{j,eff}$ is directly related to three basic parameters, the spacecraft starting mass M_o, the electric-propulsion-system effective specific mass α_{ps}^*, and the electric-propulsion-system mass-fraction M_{ps}/M_o:

$$P_{j,eff} = M_o \, (1/\alpha_{ps}^*) \, (M_{ps}/M_o) \qquad (1)$$

Effective specific mass α_{ps}^* has been defined by Mickelsen[1].

Melbourne[2] has shown that the propulsion-system mass-fraction M_{ps}/M_o is approximately constant for nearly all missions of interest. This constancy can be shown by use of a parameter β which is defined as:

$$\beta^2 \equiv (\alpha_{ps}^*/2) \int_o^\tau (F/M)^2 \, dt \qquad (2)$$

---

* suggested by Dr. David B. Langmuir, TRW Systems, Redondo Beach, to W.R. Mickelsen while walking into the Broadmoor Hotel on or about March 11, 1963, while attending the AIAA Electric Propulsion Conference, Colorado Springs.

The definite integral of the square of the instantaneous thrust/mass ratio is a measure of trajectory difficulty, and its value also depends on the thrust program. Melbourne showed that payload fraction M_{pay}/M_o is related to β and M_{ps}/M_o as follows:

$$M_{pay}/M_o = (M_{ps}/M_o)\left[\frac{1}{\beta^2 + (M_{ps}/M_o)} - 1\right] \qquad (3)$$

This equation is represented by the following figure:

Fig. 1

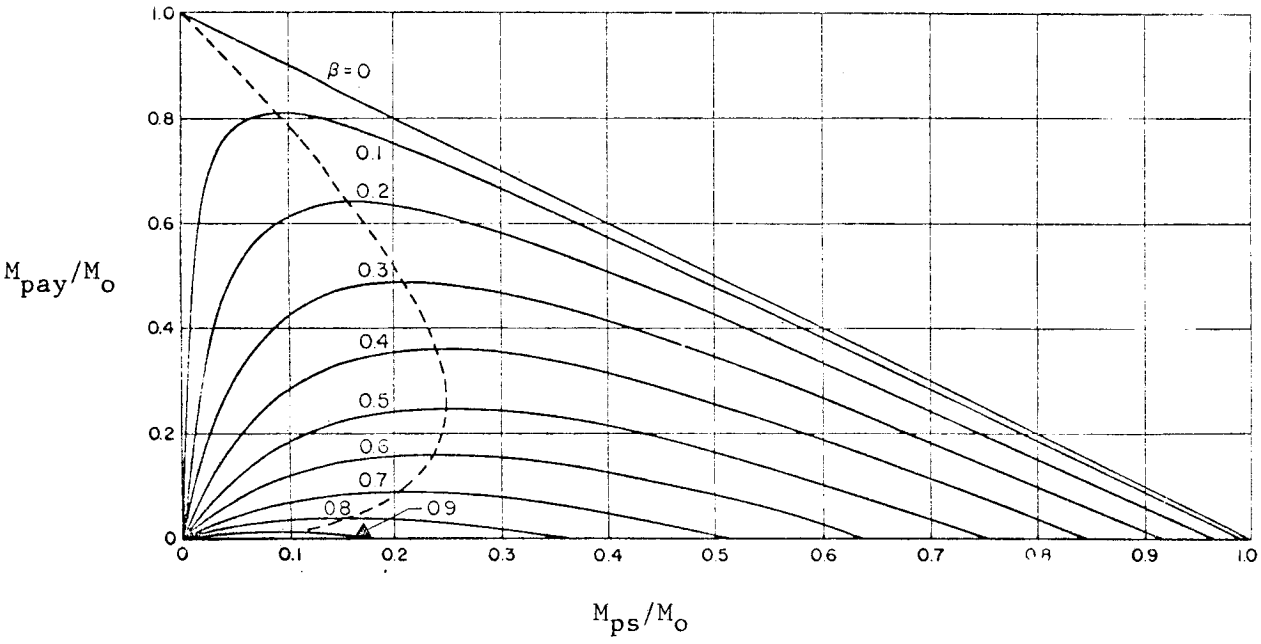

From inspection of this figure, it is evident that the propulsion-system mass-fraction M_{ps}/M_o will have optimum values of 0.2 to 0.25 for all missions where the payload fraction M_{pay}/M_o has values between 0.1 and 0.5. The relationships shown in the figure above are fundamental to all electric-propulsion missions, irregardless of the type of thrust program, whether hyperbolic boost is used or not, etc. Because of the fundamental nature of these relationships,

it can be said that the propulsion-system mass-fraction is universally about 0.2.

Electric-spacecraft starting mass M_o will depend on the type of booster, and on whether hyperbolic boost is used. For example, Saturn V and Saturn V/Centaur payloads are shown in the following figures as function of hyperbolic velocity with respect to Earth (ie, boost beyond escape):

Fig. 2

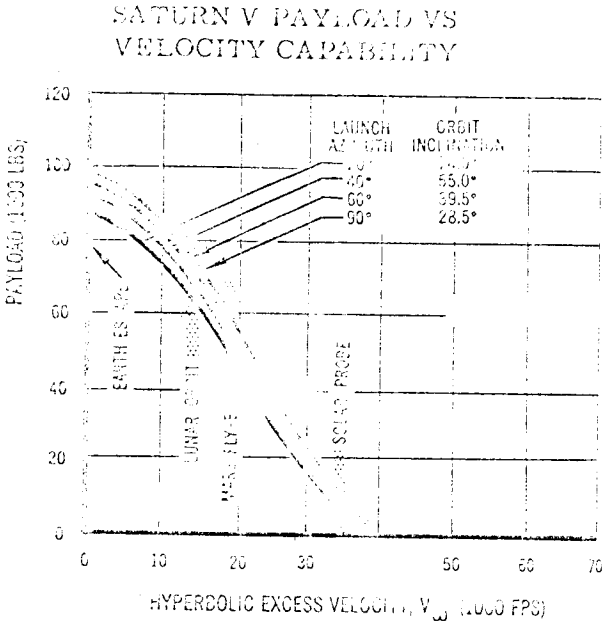

Fig. 3

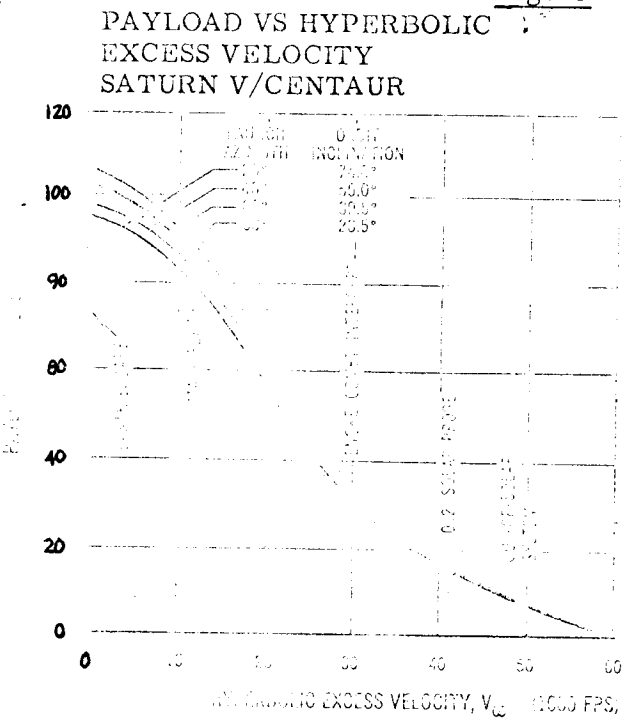

From inspection of these figures it appears that electric spacecraft starting mass could be from 20,000 lb. to 100,000 lb.

In addition to this wide range of possible starting mass M_o, mission analysis has shown that α^*_{ps} can be in the range from 20 lb/kwj to 120 lb/kwj and still be of interest. From these considerations it appears that electric spacecraft launched with Saturn V-class boosters might have anywhere from 160 to 5,000 kwj. (the notation kwj denotes kilowatts of effective jet power).

Contact-ionization thrusters are operated at the highest current density j commensurate with the required durability of accel electrodes which are eroded by charge-exchange-ions. The best performance of "flight-type" contact-ionization thrusters reported to date[3] is a current density of $j = 170$ amp/m^2. To obtain this current density in the Hughes multi-strip thruster, and accel voltage of $\Phi_A = 13{,}000$ volts is needed. Operation in the specific-impulse range-of-interest requires a very wide range of the ratio Φ_A/Φ_{net}, where Φ_{net} is the net acceleration voltage. This is illustrated by the following figure:

Fig. 4

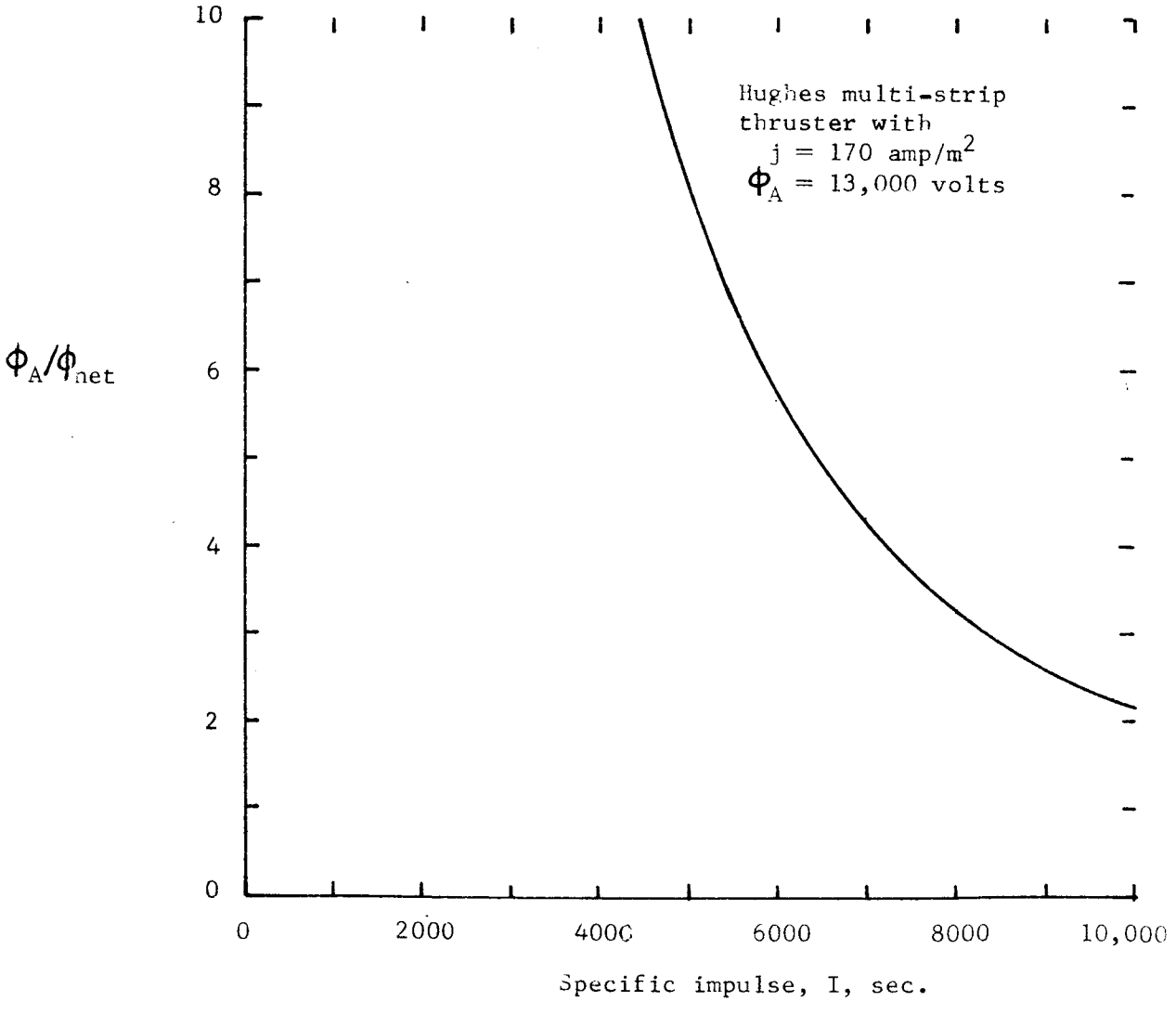

Operation at such high values of ϕ_A/ϕ_{net} is questionable, but it is assumed here that such high values will be found to be feasible. In this way, current density j may be held constant throughout the specific-impulse range-of-interest in order to obtain the highest power-density possible.

Power density $P_{j,eff}/A$ is given by:

$$P_{j,eff}/A = j\,\phi_{net} \tag{4}$$

so that if j is constant, then $P_{j,eff}/A$ is directly proportional to ϕ_{net}. When j is held constant, then ionizer temperature is also constant. Therefore, the heat loss from the ionizer must also be constant. At $j = 170$ amp/m^2, the heat loss per unit ionizer area in the Hughes multi-strip thruster[4] is $\dot{Q}/A = 150$ kw/m^2. With this information, the ratio of heat loss $\dot{Q}$ to jet power $P_{j,eff}$ can be written:

$$\dot{Q}/P_{j,eff} = (\dot{Q}/A) \,/\, (P_{j,eff}/A) = 150{,}000/(170\ \phi_{net})$$
$$= 870/\phi_{net} \tag{5}$$

Net accelerating voltage ϕ_{net} is related to specific impulse, so $\dot{Q}$ can be calculated for various jet-power levels over a range of specific impulse, as shown in the following figure: (the notation kwt denotes kilowatts of thermal power).

Fig. 5

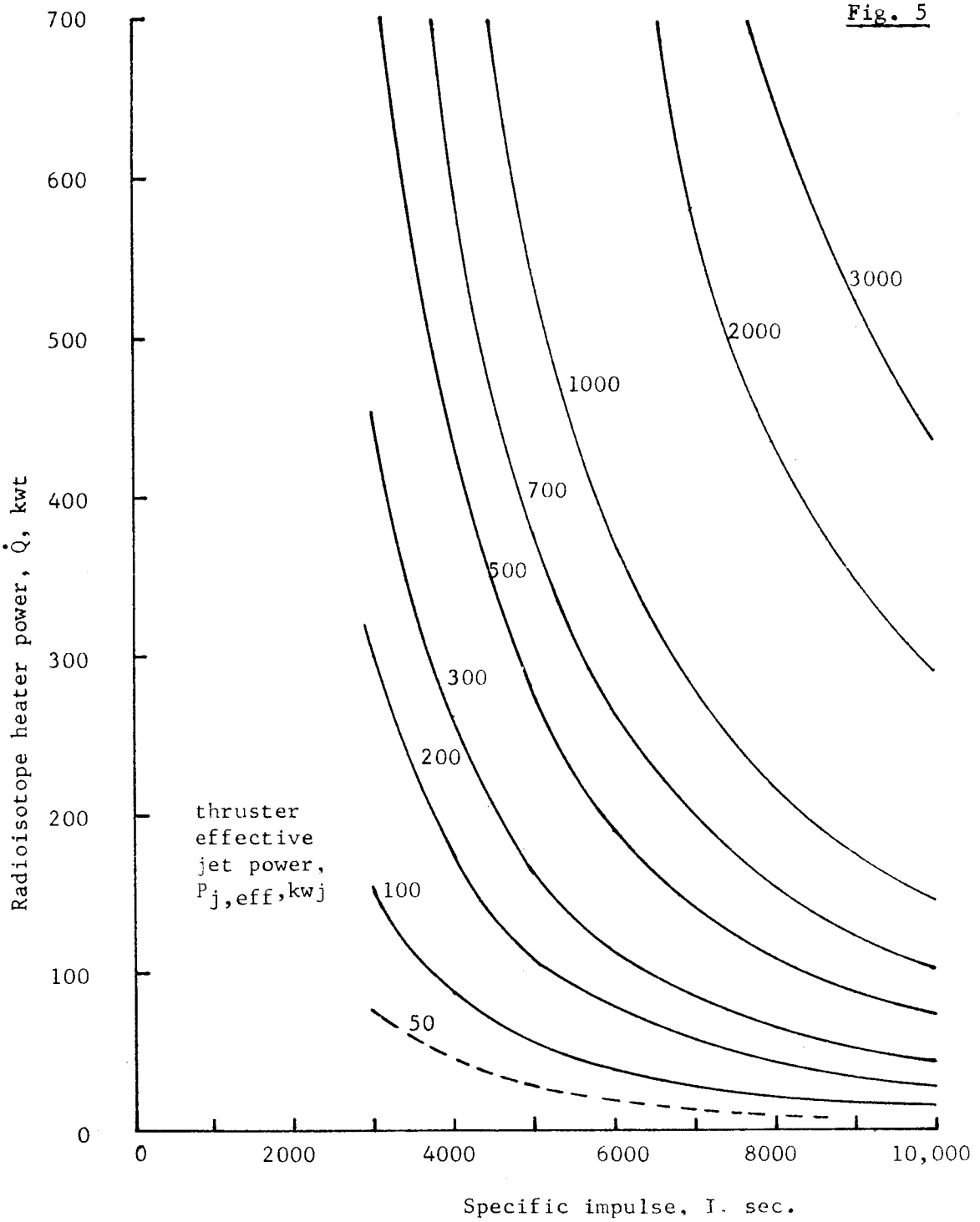

This figure represents the radioisotope-heater power level required for various jet-power levels. Use of radioisotope-heating at low specific impulse will depend on the amount of radioisotope that is available for use in electric propulsion systems.

Radioisotope properties and availability are reported in a number of papers, and some of these [5,6,7] are referenced here. The following table summarizes information about those radioisotopes that have appreciable production rates and that are relatively free from radiation:

TABLE 1

radioisotope	emission	ref.	availability, kwt 1967	1970	1980	sp. vol. cc/kwt	sp. wt. lb/kwt	half-life years
Pm - 147 (Pm_2O_3)	β^- to 0.223Mev	5		9.4	94	1000	12.3	2.6
		6	11			550	8.2	2.7
		7	17	25	111	670	8.2	2.6
Cm-242 (Cm_2O_3)	α^{++} at 6.1Mev	5		1.8	50	0.86	0.0184	0.44
		6				0.87	0.0225	0.45
Cm-244 (Cm_2O_3)	α^{++}	5						
		6				37	0.96	18
Po-210 (metal)	α^{++} at 5.3Mev	5				0.76	0.0157	0.38
		6				0.83	0.0164	0.38
		7	140*	140*		0.83	0.017	0.38
Pu-238 (PuO_2)	α^{++} at 5.5Mev	5		29	53	108	4.6	90
		6				256	5.7	89
		7	13	26	73	200	5.1	89.6

* produced by neutron irradiation of bismuth, and production is estimated on basis of using bismuth coolant in private and public reactors.

If the values in this table are correct, then it appears that the quantity of radioisotope available for electric propulsion will be severely limited. For example, the 1980 production of Pu - 238 will be about 60 kwt, and if 1/3 of this production could be given to electric propulsion then only 20 kwt would be available for radioisotope heating of the ionizer in contact-ionization thrusters. Since Po - 210 is produced by neutron irradiation of bismuth, the annual production rate is uncertain because bismuth would have to be used in great quantities as a reactor coolant in order to achieve the production figures listed in the table. About one inch of lead shielding [6] would be required to reduce Pm - 147 radiation to 10 milli-roengten at one meter from a one kilowatt source. This amount of shielding should pose no great problem in launch operations. Shielding is not required for Pu - 238.

From these considerations it appears that Pm - 147 and Pu - 238 are possible candidates for radioisotope heating of contact ionizers, and the Po - 210 might be a candidate if firm values for annual production rate were known.

Decay rate is an important consideration when half-life is of the order of mission time. Thermal power as a function of time is shown in the next figure.

Fig. 6

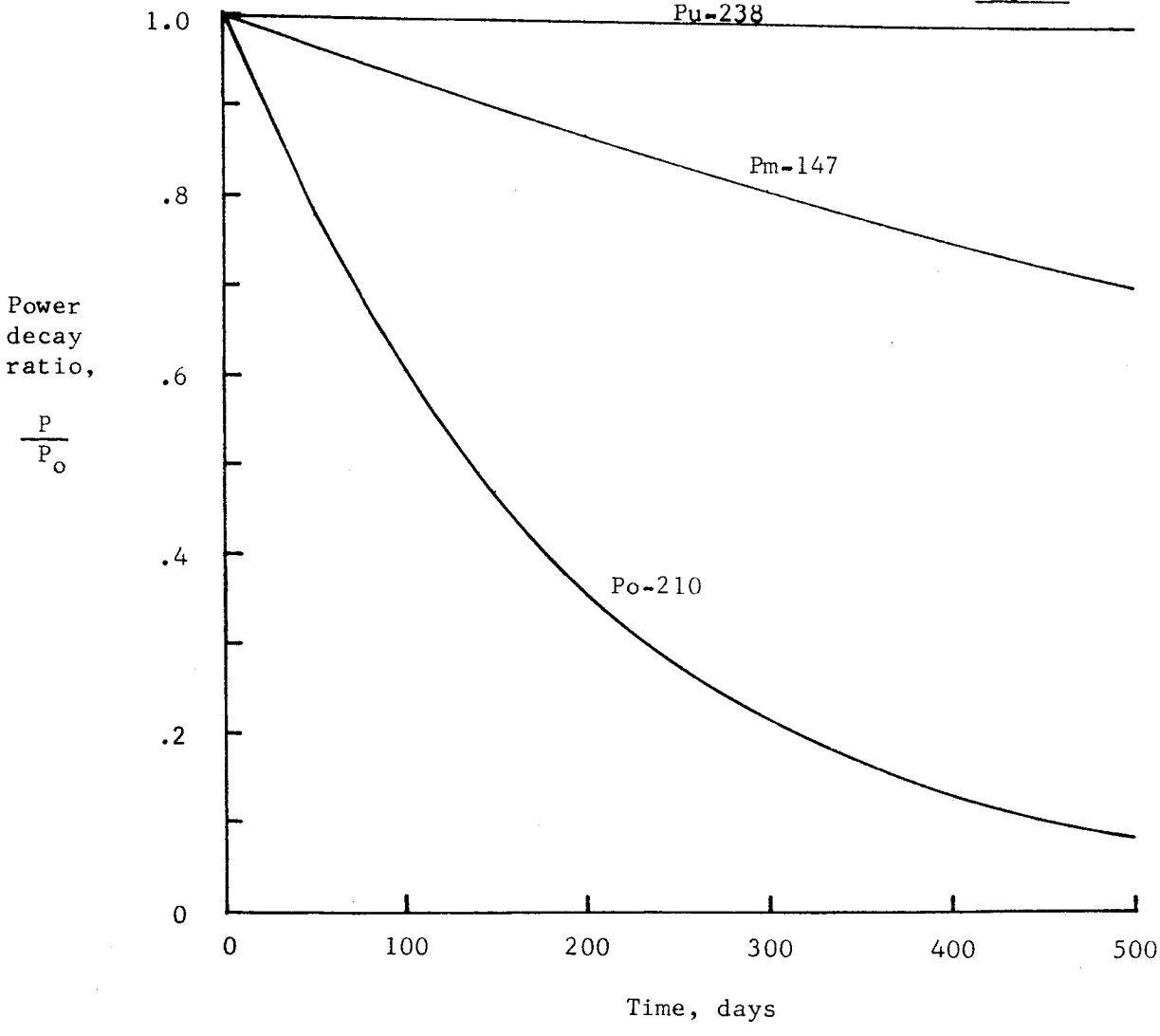

If the ionizer heating power is primarily due to radiation heat transfer, then the significant parameter is $(P/P_o)^{\frac{1}{4}}$. In real ion thrusters, there is considerable ionizer heat loss due to conduction, so the value of $(P/P_o)^{\frac{1}{4}}$ is an optimistic measure of performance. However this parameter is plotted in the following figure to represent the most optimistic performance obtainable from the three radioisotopes in contact ionizer heater applications. Actual decreases in ionizer temperature will be greater than suggested by the parameter $(P/P_o)^{\frac{1}{4}}$.

Fig. 7

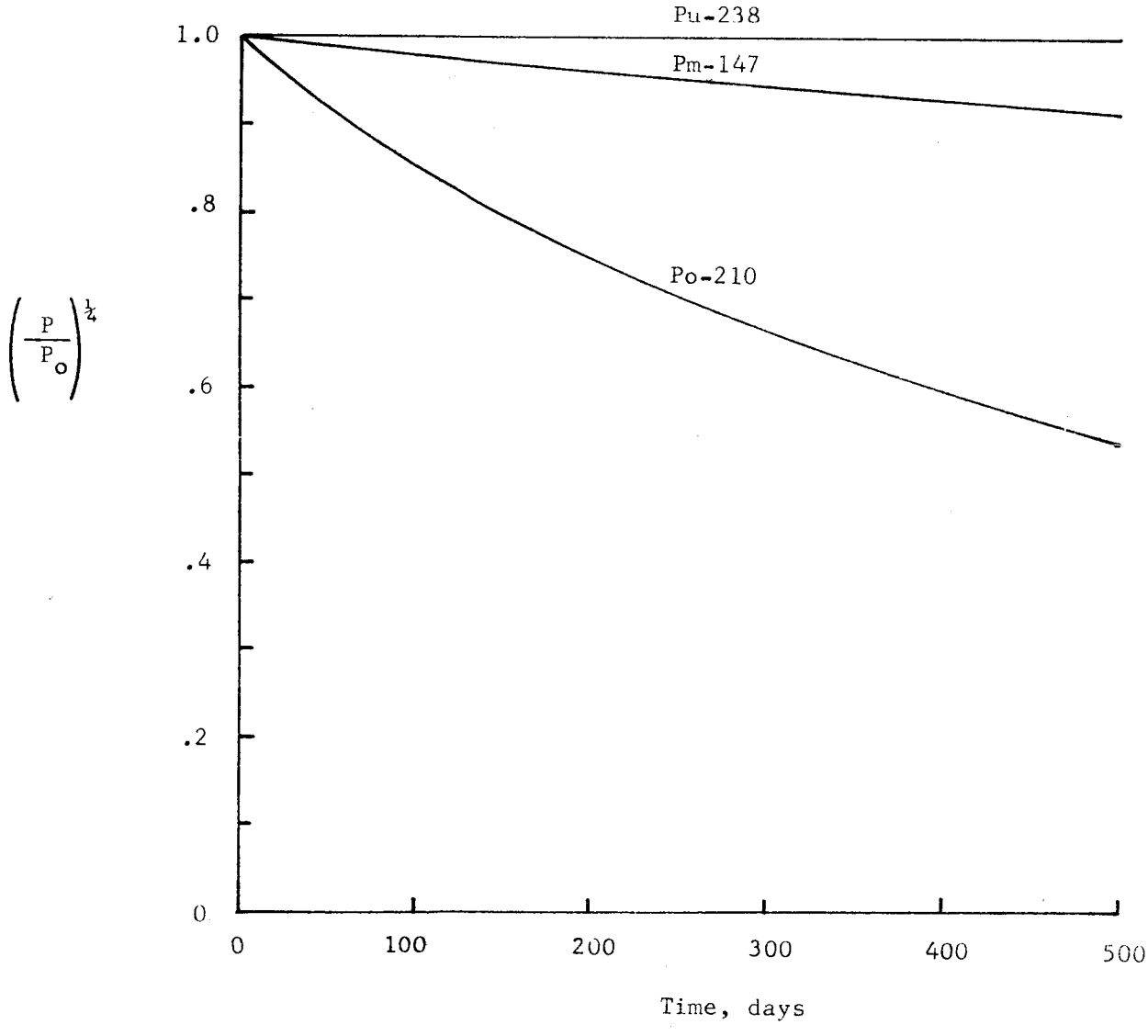

Allowable variation in ionizer temperature will depend on a number of factors and considerations. The most obvious of these is that the ionizer temperature must not be allowed to fall below the critical value for contact ionization. Ionizer temperature may be higher than the critical value, but the neutral atom fraction will be higher also, as illustrated in the following figure which is for a typical porous tungsten ionizer.[8]

Fig. 8

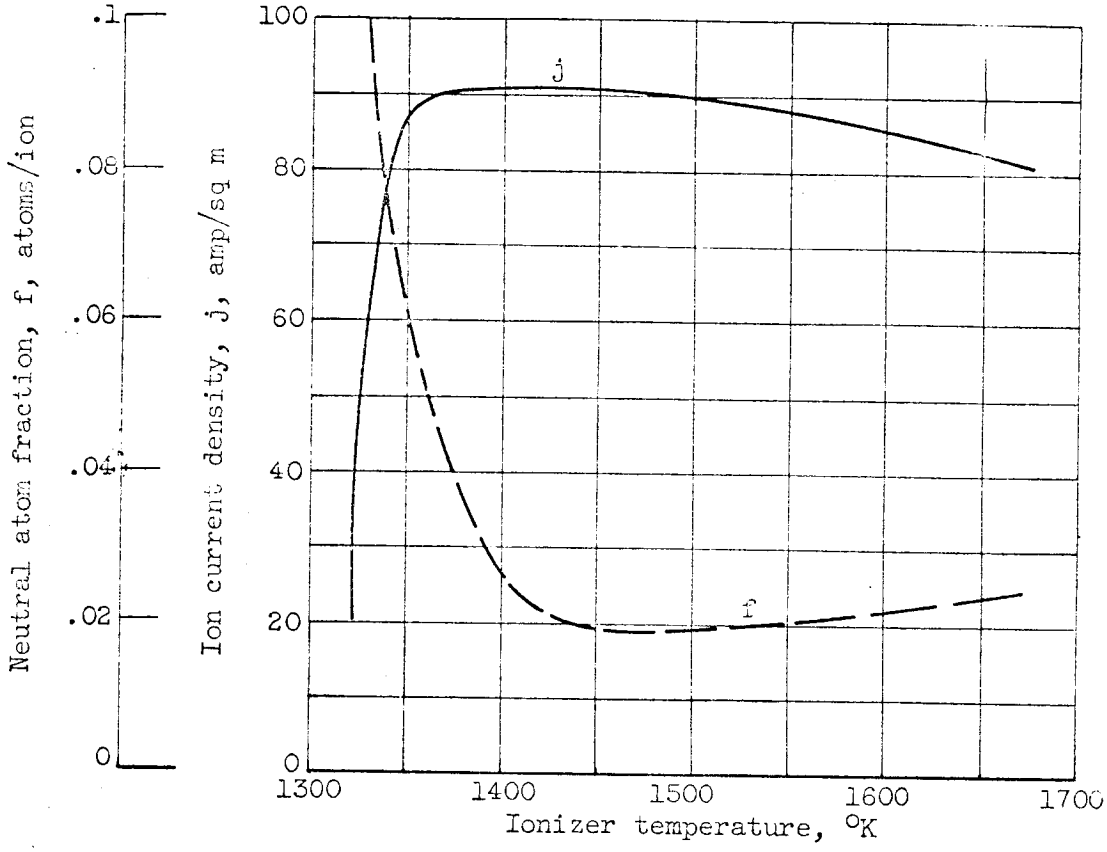

From inspection of this figure it appears that a temperature change of 200°K would be acceptable. This amounts to a temperature change of about 15%. With reference to the preceding figure, it appears that Pu - 238 would certainly provide less than 15% temperature change over reasonable mission times, and that Pm - 147 might be acceptable on this basis if most of the ionizer

heat loss were thermal radiation. However, a Po - 210 system would require some means of maintaining a fairly constant temperature for most missions. For example, a mechanical shutter arrangement is used in radioisotope-thermoelectric powerplants to obtain power-flattening. If Po - 210 were used for ionizer heating, then the weights of the shutters, mechanism, and controls would have to be charged against the thruster, thereby increasing the thruster effective specific weight. For these reasons, Po - 210 is not considered as a possible radioisotope for ionizer heating in the present analysis.

Effective specific weight[1] of contact-ionization thrusters with radioisotope heating of the ionizer can be estimated from the information presented so far. An expression for thruster effective specific weight α^*_{th} can be written as[3]:

$$\alpha^*_{th} = \alpha_{th} + \alpha_r \left(\dot{Q}/P_{j,eff}\right) + \left(\alpha_c + \alpha_{pp}/\eta_c\right)\left(1-\eta_{th}\right)/\eta_{th} + M_{tank}/P_{j,eff} \qquad (6)$$

where the following definitions are used:

α_{th} = physical specific weight of thruster, lb/kwj

α_r = specific weight of radioisotope, lb/kwt

α_c = physical specific weight of power conversion, power conditioning, and controls, lb/kwe

α_{pp} = specific weight of powerplant

η_c = efficiency of power conversion, conditioning, and controls subsystem

η_{th} = thruster efficiency

M_{tank} = weight of propellant tanks

The Hughes multi-strip thruster can be used for purposes of comparison with other existing thrusters. This thruster has a weight for a given ionizer area[4], and assuming that the electric heaters would weigh no more than the

radioisotope container, and that the heat shielding would be the same as for the all-electric design, then the physical specific weight is:

$$\alpha_{th} = (24.3 \times 1000)/(0.0115 \times 170 \times \phi_{net}) = 12{,}400/\phi_{net} \qquad (7)$$

Specific weights of radioisotopes are listed in Table 1. Pu - 238 has a lower specific weight than Pm - 147, so Pu - 238 is used for the present analysis in order to be the most favorable towards the radioisotope-ionizer-heating concept. The ratio $\dot{Q}/P_{j,eff}$ is given by equation (5). Some other system parameters must be assumed: α_c = 10 lb/kwe, η_c = .92, and α_{pp} = 20 lb/kwe (these are the same as used in a previous comparison[3] of existing thrusters).

With radioisotope heating of the ionizer, the only remaining thruster losses are the vaporizer heating, the neutralizer power, and the accelerator drain currents. These losses will vary with thruster module size. For example, the NASA-Lewis mercury-discharge thruster has such losses amounting to about 5% for a 15-cm anode size and about 1% for a 50-cm anode size at design operating conditions of 5000 and 9000 seconds specific impulse respectively. These losses are equivalent to about 190 ev/ion for the 15-cm thruster and 100 ev/ion for the 50-cm thruster. Since the 50-cm mercury-discharge thruster represents the best performance to date, the neutralizer and vaporizer powers of 100 ev/ion will be assumed here. This assumption results in an expression for thruster efficiency as follows:

$$\eta_{th} = \frac{1}{1 + (100/\phi_{net})} \qquad (8)$$

Propellant utilization efficiency has been assumed to be 100%, but would be somewhat less if a plasma-bridge neutralizer were used.

Tankage has been discussed in a previous analysis[3], where a 24% tankage for cesium was calculated by comparison with a flight-qualified mercury tank

design[9]. Future advances in tank design such as frozen cesium may decrease this tankage fraction, but until such advances are shown to be feasible, the 24% tankage represents the best state-of-the-art. In the previous analysis[3], a tankage penalty of $M_{tank}/P_{j,eff}$ = 8 lb kwj was found for cesium-propellant thrusters, and this same value is used here.

Effective specific weight of a contact-ionization thruster with radio-isotope-ionizer heating can be estimated from the discussion so far. An estimate such as this is shown in the following figure.

Fig. 9

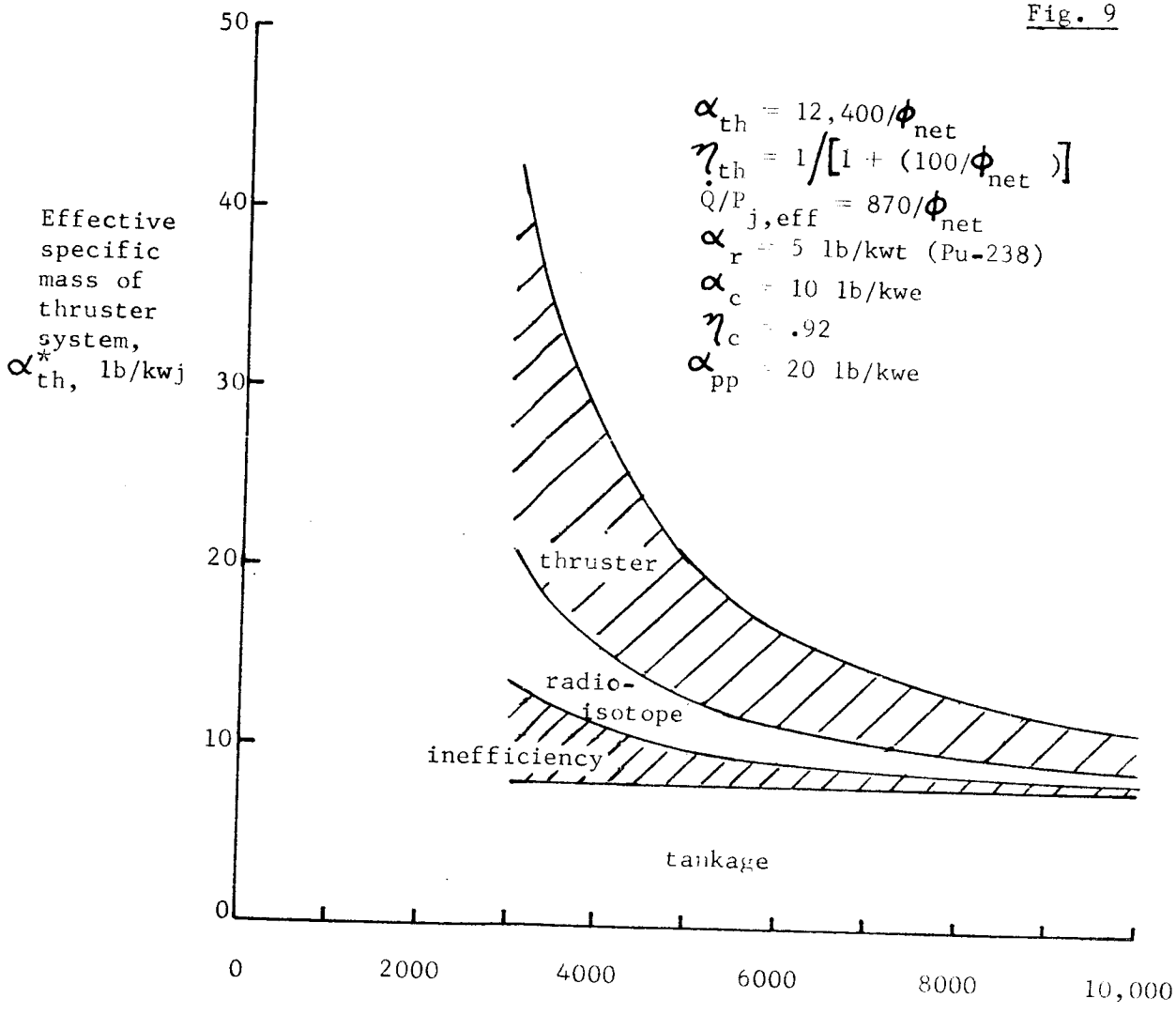

If lighter weight tankage can be devised, then the total values of α^*_{th} could be reduced accordingly. It must be noted here that the additional penalty associated with non-ideal thrust program is not included in these calculations. This penalty can amount to 5 or 10 lb/kwj for many missions[1].

The preceding figure was composed without regard to radioisotope availability. As discussed previously, 1/3 of the 1980 annual production of Pu-238 might be assigned to electric propulsion, which would amount to 20 kwt. This limitation in availability would result in the restrictions in the operating range of the radioisotope-heated contact-ioniztion thruster as indicated in the following figure. This figure was constructed from the information shown in Figures 5 and 9.

Fig. 10

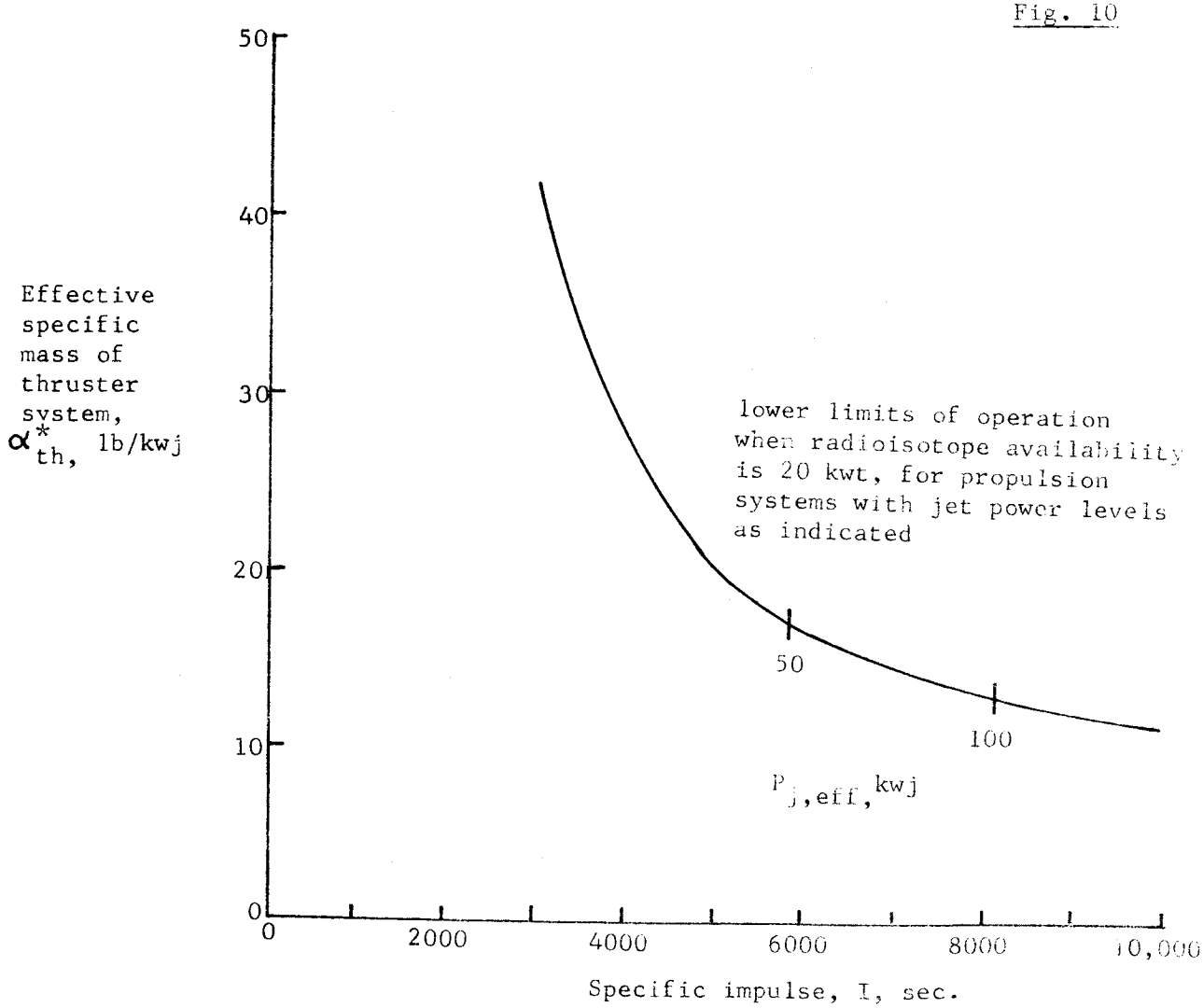

From inspection of this figure it is clear that radioisotope heating of contact thruster ionizers would be limited to electric propulsion systems having power levels in the lowest portion of the range of interest for Saturn-V-class boosted electric spacecraft.

If radioisotope availability were increased by a factor of five to 100 kwt, then the restrictions in operating range would be as shown in the next figure.

Fig. 11

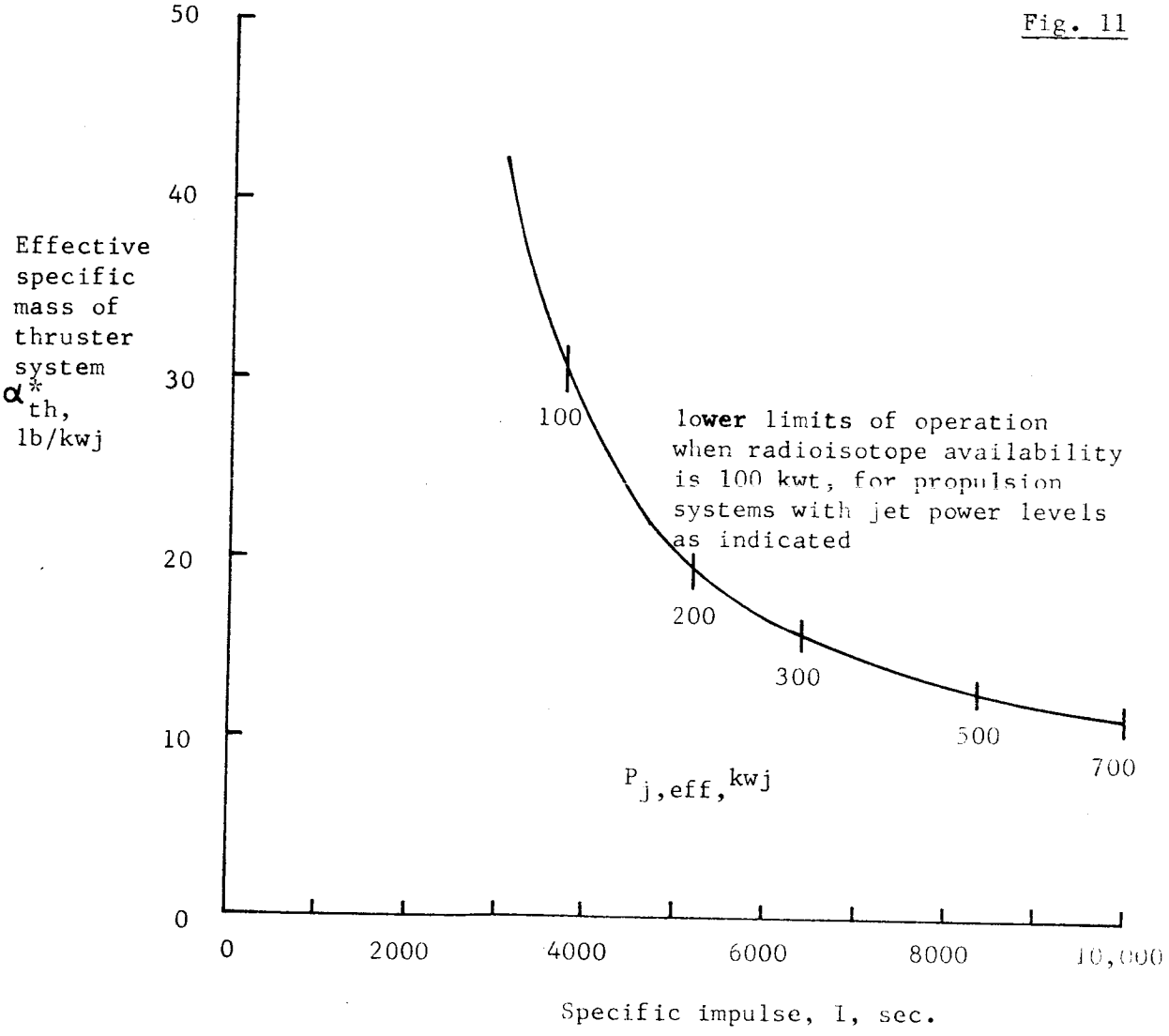

Availability of radioisotopes may be different from these discussed here. In this event, the lower limits of operation would change, and could be incorporated quite simply onto figures such as the preceding. The general format of calculations could be the same as used herein.

The final portion of assessment of the radioisotope-heated contact-ionization thruster is that of comparison with existing and hypothetical future thrusters. This comparison can be done with the aid of a previous[3] analysis, and is shown in the following figure.

Fig. 12

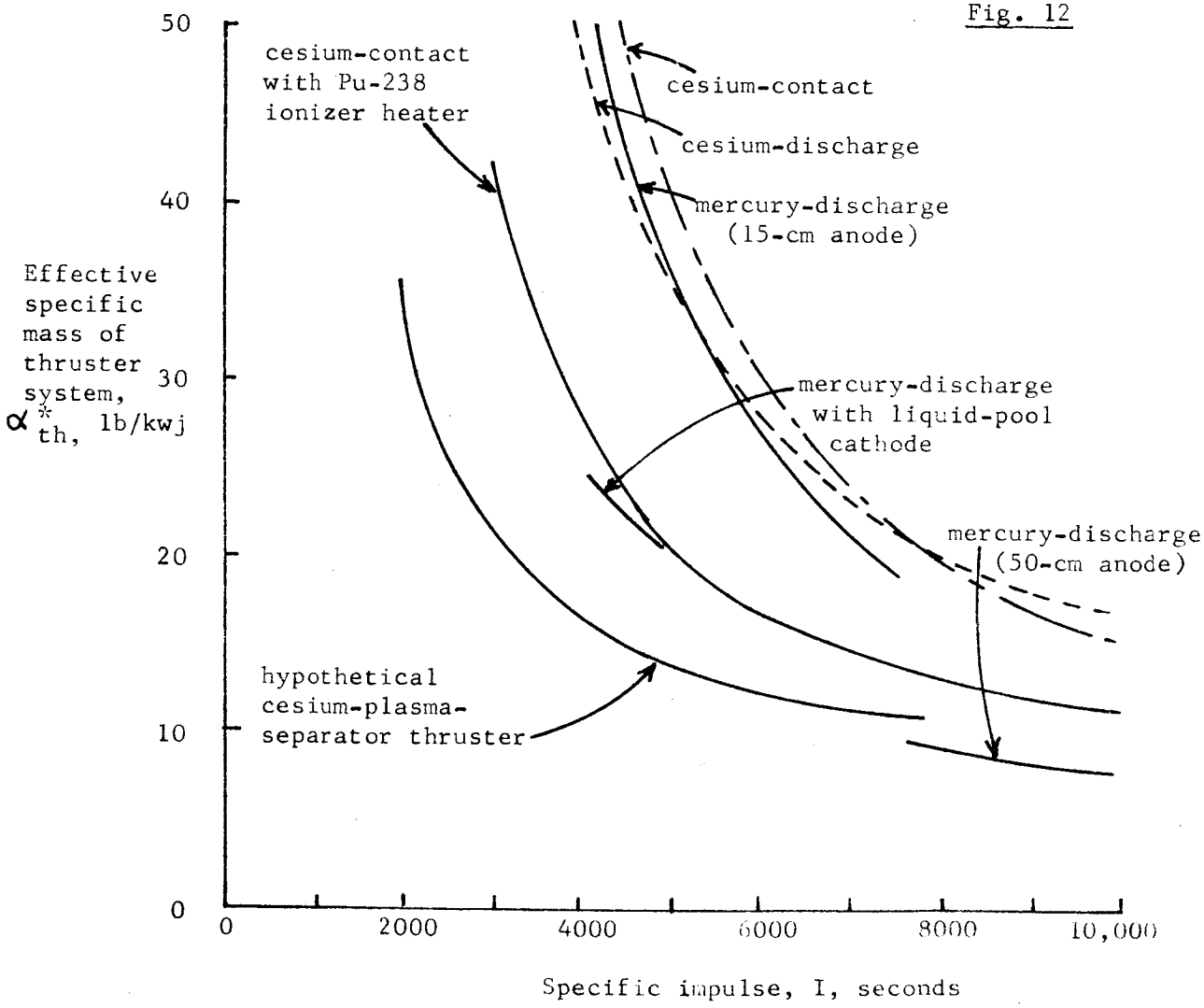

On the basis of this comparison, the cesium-contact thruster with a Pu-238 ionizer heater appears to offer performance gains over existing thrusters. It should be noted here that a neutralizer and vaporizer power loss of 100 ev/ion has been charged against the radioisotope-heated contact thruster. If this loss could be reduced, then the performance would be somewhat better. A rough estimate of possible savings in inefficiency loss can be made by inspection of Figure 9.

The disquieting feature of the radioisotope-heated contact thruster is the limitation of operating range due to radioisotope availability. If boosters smaller than the Saturn-V class could be used for electric spacecraft missions, these limitations would be eased somewhat. For example, solar-electric spacecraft boosted with the Saturn 1B/Centaur might be a possible application. However, such applications would be short-range, and the question of whether the costs of development of a radioisotope-heated contact thruster system would be worthwhile is cogent to the future of the overall electric propulsion program. If this application is considered seriously, then a more exact and comprehensive systems study could be done along the lines of the analysis described here.

This analysis has been confined to consideration of primary electric propulsion. Application of radioisotope heaters to contact-ionization thrusters for satellite attitude and position control is certainly feasible with regard to radioisotope availability. The potential advantage of elimination of electric heaters is attractive, and would do much to reduce the complexity of currently proposed electrostatic thrusters for satellite propulsion.

References

1. Mickelsen, W.R.: Performance Parameters for Electric Propulsion Systems. Journal of Spacecraft and Rockets. February, 1966.

2. Melbourne, W.G.: Interplanetary Trajectories and Payload Capabilities of Advanced Electric Propulsion Vehicles. Jet Propulsion Laboratory Technical Report No. 32 - 68. March, 1961.

3. Mickelsen, W.R.: Future Trends in Electric Propulsion. AIAA Paper No. 66-595. June, 1966.

4. Zimmerman, R.L., Garvin, H.L., McKee, W.E., and Kami, S.: Development of Multistrip Cesium Contact Thrusters. AIAA Paper No. 66-235. March, 1966.

5. Division of Isotopes Development: Present and Potential Annual Availability of Isotopic Power Fuels. U.S. Atomic Energy Commission. April, 1962.

6. Rohrmann, C.A., and Sayre, E.D.: Radioisotopic Space Power-Prospects and Limitations. AIAA Paper No. 64-453. September, 1964.

7. Streb, A.J.: Radioisotope Power Systems for Manned Space Stations. AIAA Paper No. 64-711. September, 1964.

8. Mickelsen, W.R., and Kaufman, H.R.: Status of Electrostatic Thrusters for Space Propulsion. NASA TN D-2172. May, 1964.

9. Molitor, J.H., Berman, D., Seliger, R.L., and Olson, R.N.: Design of a Solar-Electric Propulsion System for Interplanetary Spacecraft. AIAA Paper No. 66-214. March, 1966.

PROPELLANT FROM SPENT TANKAGE

by W.R. Mickelsen

Spent tankage has been suggested as a possible source of propellant for electric spacecraft[1]. Chemical rocket propellant tanks are expected to be made of aluminum because of the superior fracture resistance of aluminum at cryogenic temperatures[2]. Aluminum melts at 932°K, which is a reasonably moderate temperature for conversion of spent tankage to the vapor state. Aluminum vapor could then be fed into electric thrusters as propellant.

Before investigating the feasibility of aluminum vapor as propellant in electric thrusters, it is necessary to evaluate the improvement in mission performance that would result from the utilization of spent booster tankage. Fortunately a precise evaluation of performance gains can be made in a simple, closed-form analysis which is described in this section.

Payload mass fraction M_{pay}/M_o for electric spacecraft is given by the expression derived by Melbourne[3]:

$$L \equiv \frac{M_{pay}}{M_o} = \frac{1}{1 + \frac{M_o}{2P_{j,eff}} J} - \frac{M_{ps}}{M_o} \qquad (1)$$

In this expression the following definitions are used:

M_{pay} = mass of payload delivered at terminus of electric-propulsion phase

M_o = total mass of electric spacecraft at beginning of electric propulsion phase, including spent-tankage used as propellant

$P_{j,eff}$ = effective jet power, ie, $P_{j,eff} = F^2/(2\dot{m}_{tot})$, where F is thrust and $\dot{m}_{tot}$ is total rate of propellant consumption

$J = \int_o^\tau (F/M)\, dt$, where τ is the propulsion duration, and M is instantaneous mass of the electric spacecraft

M_{ps} = mass of electric propulsion system

If spent tankage from upper stages of chemical boosters were used for electric-thruster propellant, then the parameter for evaluating mission performance is the payload mass fraction based on electric spacecraft mass not including the spent tankage mass M_{st}. That is, the chemical booster would launch an electric spacecraft of mass $M_o - M_{st}$, and the spent booster tankage would be added to make a total spacecraft starting mass of M_o. This payload fraction L_{st} is defined by:

$$L_{st} \equiv \frac{M_{pay}}{M_o - M_{st}} \tag{2}$$

where M_{st} is the mass of spent tankage which is salvaged for electric-propulsion propellant. By combining equations (1) and (2), the following expression for payload fraction can be written:

$$L_{st} = \frac{1}{\frac{M_o - M_{st}}{M_o} + \frac{M_o - M_{st}}{M_{ps}} \left[\frac{\alpha_{ps}}{2} J\right]} - \frac{M_{ps}}{M_o - M_{st}} \tag{3}$$

where α_{ps} is the propulsion-system specific mass.

Spent tankage mass fraction F can be defined as:

$$F \equiv \frac{M_{st}}{M_o} \tag{4}$$

Propulsion-system mass fraction S can be defined as:

$$S \equiv \frac{M_{ps}}{M_o - M_{st}} = \frac{M_{ps}}{M_o} \frac{1}{1 - F} \tag{5}$$

These mass fractions can be used to simplify equation (3) as follows:

$$L_{st} = \frac{1}{1 - F + \frac{1}{S} \left[\frac{\alpha_{ps}}{2} J\right]} - S \tag{6}$$

This equation can be further simplified by using the Melbourne[3] parameter β:

$$\beta^2 \equiv \frac{\alpha_{ps}}{2} J \tag{7}$$

which results in:

$$L_{st} = \frac{1}{1 - F + \frac{\beta^2}{S}} - S \tag{8}$$

Mass fraction F and the parameter β are fixed by the mission and by the propulsion system specific mass. Propulsion-system mass fraction S can be varied to obtain maximum payload by setting $dL_{st}/dS = 0$ as follows:

$$\frac{dL_{st}}{dS} = \frac{\beta^2/S^2}{(1 - F + \beta^2/S)^2} - 1 = 0 \tag{9}$$

Solving for optimum S:

$$S_{opt} = \frac{\beta(1 - \beta)}{1 - F} \tag{10}$$

and using this expression for S_{opt} in equation (8):

$$L_{st} = \frac{1}{1 - F}(1 - \beta)^2 \tag{11}$$

Maximum payload mass fraction L when spent tankage is not used is derived by Melbourne[3] with the relult:

$$L_{max} = (1 - \beta)^2 \tag{12}$$

The gain in mission performance can be expressed as the ratio of payload mass fractions:

$$\frac{L_{st}}{L} = \frac{1}{1 - F} \tag{13}$$

Melbourne[3] has also shown that when payload is maximized, then the propellant mass fraction M_{pr}/M_o is:

$$\frac{M_{pr}}{M_o} = \beta \tag{14}$$

Now, it is clear that for maximum payload gain, F should be as near unity as possible in equation (13). However F cannot exceed the propellant mass fraction given by equation (14). Therefore, the maximum payload gain is expressed by:

$$\left(\frac{L_{st}}{L}\right)_{max} = \frac{1}{1-\beta} \tag{15}$$

Payload mass-fraction gains calculated from equation (13) are shown in Figure 1.

Fig 1.

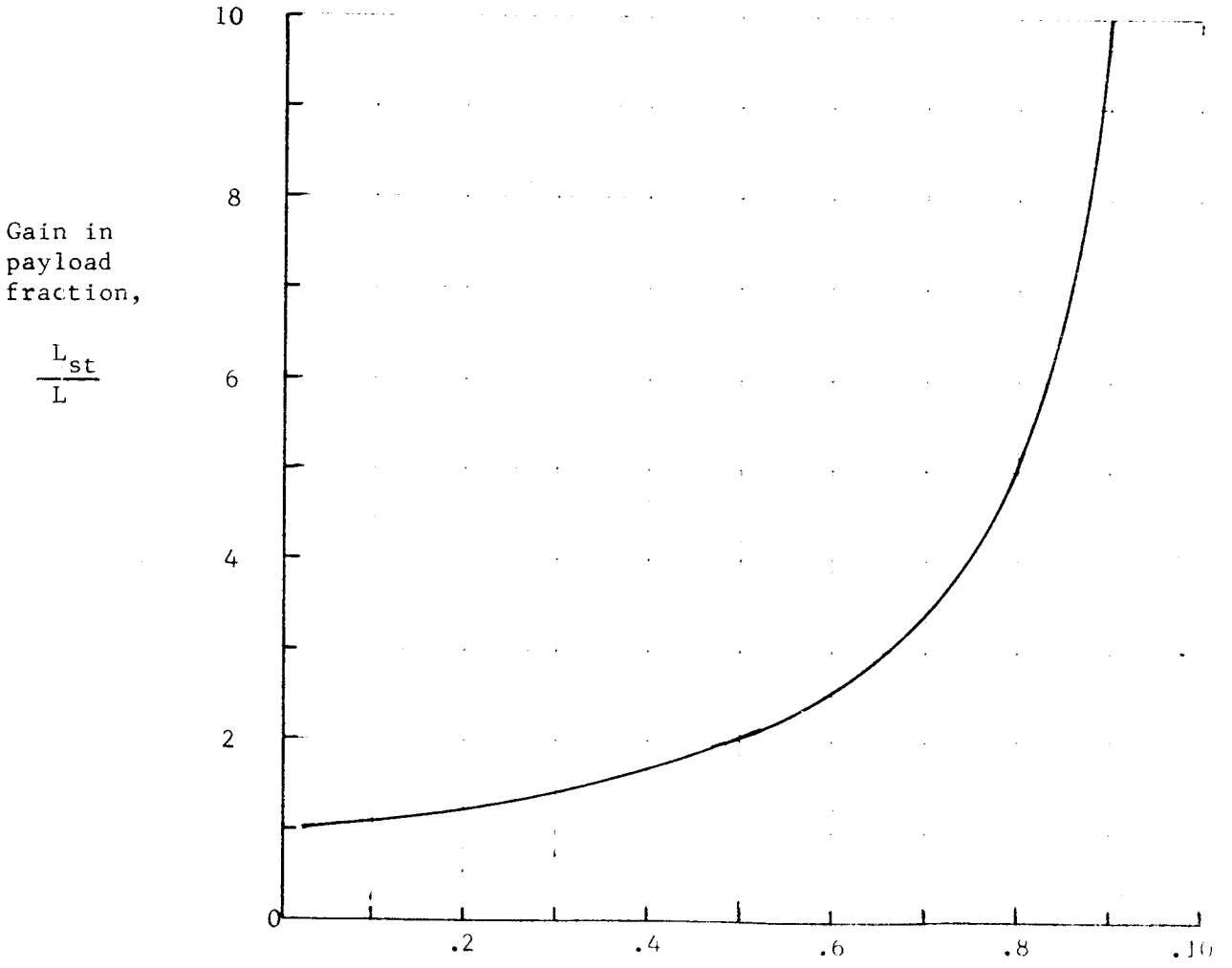

From inspection of Figure 1 it is evident that the greatest gains in payload fraction will occur at the highest values of F, which correspond to the highest values of β. In essence, the observation can be made that payload gains will be the greatest for the more difficult missions (ie, those with the highest values of β).

Dependence on mission difficulty can be illustrated further by noting that equation (11) can be rewritten with the aid of equation (14) for F_{max}:

$$L_{st\ max} = 1 - \beta \tag{16}$$

This expression is plotted in Figure 2. Together with equation (12) for L.

Fig. 2

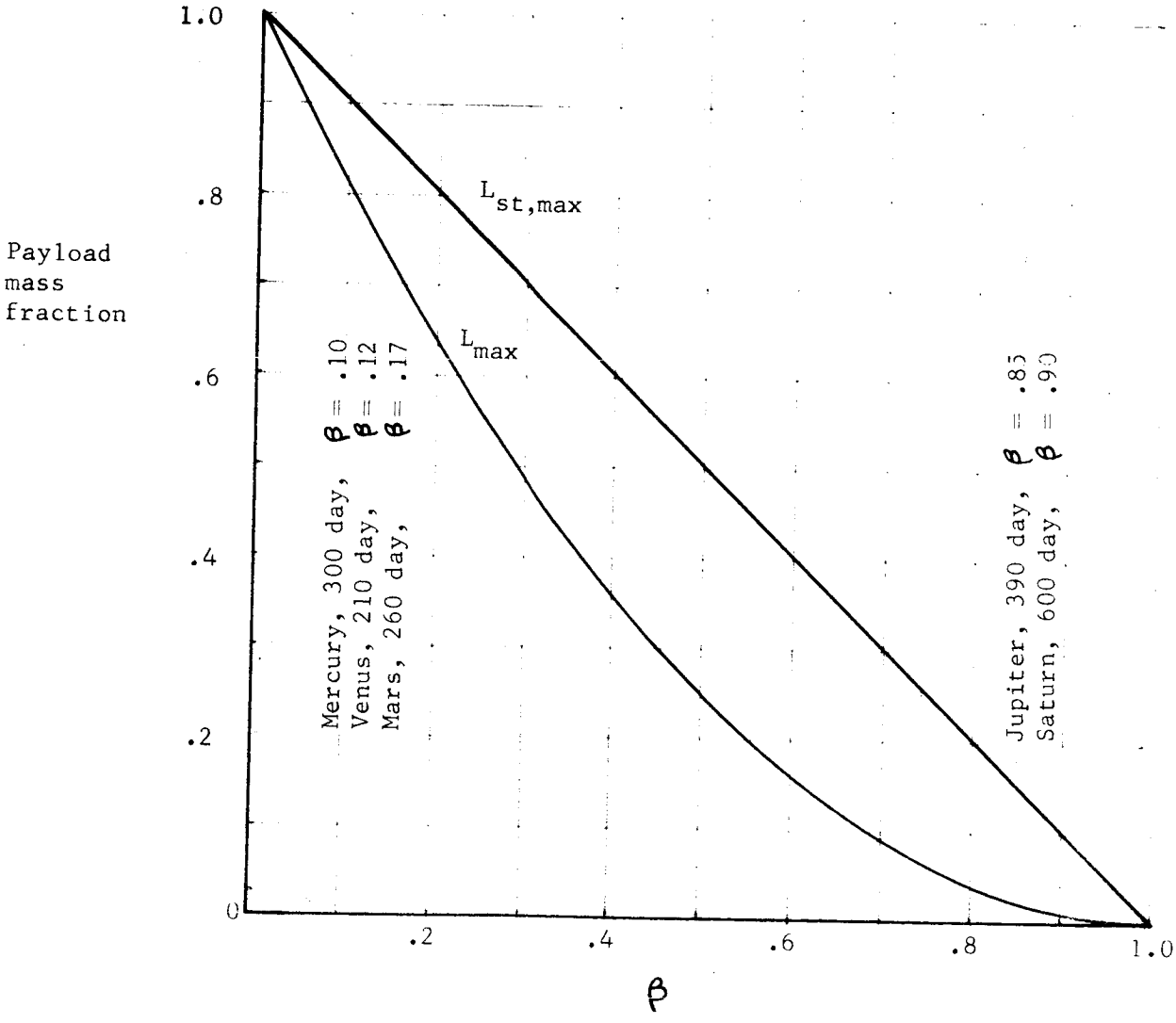

Included in Figure 2 are the approximate locations of β for various heliocentric transfer missions for planetary orbiters with $\alpha_{ps} = 15$ kg/kwj. From this figure it is also evident that the greatest payload gains by use of spent tankage will be for the more ambitious missions.

REFERENCES

1. Mickelsen, W.R.: "Future Trends in Electric Propulsion". AIAA Paper No. 66-595. June, 1966.

2. Johnsen, I.A., and Smith, G.: private communication. NASA Lewis Research Center. April 22, 1966.

3. Melbourne, W.G.: "Interplanetary Trajectories and Payload Capabilities of Advanced Propulsion Vehicles". JPL Technical Report No. 32-68. March, 1961.

THERMAL POWER AUGMENTATION IN ELECTRIC PROPULSION SYSTEMS

by William R. Mickelsen

Jet power in conventional electric propulsion systems would be produced entirely from the electric power output from the electric powerplant. This electric power might be produced in a Rankine-cycle powerplant having a prime thermal-power source such as a nuclear reactor. The thermodynamic cycle is usually not very efficient, and the electric powerplant has a significant mass which detracts from payload capacity of the electric spacecraft. Augmentation of the jet power with thermal power directly from the prime thermal-power source is a possible means for improving electric spacecraft performance.

Thermal power augmentation in electric propulsion systems can be represented schematically as in Figure 4.1. The basic mode of operation is that the propellant passes through a prime thermal power source thereby acquiring a thermal power represented by the product of total enthalpy and mass flow rate. The heated propellant then passes through a nozzle in which the total enthalpy is converted to kinetic energy of the high-speed propellant flow. Propellant enters the electric thruster with a significant thermal power. Electric power is used in the electric thruster to add to the power contained in propellant motion. Final jet power is simply the sum of the thermal power entering the thruster and the electric power added to the propellant stream in the electric acceleration process. Electric power is generated by the electric powerplant which derives its power from the prime thermal power source. Here the electric powerplant is assumed to contain all power conditioning and controls required by the electric thruster.

Two prime thermal power sources are shown in Figure 4.1, but these two could be combined into one source such as one nuclear reactor. Another configuration

might be a nuclear reactor for the electric powerplant, and a chemical reaction for the thermal heating of the propellant. For example, an exothermic chemical reaction might be a part of colloid-particle formation during the flow through the nozzle. Chemical power released in such colloid-particle electrostatic propulsion systems could be utilized for thermal power augmentation of jet power as illustrated in Figure 4.1

Performance of the ATEP thermal-power-augmentation electric-propulsion system* can be evaluated by comparison with conventional electric propulsion systems. Such an analysis is done here.

Total mass M_{ps} of the ATEP system is:

$$M_{ps} = M_{pp} + M_r + M_n + M_{th} + M_{tank} \tag{4.1}$$

where M_{pp} is electric powerplant mass, M_r is the mass of the prime thermal power source for propellant heating, M_n is mass of the propellant-flow nozzle subsystem, M_{th} is electric thruster mass, and M_{tank} is propellant-tank mass. Equation (4.1) can be rewritten:

$$M_{ps} = \wp_{pp} (M_{pp}/\wp_{pp}) + \wp_r (M_r/\wp_r) + P_n (M_n/P_n) + \eta_{th} \wp_{pp} \left[M_{th}/(\eta_{th}\wp_{pp})\right] + M_{tank} \tag{4.2}$$

where η_{th} is electric thruster efficiency, and where the powers are as shown in Figure 4.1. A physical specific mass can be defined for each of the subsystems:

$$\alpha_{pp} = M_{pp}/\wp_{pp} \tag{4.3}$$

$$\alpha_r = M_r/\wp_r \tag{4.4}$$

$$\alpha_n = M_n/P_n \tag{4.5}$$

$$\alpha_{th} = M_{th}/(\eta_{th}\wp_{pp}) \tag{4.6}$$

*ATEP system: augmented-thermally electric propulsion system

These specific masses can be substituted into equation (4.2):

$$M_{ps} = \alpha_{pp} \wp_{pp} + \alpha_r \wp_r + \alpha_n P_n + \alpha_{th} \eta_{th} \wp_{pp} + M_{tank} \tag{4.7}$$

Specific mass of the entire propulsion system can be defined:

$$\alpha_{ps} = M_{ps}/P_j \tag{4.8}$$

Equation (4.7) can be divided by P_j to obtain:

$$\alpha_{ps} = \alpha_{pp}(\wp_{pp}/P_j) + \alpha_r (\wp_r/P_j) + \alpha_n (P_n/P_j) + \alpha_{th}\eta_{th}(\wp_{pp}/P_j) + M_{tank}/P_j \tag{4.9}$$

The last term can be related to α_{ps} as follows:

$$M_{tank}/P_j = \alpha_{ps} M_{tank}/M_{ps} \tag{4.10}$$

Tank mass can be related to propellant mass M_{pr} through a tankage factor k:

$$M_{tank} = k M_{pr} \tag{4.11}$$

Combining equations (4.10) and (4.11):

$$M_{tank}/P_j = \alpha_{ps} k M_{pr}/M_{ps} \tag{4.12}$$

This equation can be expressed in terms of vehicle mass fractions:

$$M_{tank}/P_j = \alpha_{ps} k (M_{pr}/M_o)/(M_{ps}/M_o) \tag{4.13}$$

where M_o is the total initial mass of the vehicle.

Further derivation is required before equation (4.13) can be stated in terms of mission parameters.

By means of a fundamental analysis, the payload fraction M_{pay}/M_o can be derived (e.g. reference 4.1, pp. 45-48):

$$\frac{M_{pay}}{M_o} = \frac{1}{1 + \frac{1}{2}\frac{M_o}{P_j}\int_o^\tau (F/M)^2 \, dt} - \frac{M_{ps}}{M_o} \tag{4.14}$$

The first term on the right side of equation (4.14) is the final mass fraction, so that the propellant mass fraction is:

$$\frac{M_{pr}}{M_o} = 1 - \frac{1}{1 + \frac{1}{2}\frac{M_o}{P_j}\int_o^\tau (F/M)^2 \, dt} \tag{15}$$

From the previous definition of propulsion system specific mass, it is evident that the sub-system masses can be separated into power components and propellant components, and the propulsion system mass fraction can be written:

$$M_{ps}/M_o = M_e/M_o + M_{tank}/M_o \tag{16}$$

Using the tankage factor k:

$$M_{ps}/M_o = M_e/M_o + k(M_{pr}/M_o) \tag{17}$$

From equations (4.14), (4.15), and (4.17):

$$\frac{M_{pay}}{M_o} = \frac{1 + k}{1 + \frac{1}{2}\frac{M_o}{P_j}\int_o^\tau (F/M)^2 \, dt} - \frac{M_e}{M_o} - k \tag{18}$$

This expression can also be written as:

$$\frac{M_{pay}}{M_o} = \frac{1 + k}{1 + \frac{1}{2}\frac{M_o}{M_e}\frac{M_e}{P_j}\int_o^\tau (F/M)^2 \, dt} - \frac{M_e}{M_o} - k \tag{19}$$

A new specific mass α_e can be defined:

$$\alpha_e \equiv M_e/P_j \tag{20}$$

and this specific mass will be assumed constant in the derivation that follows. With this definition of specific mass, a parameter τ can be defined:

$$\tau^2 \equiv \frac{1}{2}\alpha_e \int_o^\tau (F/M)^2 \, dt \tag{21}$$

and with this parameter, equation (4.19) can be simplified:

$$\frac{M_{pay}}{M_o} = \frac{1 + k}{1 + \sigma^2/(M_e/M_o)} - \frac{M_e}{M_o} - k \qquad (4.22)$$

For maximum payload there is an optimum value of M_e/M_o which can be found by differentiating equation (4.22) with respect to M_e/M_o and setting equal to zero. The resulting optimum value of M_e/M_o is:

$$(M_e/M_o)_{opt} = \sigma \left[(1+k)^{\frac{1}{2}} - \sigma\right] \qquad (4.23)$$

which is similar to Melbourne's results (e.g. reference 2).

By comparing equations (4.22) and (4.15), and by using the optimum ratio of M_e/M_o as given by equation (4.23), the propellant mass fraction for maximum payload is:

$$M_{pr}/M_o = \sigma/(1+k)^{\frac{1}{2}} \qquad (4.24)$$

Equations (4.17), (4.23), and (4.24) can be used to find an expression for M_{ps}/M_o:

$$\frac{M_{ps}}{M_o} = \sigma\left[\frac{1 + 2k}{(1+k)^{\frac{1}{2}}} - \sigma\right] \qquad (4.25)$$

Equations (4.24) and (4.25) can be used in equation (4.13) to obtain:

$$\frac{M_{tank}}{P_j} = \alpha_{ps}\left[\frac{k}{1 + 2k - (1+k)^{\frac{1}{2}}\sigma}\right] \qquad (4.26)$$

which is the expression desired.

An expression for α_{ps} can be found by combining equations (4.9) and (4.26):

$$\alpha_{ps}\left[1 - \frac{k}{1 + 2k - (1+k)^{\frac{1}{2}}\sigma}\right] = \alpha_{pp}\,(\wp_{pp}/P_j) + \alpha_r\,(\wp_r/P_j) + \alpha_n\,(P_n/P_j) + \alpha_{th}\,\eta_{th}\,(\wp_{pp}/P_j) \qquad (4.27)$$

The power ratios in equation (4.27) can be written in terms of the nozzle exit speed v_n and the jet exhaust speed v_j as follows. Electric power input to the

propellant stream in the electric thruster is $P_j - P_n$, so that:

$$\mathcal{P}_{pp} = (P_j - P_n)/\eta_{th} \tag{4.28}$$

From this, the ratio $\mathcal{P}_{pp}/P_j$ is:

$$\mathcal{P}_{pp}/P_j = (1 - P_n/P_j)/\eta_{th} \tag{4.29}$$

Exhaust powers from the nozzle and from the electric thruster can be written:

$$P_n = \tfrac{1}{2}\,\dot{m}v_n^2 \tag{4.30}$$

$$P_j = \tfrac{1}{2}\,\dot{m}v_j^2 \tag{4.31}$$

From the preceding relations:

$$\mathcal{P}_{pp}/P_j = (1 - v_n^2/v_j^2)/\eta_{th} \tag{4.32}$$

Stream power at the nozzle exit is:

$$P_n = \eta_n \mathcal{P}_r \tag{4.33}$$

where η_n is the nozzle flow efficiency which must include real-gas effects. From previous relations:

$$\mathcal{P}_r/P_j = (v_n^2/v_j^2)/\eta_n \tag{4.34}$$

These equations for power ratio can be incorporated into equation (4.27) :

$$\alpha_{ps}\left[1 - \frac{k}{1 + 2k - (1+k)^{\frac{1}{2}}\sigma}\right] = (\alpha_{th} + \alpha_{pp}/\eta_{th})\,(1 - v_n^2/v_j^2) + (\alpha_n + \alpha_r/\eta_n)(v_n^2/v_j^2) \tag{4.35}$$

A similar expression can be derived for the specific mass α'_{ps} of conventional electric propulsion systems:

$$\alpha'_{ps}\left[1 - \frac{k}{1 + 2k - (1+k)^{\frac{1}{2}}\sigma'}\right] = \alpha_{th} + \frac{\alpha_{pp}}{\eta_{th}} \tag{4.36}$$

where τ' is:

$$\tau'^2 = \tfrac{1}{2}\alpha'_e \int_0^\tau (F/M)^2 \, dt \qquad (4.30)$$

Equation (4.35) may be divided by equation (4.36) to obtain:

$$\frac{\alpha_{ps}}{\alpha'_{ps}} = \left[1 - \frac{v_n^2}{v_j^2}\left(1 - \frac{\alpha_n + \alpha_r/\eta_n}{\alpha_{th} + \alpha_{pp}/\eta_{th}}\right)\right]\left[\frac{1 - \dfrac{k}{1 + 2k - (1+k)^{\frac{1}{2}}\tau'}}{1 - \dfrac{k}{1 + 2k - (1+k)^{\frac{1}{2}}\tau}}\right] \qquad (4.38)$$

This expression can be rewritten:

$$\frac{\alpha_{ps}}{\alpha'_{ps}} = \left[1 - \frac{v_n^2}{v_j^2}\left(1 - \frac{(\alpha_n/\alpha_{pp}) + \alpha_r/(\alpha_{pp}\eta_n)}{(\alpha_{th}/\alpha_{pp}) + 1/\eta_{th}}\right)\right]\left[\frac{1 - \dfrac{k}{1 + 2k - (1+k)^{\frac{1}{2}}\tau'}}{1 - \dfrac{k}{1 + 2k - (1+k)^{\frac{1}{2}}\tau}}\right] \qquad (4.39)$$

There is a relationship between τ and τ' which can be formulated by inspection of equations (4.21), (4.35), (4.36), and (4.37). First, noting that from equations (4.21) and (4.37):

$$\frac{\tau}{\tau'} = \left(\frac{\alpha_e}{\alpha'_e}\right)^{\frac{1}{2}} \qquad (4.40)$$

Further, it can be seen from equations (4.35) and (4.36) that:

$$\frac{\alpha_e}{\alpha'_e} = 1 - \frac{v_n^2}{v_j^2}\left(1 - \frac{(\alpha_n/\alpha_{pp}) + \alpha_r/(\alpha_{pp}\eta_n)}{(\alpha_{th}/\alpha_{pp}) + 1/\eta_{th}}\right) \qquad (4.41)$$

which is merely the first factor in equation (4.39). Therefore, equation (4.39) can be solved explicitly for α_{ps}/α'_{ps} if values are assigned to the various parameters.

Typical values for the specific mass ratios might be:

$$\alpha_n/\alpha_{pp} = 0.01$$

$$\alpha_r/\alpha_{pp} = 0.10$$

$$\alpha_{th}/\alpha_{pp} = 0.05$$

Typical values of the efficiencies might be:

$$\eta_n = 0.5$$

$$\eta_{th} = 0.9$$

With these typical values, equation (4.39) reduces to:

$$\frac{\alpha_{ps}}{\alpha'_{ps}} = \left[1 - 0.81 \frac{v_n^2}{v_j^2}\right] \frac{\left[1 - \frac{k}{1 + 2k - (1+k)^{\frac{1}{2}} \gamma'}\right]}{\left[1 - \frac{k}{1 + 2k - (1+k)^{\frac{1}{2}} \gamma}\right]} \qquad (42)$$

The ratio α_{ps}/α'_{ps} can be calculated for a range of values of v_n/v_j by assuming values of k and of γ'.

Both the trajectory and the propulsion system specific mass enter into the magnitude of γ'. Values of γ' for conventional electric propulsion systems are shown in Figure 4.2. Reasonable payload fractions are associated with a range of γ' from 0.3 to 0.9. Values of α_{ps}/α'_{ps} calculated from equation 4.42 are shown in Figure 4.3 for a tankage of k = 0. From this figure, it is clear that substantial reductions in propulsion system specific mass are theoretically possible with the ATEP system. Essentially the same reductions in α_{ps}/α'_{ps} would occur for the case of negligible tankage as illustrated in Figure 4.4.

The effect of propulsion-system mass reduction on payload fraction is also of interest. Payload fraction M_{pay}/M_o can be found by combining equations 4.22 and 4.23 with the result:

$$M_{pay}/M_o = 1 + \gamma^2 - (2+k)\gamma/(1+k)^{\frac{1}{2}} \qquad (43)$$

The parameter γ is related to γ' by equations (4.44) and (4.41). Payload fractions of the ATEP system are shown in Figure 4.5 for a range of v_n/v_j and γ'. It can be seen from this figure that the payload in difficult missions (e.g., $\gamma' = .9$) could be doubled even for values of v_n/v_j as low as 0.37. Also a 50% increase

in payload is possible for values of v_n/v_j as low as 0.28.

This analysis has shown that very significant improvement in performance is possible with the ATEP system. Such performance gains are possible only when the nozzle exhaust velocity v_n is about 0.3 or more of the final jet velocity v_j. For example if the nozzle exhaust velocity v_n corresponds to a specific impulse of 300 seconds, the ATEP system would provide significant performance gains only for missions (or portions of missions) that require a specific impulse of 1000 seconds or less. In considering the implications of this statement, it must be remembered that some missions are fairly insensitive to deviations from optimum specific impulse. For instance, optimum specific impulse might be 1300 seconds, but operation at a specific impulse of 1000 seconds might result in only a small loss in payload. If this were true, then an ATEP system with $v_n/g_c = 300$ sec. would be advantageous.

Systems having solid-core nuclear reactors as prime thermal power sources would require a propellant with a low molecular weight. Nuclear reactors are temperature limited, so a low molecular weight is required if v_n is to be an appreciable fraction of v_j.

If electrothermal thrusters were used in an ATEP system, heat would have to be added to a supersonic stream.

If plasma thrusters were used in an ATEP system, plasma generation would have to be done in a supersonic stream having an appropriate density.

If electrostatic thrusters were used in an ATEP system, means for achieving a reasonably high current density in a space-charge-limited accelerator would have to be found. For example, if a low-molecular-weight propellant were thermally accelerated to v_n, and then formed into heavy molecules or into colloids while still moving at v_n, then adequate current density might be achieved.

Primary motivation for further investigation of the ATEP system concepts

must stem from mission requirements. Substantial portions of future space missions will require specific impulse in the neighborhood of 1000 sec., so further investigation of ATEP system applications is justified.

References

4.1. Mickelsen, W. R., and Kaufman, H. R.: Status of Electrostatic Thrustors for Space Propulsion. NASA TN D-2172. May, 1964.

4.2. Melbourne, W. G.: Interplanetary Trajectories and Payload Capabilities of Advanced Propulsion Vehicles. TR 32-68, Jet Propulsion Laboratory, California Institute of Technology. March 31, 1961.

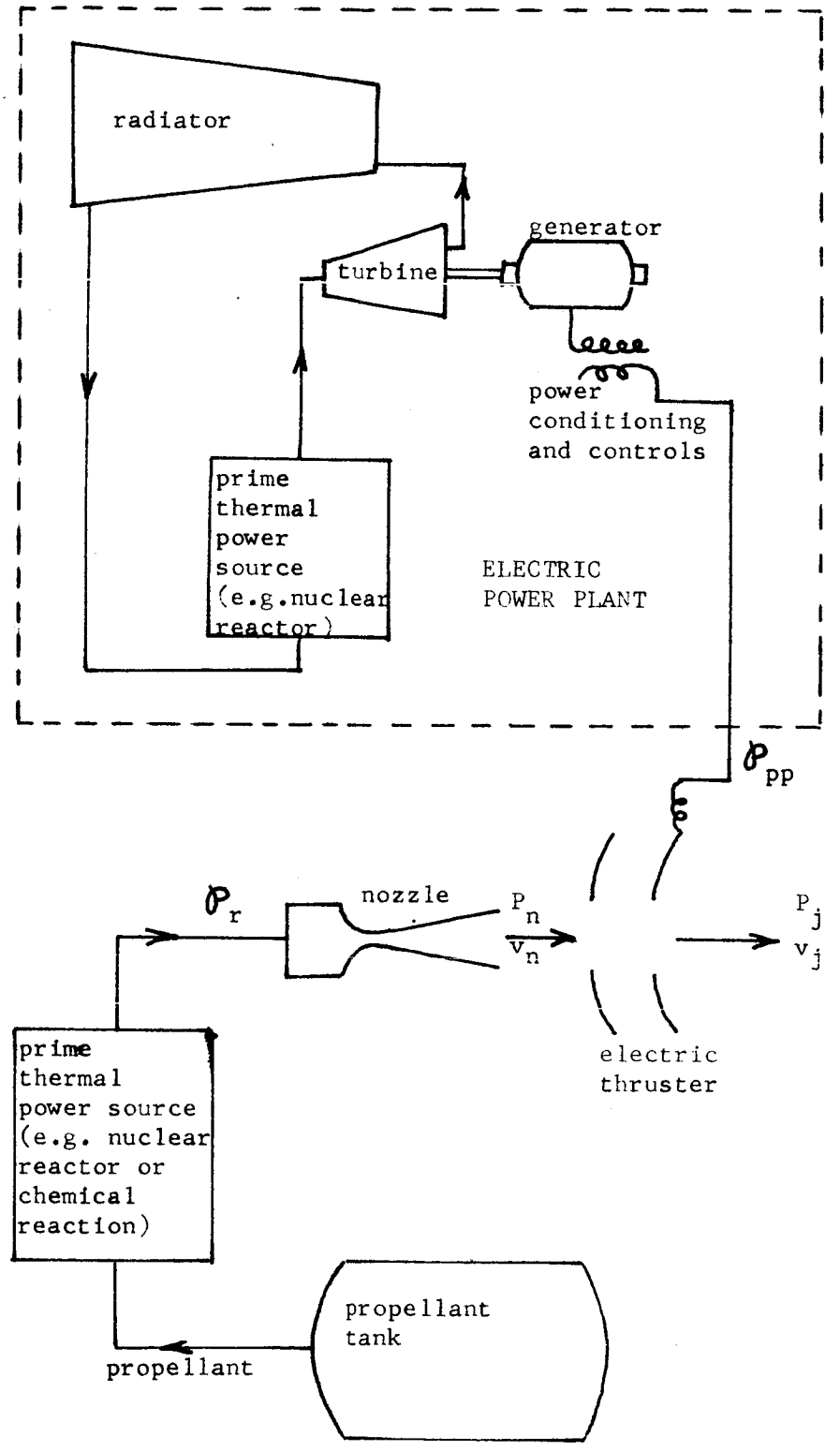

Fig. 4.1 Schematic drawing of ATEP system.

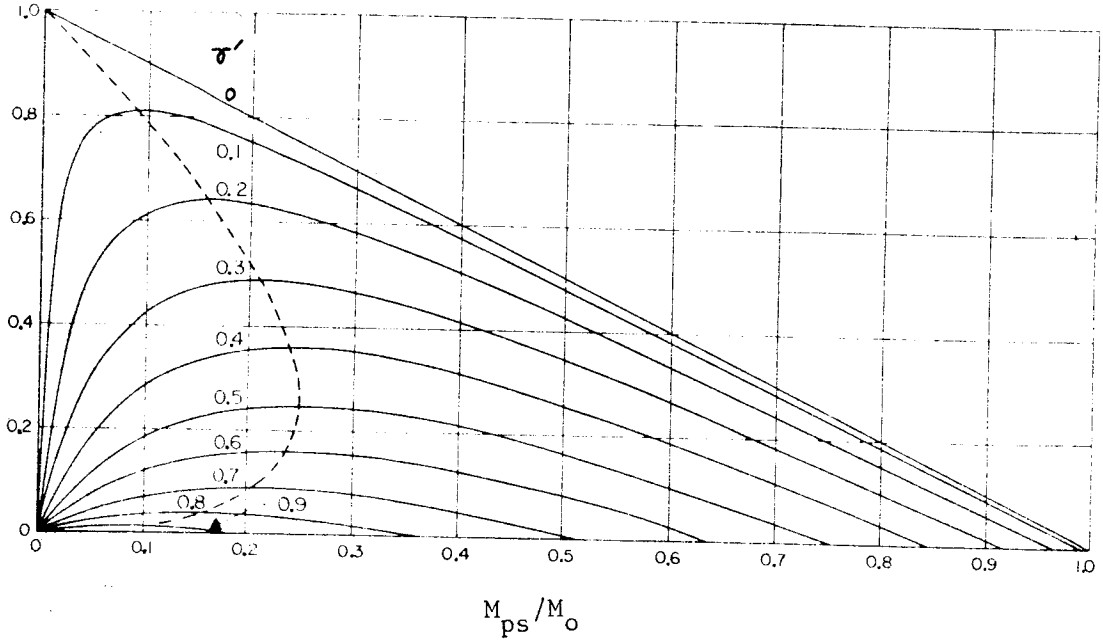

Fig. 4.2 Payload capacity of conventional electric spacecraft with negligible tankage.

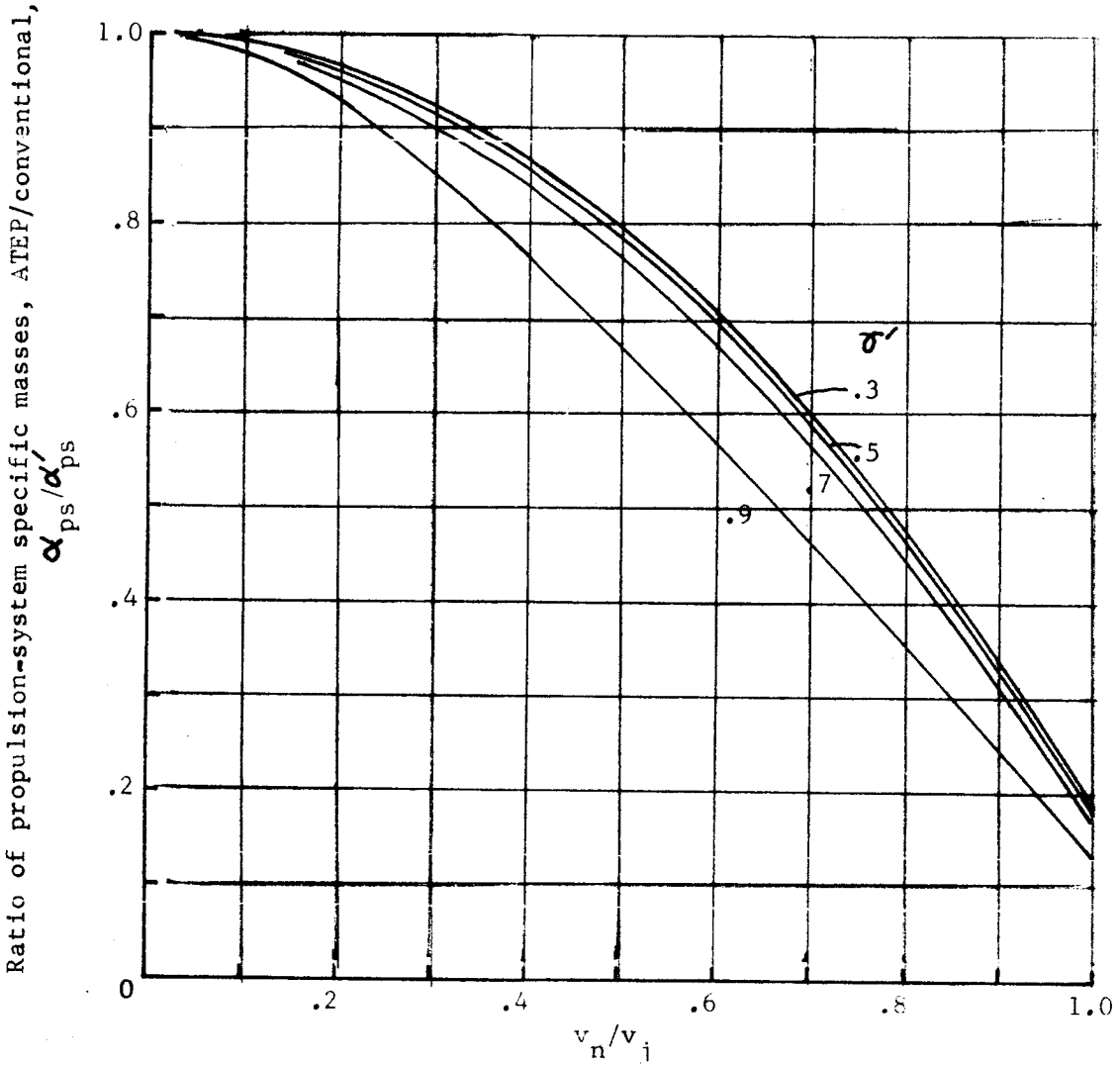

Fig. 4.3 Comparison of ATEP system with conventional electric propulsion system. $\alpha_n/\alpha_{pp} = 0.01$, $\alpha_r/\alpha_{pp} = 0.1$, $\alpha_{th}/\alpha_{pp} = 0.05$, $\eta_n = 0.5$, $\eta_{th} = 0.9$, $k = 0.1$.

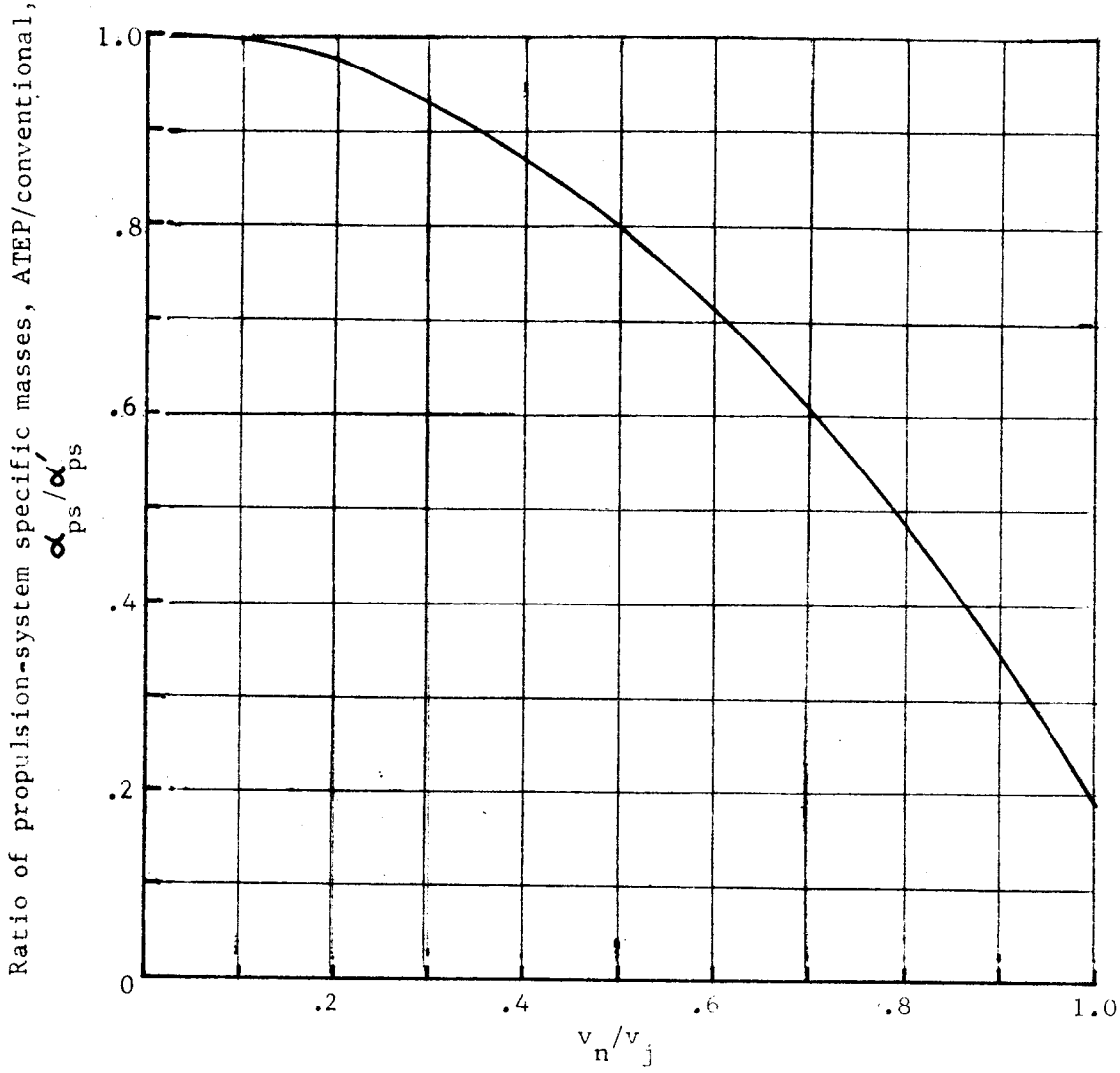

Fig. 4.4 Comparison of ATEP system with conventional electric propulsion system. $\alpha_n/\alpha_{pp} = 0.01$, $\alpha_r/\alpha_{pp} = 0.1$, $\alpha_{th}/\alpha_{pp} = 0.05$, $\eta_n = 0.5$, $\eta_{th} = 0.9$, $k = 0$.

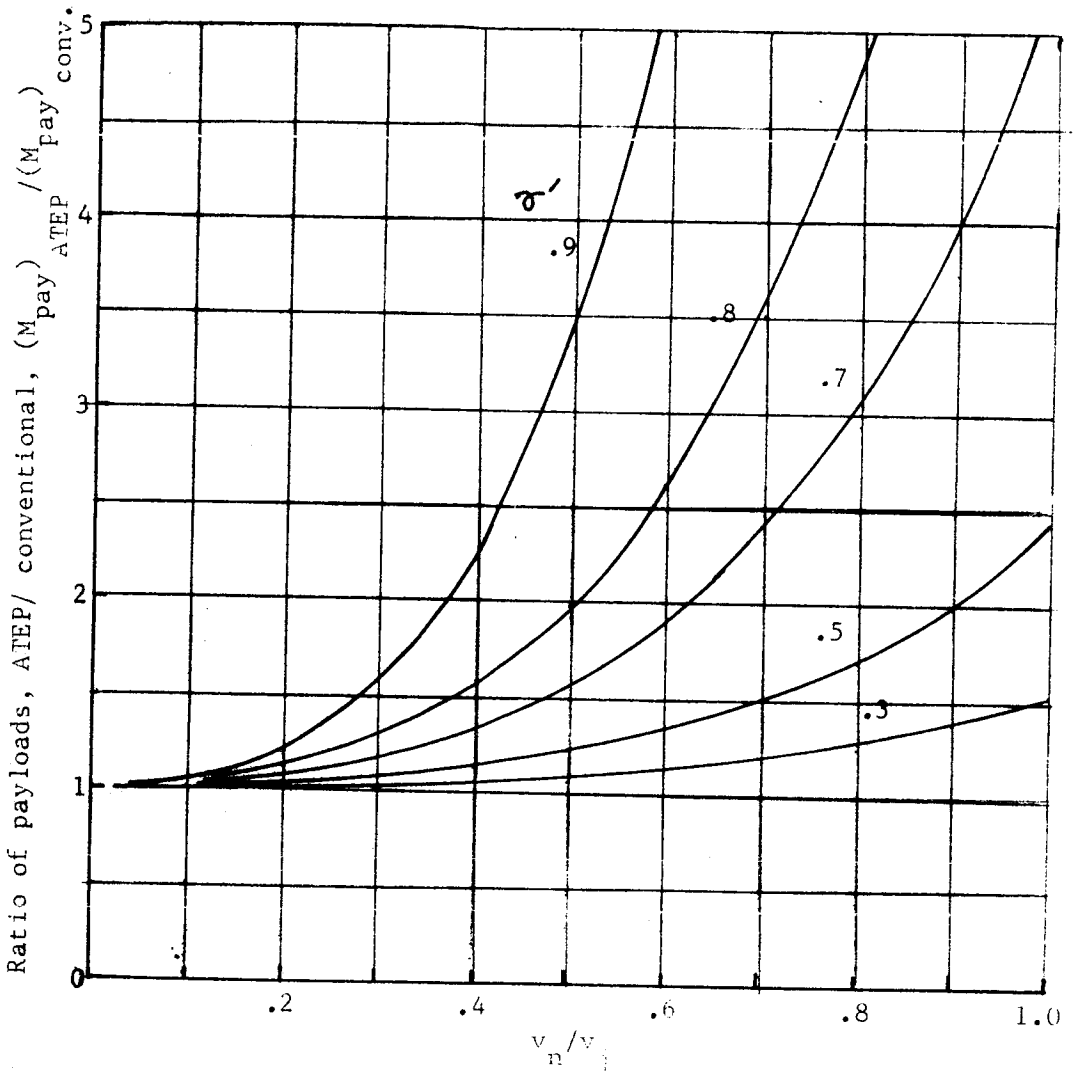

Fig. 4.5 Payload capacity of ATEP system.

APPLICATIONS OF THE ATEP CONCEPT

by Daniel C. Garvey and William R. Mickelsen

Analysis of the ATEP concept in the preceding section has shown that significant improvement in mission performance would be possible if the ATEP concept could be applied to real electric propulsion systems. Because of this promise it is of interest to examine the general feasibility of using electrostatic, electrothermal thrusters in the ATEP concept. Preliminary results of this examination are discussed in this section.

Electrostatic Thrusters

The basic mode of operation of the ATEP system is described by Figure 4.1 of the previous section. A nuclear reactor is part of the thermodynamic system that provides electric power for the electrostatic thruster. In the assumed thruster model, liquid lithium propellant flows from the propellant tank through the reactor, where it is heated, producing lithium vapor with a small degree of ionization. Lithium was chosen for this analysis because of its advantage as a reactor coolant and because of its low molecular weight and good tankage properties. Upon leaving the reactor, the lithium molecules are accelerated by the nozzle to a supersonic velocity. The electrostatic thruster model chosen for analysis here is a colloid-particle thruster concept in which colloid particles are formed in the nozzle flow in a condensation region, as described in the next section. After leaving the nozzle, the colloid particles are assumed to be charged in a charging chamber, and subsequently accelerated in an electrostatic accelerator.

The Supersonic Nozzle. The purpose of the supersonic nozzle in Sketch A is to convert the gas enthalpy at stagnation conditions T_o and p_o into kinetic energy at the nozzle exit plane. (Symbols are defined in the symbol list at the end of this section):

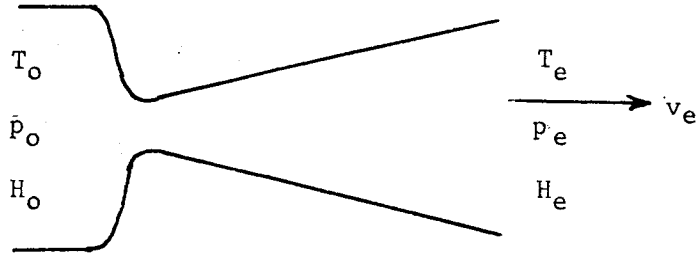

Sketch A

Assuming that the lithium vapor is an ideal monatomic gas, and that the flow is one demensional and isentropic, the velocity at the exit plane can be determined from an energy balance:

$$v_e = \left[2Jg\ (H_o - H_e)\right]^{\frac{1}{2}} \tag{5.1}$$

The stagnation enthalpy for an ideal monatomic gas is given by [5.1]:

$$H_o = \frac{5}{2}\ (1 + \alpha)\ \frac{R}{m}\ (T_o - T_v) + H_v + H_i \tag{5.2}$$

In equation (5.1), the total heat required to vaporize the gas is given by H_v. Figure 5.1 depicts the lithium propellant vaporization curve [5.2]. The degree of ionization present is given by α and H_i is the enthalpy invested in ionization. For monatomic gases, the relation between the degree of ionization α, temperature T_o and pressure p_o may be obtained from the Saha Equation [5.3]:

$$\log\left(\frac{\alpha^2}{1-\alpha^2}\right) p_o = \frac{-9072E_i}{T_o(^oR)} + \frac{5}{2}\log\frac{T_o(^oR)}{1.8} + \log\frac{2Q^+}{Q} - 6.491 \qquad (5.3)$$

The partition functions Q, Q+ and the ionization potential E_i of the lithium molecule were obtained from the literature[5.4]. In Figure 5.2 the degree of ionization α is plotted for different values of stagnation temperature T_o and pressure p_o. The enthalpy which goes into ionization of the gas is given by [5.1] :

$$H_i = \frac{41526\,\alpha\,E_i}{m} \qquad (5.4)$$

If it is assumed that the propellant does not cool below its vaporization temperature upon expansion in the nozzle, the energy required for vaporization and ionization may be assumed frozen[5.1] :

$$H_f = H_i + H_v \qquad (5.5)$$

The stagnation enthalpy is then given by:

$$H_o = \frac{5}{2}(1+\alpha)\frac{R}{m}(T_o - T_v) + H_f \qquad (5.6)$$

The enthalpy at the exit plane (H_e) is composed of energy frozen in the flow due to vaporization and ionization (H_f) and thermal energy H_t remaining in the flow:

$$H_e = H_t + H_f \qquad (5.7)$$

Rewriting equation (5.2) and applying equations (5.5), (5.6) and (5.7), the velocity at the nozzle exit is characterized by:

$$V_e = \left\{ 2Jg \left[\frac{5}{2} (1 + \alpha) \frac{R}{m} (T_o - T_v) - H_t \right] \right\}^{\frac{1}{2}} \tag{5.8}$$

If it is assumed that the area ratio A/A^* is very large, then:

$$\frac{5}{2} (1 + \alpha) \frac{R}{m} (T_o - T_v) \gg H_t \tag{5.9}$$

and

$$\frac{v_e}{g} = \left\{ \frac{2J}{g} \left[\frac{5}{2} \frac{R}{m} (1 + \alpha) (T_o - T_v) \right] \right\}^{\frac{1}{2}} \tag{5.10}$$

The impulse at the nozzle exit plane is described by[5.1] :

$$I_e = \left[\frac{5JR}{gm} (1 + \alpha) (T_o - T_v) \right]^{\frac{1}{2}} \tag{5.11}$$

Figure 5.3 depicts the value of impulse at the nozzle exit plane for various stagnation temperatures T_o and pressures p_o. It is apparent in Figure 5.3 that stagnation conditions of high temperatures ($T_o \geq 2000^oK$) and low pressures ($p_o \leq 10^3 \frac{\text{dynes}}{\text{cm}^2}$) are desirable for large nozzle specific impulse ($I_e \geq 300$ sec.) with a low molecular weight lithium propellant. The exit Mach number associated with the nozzle specific impulse at various stagnation temperatures is described by Figure 5.4.

Ionization Chamber. Atomic lithium particles enter the ionization chamber traveling at a velocity v_e obtained from acceleration by the supersonic nozzle. In the model ionization chamber, it is assumed that charging and homogenous condensation occur at velocity v_e. The charged colloidal particles leave the chamber at a velocity v_e. (Sketch B)

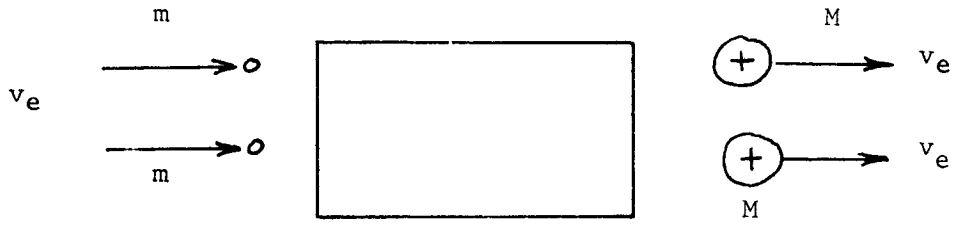

Sketch B

Electrostatic Thruster. Upon exiting the ionization chamber, the charged colloidal particles enter the electrostatic thruster at a velocity v_e. (Sketch C)

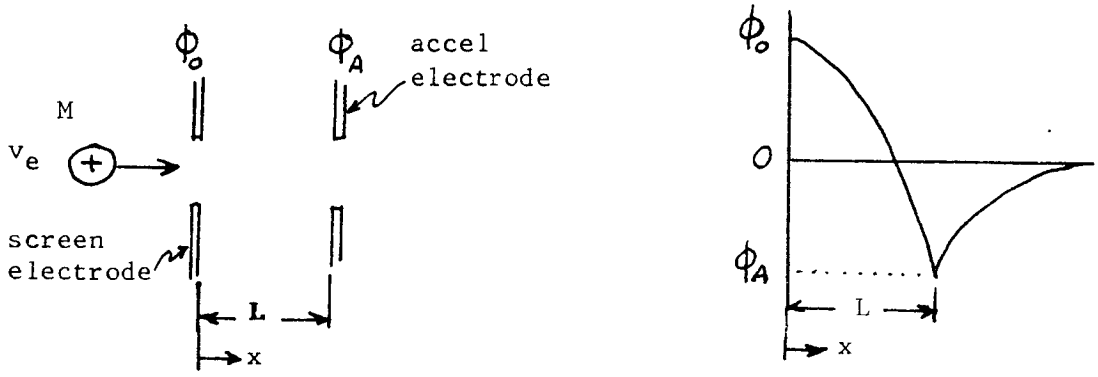

Sketch C

The charged particle equation of motion is obtained from Sketch C:

$$M \frac{dv}{dt} = qE = -q \frac{d\phi}{dx} \tag{5.12}$$

With the integration of equation 5.12 and application of the boundary conditions $\phi = \phi_o$ and $v = v_e$, equation 5.12 can be integrated:

$$\frac{M}{2} (v^2 - v_e^2) = -q (\phi - \phi_o) \tag{5.13}$$

The particle velocity in equation (5.13) is characterized by:

$$v = \left[\frac{2q}{M} (\phi_o - \phi) + v_e^2 \right]^{\frac{1}{2}} \tag{5.14}$$

The kinetic energy of the charged particle entering the thruster is equivalent to a potential energy:

$$\frac{1}{2} M v_e^2 = q \phi_T \tag{5.15}$$

Expressing the initial particle velocity v_e in terms of potential energy:

$$v_e^2 = \frac{2q \phi_T}{M} \tag{5.16}$$

The particle velocity in the thruster may be expressed as:

$$v = \left[\frac{2q}{M} (\phi_o + \phi_T - \phi) \right]^{\frac{1}{2}} \tag{5.17}$$

From Poisson's Equation in one dimension:

$$\frac{d^2\phi}{dx^2} = -\frac{\sigma}{\epsilon_o} \tag{5.18}$$

an expression relating the potential and the charge density is obtained. The charge density is also related to the current density j and the particle velocity v:

$$\sigma = jv \tag{5.19}$$

Applying equations (5.17) and (5.19), Poisson's Equation may be written in the form:

$$\frac{d^2\phi}{dx^2} \qquad \frac{-j}{\epsilon_o \left[\frac{2q}{M}(\phi_o + \phi_t - \phi)\right]^{\frac{1}{2}}} \tag{5.20}$$

Solution of equation (5.20) for one dimensional space-charge-limited flow of charged particles will result in the maximum current density j. The space-charge-limited condition is met in the thruster when the following boundary conditions are satisfied:

$$\text{at } X = 0 \qquad \phi = \phi_o \quad \& \quad \frac{d\phi}{dx} = E = 0$$

$$\text{at } X = L \qquad \phi = \phi_A$$

With the integration of equation (5.20) and the application of the boundary conditions, the space-charge-limited current density is characterized by:

$$j = \frac{4\sqrt{2}}{9} \frac{\epsilon_o}{L^2} \sqrt{\frac{q}{M}} (\phi_o - \phi_A)^{3/2} \left[(\beta + 1)^{\frac{1}{2}} + 2\beta^{\frac{1}{2}} \right]^2 \left[(\beta + 1)^{\frac{1}{2}} - \beta^{\frac{1}{2}} \right] \quad (5.21)$$

where

$$\beta = \frac{\phi_t}{\phi_o - \phi_A} = \frac{1}{2} \frac{Mv_e^2}{q} \frac{1}{(\phi_o - \phi_A)} \quad (5.22)$$

For the case of zero initial particle velocity

$$\phi_T = \beta = 0$$

and the current density is given by the Child-Langmuir Law [5.5] :

$$j_o = \frac{4\sqrt{2}}{9} \frac{\epsilon_o}{L^2} \sqrt{\frac{q}{M}} (\phi_o - \phi_A)^{3/2} \quad (5.23)$$

From equations (5.21), (5.22) and (5.23), it may be observed that for increasing values of v_e, a larger current density may be obtained while maintaining the thruster parameters constant. Alternatively, for increasing values of v_e, a constant value of current density may be achieved for decreasing thruster area, again maintaining thruster parameters constant. A plot of current density ratio obtained from equations (5.21) and (5.23) is given in Figure 5.4.

Evaluation of the ATEP Model. In the evaluation of the performance of the ATEP system, two ideal propulsion systems utilizing charged colloidial particles were compared: electrostatic versus thermally-augmented electrostatic. The mass flow rate in the colloid thruster is related to the current density by :

$$\frac{\dot{M}}{A_t} = \frac{M}{q} \; j \tag{5.24}$$

Also, the static thruster jet power/area is characterized by:

$$\frac{P_j}{A_t} = \frac{\dot{M}}{A_t} \cdot \frac{v_j^2}{2} \tag{5.25}$$

The current density in the thruster is space charge limited and for the case of initial particle velocity v_e, j is given by equation (5.21): (5.21)

$$j = \frac{4\sqrt{2}}{9} \frac{\epsilon_o}{L^2} \sqrt{\frac{q}{M}} (\phi_o - \phi_A)^{3/2} \left[(\beta + 1)^{\frac{1}{2}} + 2\beta^{\frac{1}{2}}\right]^2 \left[(\beta + 1)^{\frac{1}{2}} - \beta^{\frac{1}{2}}\right]$$

where

$$\beta = \frac{M v_e^2}{2q (\phi_o - \phi_A)}$$

and

$$\phi_o = \frac{M}{2q} v_j^2$$

The exhaust jet power per unit area in the thermally augmented electrostatic thruster is obtained from equations (5.21), (5.24), and (5.25): (5.26)

$$\left(\frac{P_j}{A_t}\right)_{ATEP} = \frac{4\sqrt{2}}{9} \frac{\epsilon_o}{L^2} \sqrt{\frac{M}{q}} (\phi_o - \phi_A)^{3/2} \left[(\beta + 1)^{\frac{1}{2}} + 2\beta^{\frac{1}{2}}\right]^2 \left[(\beta + 1)^{\frac{1}{2}} - \beta^{\frac{1}{2}}\right] \frac{v_j^2}{2}$$

In a similar manner, the current density for the case of zero initial particle velocity is space charge limited and is described

by the Child-Langmuir Law:

$$j_o = \frac{4\sqrt{2}}{9} \frac{\epsilon_o}{L^2} \sqrt{\frac{q}{M}} (\phi_o - \phi_A)^{3/2} \tag{5.23}$$

where $$\phi_o = \frac{M v_j^2}{2q}$$

The exhaust jet power per unit area in the electrostatic thruster is characterized by:

$$\left(\frac{P_j}{A_t}\right)_{EP} = \frac{4\sqrt{2}}{9} \frac{\epsilon_o}{L^2} \sqrt{\frac{M}{q}} (\phi_o - \phi_A)^{3/2} \frac{v_j^2}{2} \tag{5.27}$$

From Equations (5.26) and (5.27), the jet power per unit area may be expressed in a dimensionless form for similar thrusters:

$$\left(\frac{P_j}{A_t}\right)_{ATEP} \Big/ \left(\frac{P_j}{A_t}\right)_{EP} = \left[(\beta + 1)^{\frac{1}{2}} + 2\beta^{\frac{1}{2}}\right]^2 \left[(\beta + 1)^{\frac{1}{2}} - \beta^{\frac{1}{2}}\right] \tag{5.28}$$

where

$$\beta = \frac{M v_e^2}{2q (\phi_o - \phi_A)}$$

and

$$\phi_o = \frac{M v_j^2}{2q}$$

In accel-decel accelerators, a voltage ratio ψ can be defined:

$$\psi \equiv \frac{\phi_o - \phi_A}{\phi_o} \tag{5.29}$$

Then, the parameter β becomes:

$$\beta = \frac{v_e^2}{\psi v_j^2} = \frac{I_e^2}{\psi I_j^2} \tag{5.30}$$

The exhaust jet power/area described by Equations (5.28), (5.29) and (5.30) is plotted in Figures 5.5 and 5.6.

As a result of the model analysis, it is realized that an increased jet power/area is achieved in colloid-particle electro-static thrusters employing the ATEP system.

Electrothermal Thrusters

Application of electrothermal thrusters to the ATEP system concept requires the addition of heat to a supersonic stream as mentioned in Section 4. It is of interest to evaluate the theoretical performance of electrothermal thrusters having supersonic inlet velocities.

The operating mode of the propulsion system is depicted by Figure 5.7. A nuclear reactor is part of the thermodynamic cycle which provides power for the electrical heating of the propellant. Lithium was again selected as the propellant for reasons discussed previously. After cooling the reactor, the propellant is accelerated by the nozzle to a supersonic Mach number M_e.

In the present work the effects of propellant ionization and dissociation are not considered. The propellant upon exiting the nozzle enters the heat-addition region of the thruster, where heat is added to the supersonic stream. Employing the mathematical relations of Crocco[5.6], several cases of heat addition to a supersonic stream are considered. It is intended that the performance of the electrothermal thruster be evaluated from the view-

point of the decrease in stagnation pressure ratio for several cases of heat addition and the resultant effect on mission specific impulse I_j.

Supersonic Nozzle. - In the model the nozzle is depicted by Sketch D.

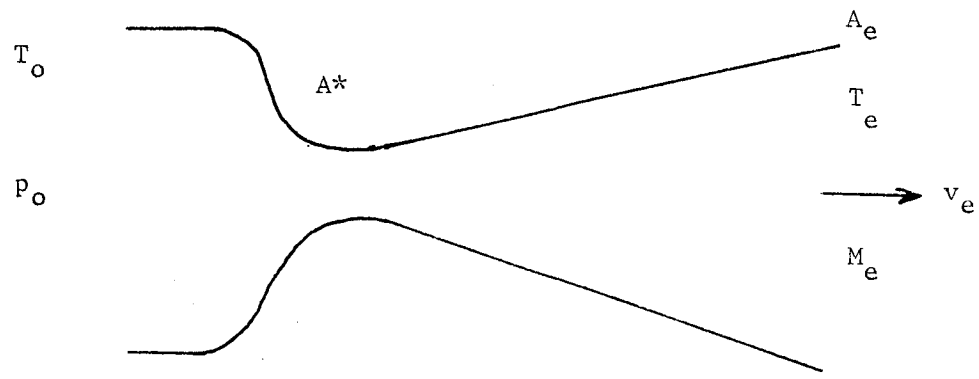

Sketch D.

For the case of steady one dimensional flow through the ideal nozzle the exhaust velocity as obtained from the conservation of energy equation is described by:

$$v_e = \sqrt{2c_p(T_o - T_e)} \tag{5.31}$$

Considering the nozzle flow to be reversible and adiabatic the isentropic relations are employed for various area ratios A_e/A^* and stagnation temperatures T_o to determine the exit Mach number M_e and the specific impulse I_e. The results are plotted in Figures 5.8 and 5.9.

Heat Addition Region. - In solving flow problems with heat addition the assumption of constant pressure or constant area is frequently made. The wall force integral in the momentum equation is then conveniently handled. To enlarge the scope of the flow solutions, treatment of cases other than constant pressure or constant area is desirable. A simple relation expressing mathematically the variation of pressure and flow area developed by Crocco[5.6] is characterized by:

$$\frac{p}{p_1} = \left(\frac{A}{A_1}\right)^{\frac{\epsilon}{1-\epsilon}} \tag{5.32}$$

where $\epsilon \equiv$ power index.

The convenience of this relation becomes evident when it is realized[5.7] that a simple integrated form is obtained in the momentum equation along with the cases of constant pressure heat addition ($\epsilon = 0$) and constant area heat addition ($\epsilon = 1$). This arbitrary relation given by Equation 5.32 in no way restricts the duct length. Therefore the area of the heat addition region could be varied with length in such a manner that the heat addition rate yields the assumed variation of pressure with area[5.7]. Hence, the ϵ relation provides an extension of the two more common cases mentioned. Figure 5.10 obtained from the literature[5.7] describes the variation of pressure ratio against area ratio for several values of ϵ .

One dimensional flow of the lithium propellant with heat addition is depicted by Sketch E.

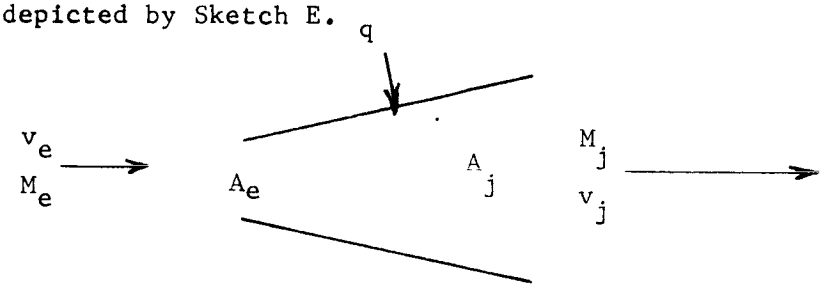

Sketch E

For steady one dimensional flow the conservation of mass equation is given by:

$$\dot{m}_e = \dot{m}_j \tag{5.33}$$

which may be described by:

$$\dot{m} = \rho A v = \frac{pA}{RT} M \tag{5.34}$$

when the gas law and Mach number definition are employed.

Applying the conservation of momentum equation in Sketch E, the following relation is obtained:

$$\dot{m}_j v_j - \dot{m}_e v_e = p_e A_e - p_j A_j + \int_e^j p\,dA \tag{5.35}$$

With the assumption that the Crocco relation holds, the wall force integral in equation (5.35) is characterized by:

$$\int_e^j p\,dA = \int_e^j p_e \left(\frac{A}{A_e}\right)^{\frac{\epsilon}{1-\epsilon}} dA = (1-\epsilon)(p_j A_j - p_e A_e) \tag{5.36}$$

The substitution of this result into equation (5.35) yields:

$$\dot{m}_j v_j + p_j A_j = \dot{m}_e v_e + p_e A_e \tag{5.37}$$

The conservation of energy equation as applied to Sketch E provides:

$$q = h_{oj} - h_{oe} \tag{5.38}$$

Equation (5.38) may be written as:

$$\frac{q}{h_{oe}} + 1 = \frac{T_{oj}}{T_{oe}}$$

when constant specific heats are considered. From equation (5.34):

$$T_j = \left(\frac{p\,A\,M\sqrt{\gamma}}{\dot{m}_j\sqrt{R}}\right)^2 \tag{5.40}$$

then:

$$T_o = \left(\frac{p_j A_j M_j \sqrt{\gamma}}{\dot{m}_j \sqrt{R}}\right)^2 \left(1 + \frac{\gamma-1}{2} M_j^2\right) \tag{5.41}$$

and similar results may be obtained for T_{oe}:

$$T_{oe} = \left(\frac{p_e A_e M_e \sqrt{\gamma}}{\dot{m}_e \sqrt{R}}\right)^2 \left(1 + \frac{\gamma-1}{2} M_e^2\right) \tag{5.42}$$

From the momentum equation:

$$v = M\sqrt{\gamma RT}$$

and using equation (5.34):

$$p_j A_j (M_j^2 \gamma + \epsilon) = p_e A_e (M_e^2 \gamma + \epsilon)$$

which becomes:

$$\frac{p_j A_j}{p_e A_e} = \frac{\epsilon + \gamma M_e^2}{\epsilon + \gamma M_j^2} \tag{5.43}$$

The conservation of energy equation may be rewritten employing equations (5.39), (5.41), (5.42), and (5.43):

$$1 + \frac{q}{h_{oe}} = \frac{M_j^2}{M_e^2} \cdot \frac{(1 + \frac{\gamma - 1}{2} M_j^2)}{(1 + \frac{\gamma - 1}{2} M_e^2)} \cdot \left(\frac{\epsilon + \gamma M_e^2}{\epsilon + \gamma M_j^2} \right)^2 \tag{5.44}$$

or:

$$1 + \frac{q}{h_{o1}} = \frac{N_j^2}{N_e^2} \tag{5.45}$$

where:

$$N = \frac{M \sqrt{1 + \frac{\gamma - 1}{2} M^2}}{(\epsilon + \gamma M^2)} \tag{5.46}$$

Equation (5.46) is plotted in Figures 5.11 and 5.12 for positive and negative values of power index. In Figure 5.11 the Mach number M_j at which thermal choking occurs is obtained[5.7] from equation (5.46):

$$M_j^2 = \frac{1}{\frac{\gamma}{\epsilon} - (\gamma - 1)} \tag{5.47}$$

For $0 \leq \epsilon \leq \gamma/(\gamma - 1)$ all possible values at which thermal choking occurs

are obtained. From Figure 5.12 for negative ϵ it is observed that the Mach number M_j proceeds asymptotically towards[5.7]:

$$M_j = \sqrt{-\frac{\epsilon}{\sigma}} \tag{5.48}$$

The future intent of this analysis is to evaluate the performance of the thruster model from the viewpoint of the decrease in stagnation pressure ratio for several cases of heat addition and the resultant effect upon the mission specific impulse I_j.

Electro-Magnetic Thruster

At this time application of electromagnetic thrusters to the ATEP system has not been considered. It is intended that a model of this system be evaluated in the future.

REFERENCES

5.1 Jack, John R.: Theoretical Performance of Propellants Suitable for Electrothermal Jet Engines. NASA TN D-682, 1961.

5.2 Stull, D.R., and Sinke, G.C.: Thermodynamic Properties of the Elements. Washington, American Chemical Society, 1956.

5.3 Zemansky, Mark: Heat and Thermodynamics. Fourth Edition, McGraw Hill Book Co., Inc., p. 439.

5.4 Allen, C.W.: Astrophysical Quantities. The Athlone Press, Univ. of London.

5.5 Kaufman, Harold R.: One-Dimensional Analysis of Ion Rockets. NASA TN D-261, 1960.

5.6 Crocco, L.: One Dimensional Treatment of Steady Gas Dynamics. Fundamentals of Gas Dynamics, vol. 3 of High Speed Aerodynamics and Jet Propulsion, H.W. Emmons, ed., Princeton University Press, 1958, pp. 100-110.

5.7 Dobrowolski, Andrzej: Analysis of Nonconstant Area Combustion and Mixing in Ramjet and Rocket-Ramjet Hybrid Engines. NASA TN D-3626, 1966.

Symbols

E_i	ionization potential volts
g	gravitational constant
H	enthalpy BTU/lbm
I	specific impulse sec.
J	Joule's constant 778 ft. lb./BTU
L	length in thruster meters
m	particles mass in nozzle flow
M	particle mass in thruster
p	pressure in atmosphere or $\frac{\text{dyne}}{\text{cm}^2}$
q	coulomb charge = 1.6×10^{-19} coulombs
Q	partition function for neutral atom
Q+	partition function for ionized atom
R	universal gas constant
T	temperature ^{o}R or ^{o}K
v	velocity m/sec or ft/sec
$\dot{M}$	mass flow rate
x	distance measurement in thruster meters
α	degreee of ionization
E	field intensity Newton's/coulomb
ϵ_o	permitivity of free space 8.85×10^{-12} $\frac{\text{coulombs}}{\text{Newton m}^2}$
j	current density amp/meter^2
ϕ	potential energy volts
σ	charge density coulomb/meter^3

Subscripts

e	nozzle exit
f	frozen
i	ionization
v	vaporization
o	stagnation

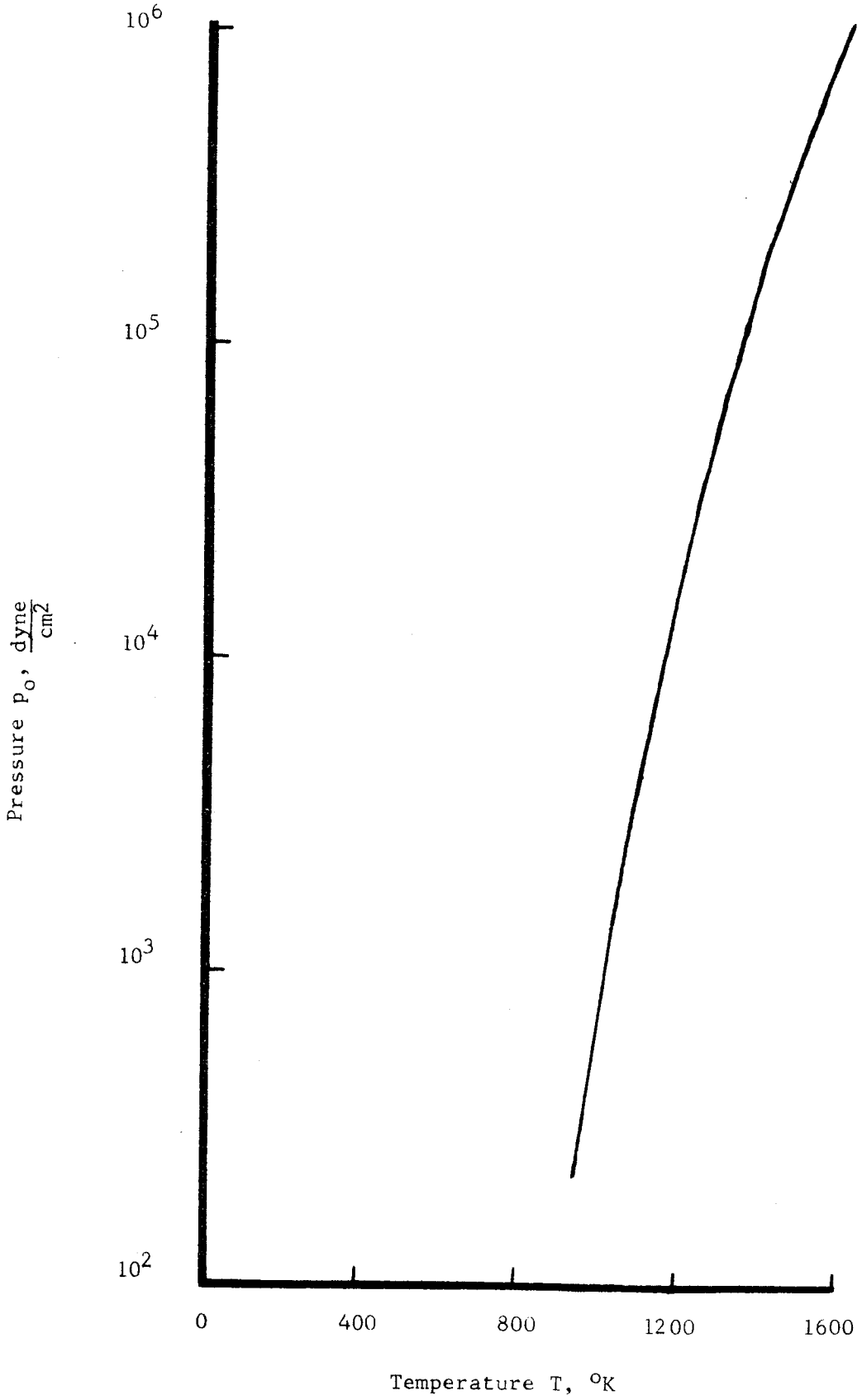

Figure 5.1. Vapor pressure curve for Lithium propellant.

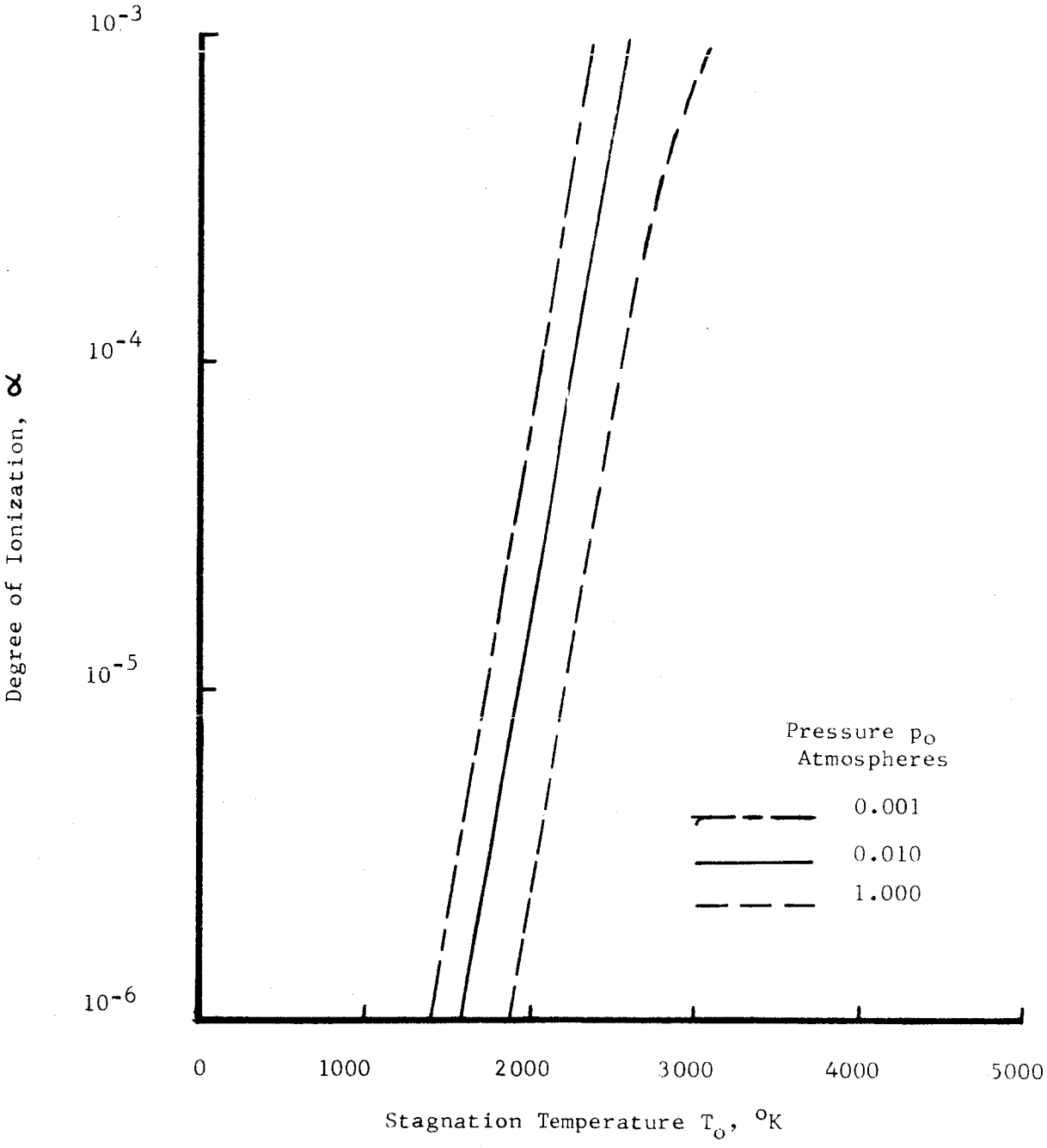

Figure 5.2 Degrees of Ionization for Lithium propellant at stagnation temperature T_o and pressure p_o.

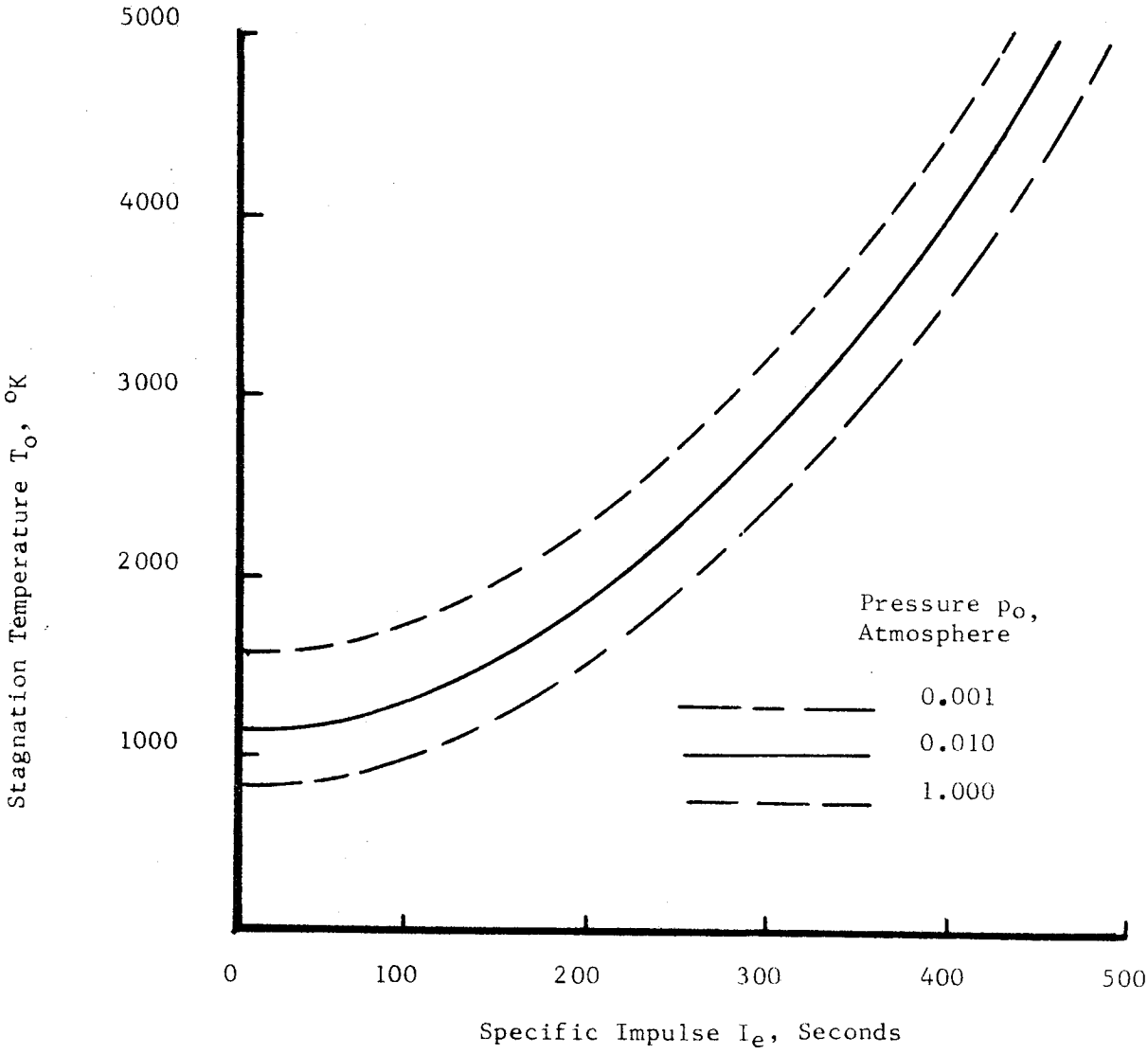

Figure 5.3 Stagnation temperatures for Lithium propellant at pressure p_o.

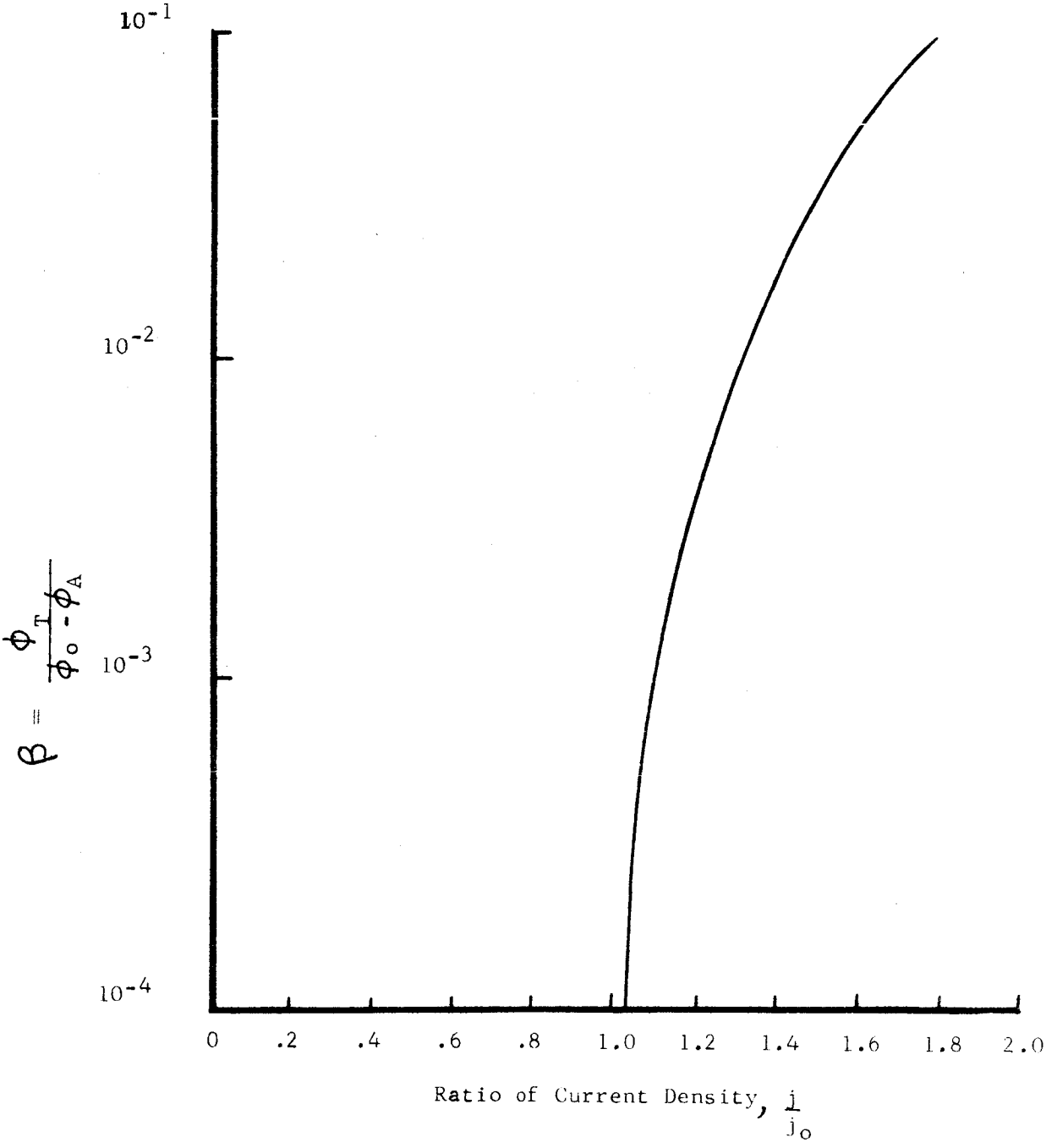

Figure 5.4 Current density ratio as a function of potential voltage ratio β.

$$\Psi \equiv \frac{\phi_o - \phi_A}{\phi_o}$$

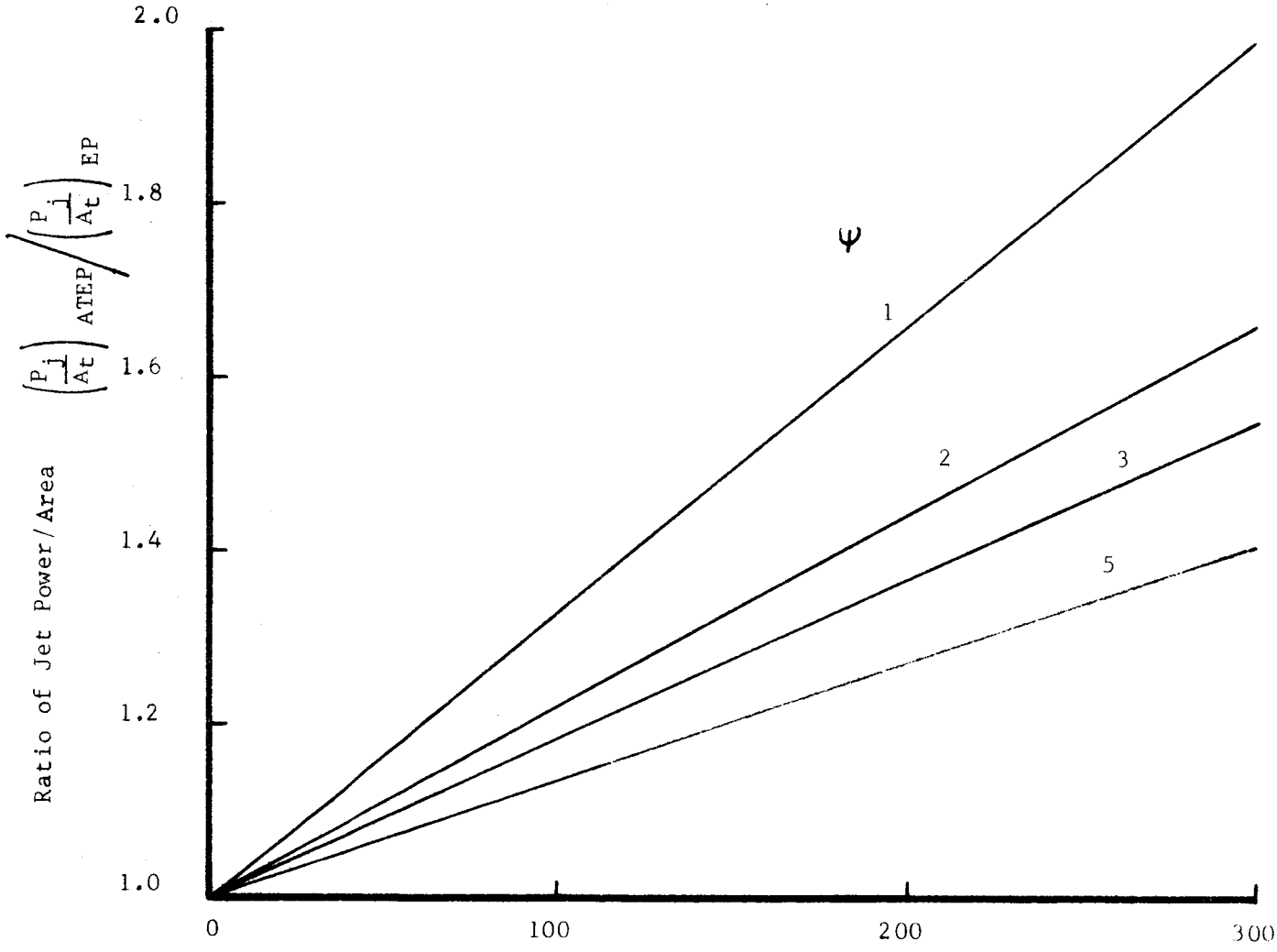

Figure 5.5 Jet power ratio as a function of nozzle specific impulse for I_j = 1000 seconds.

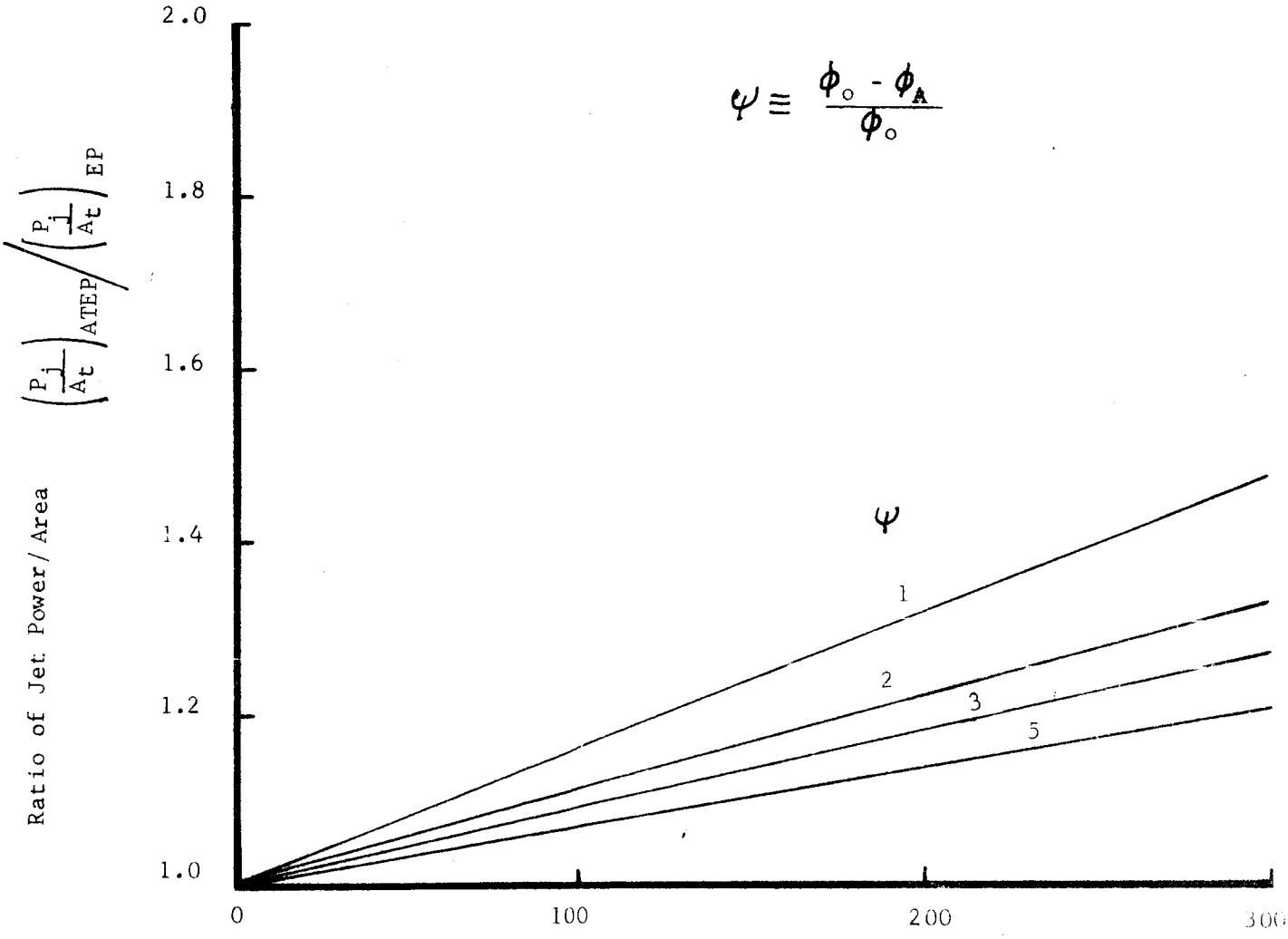

Figure 5.6 Jet power ratio as a function of nozzle specific impulse for I_j = 2000 seconds.

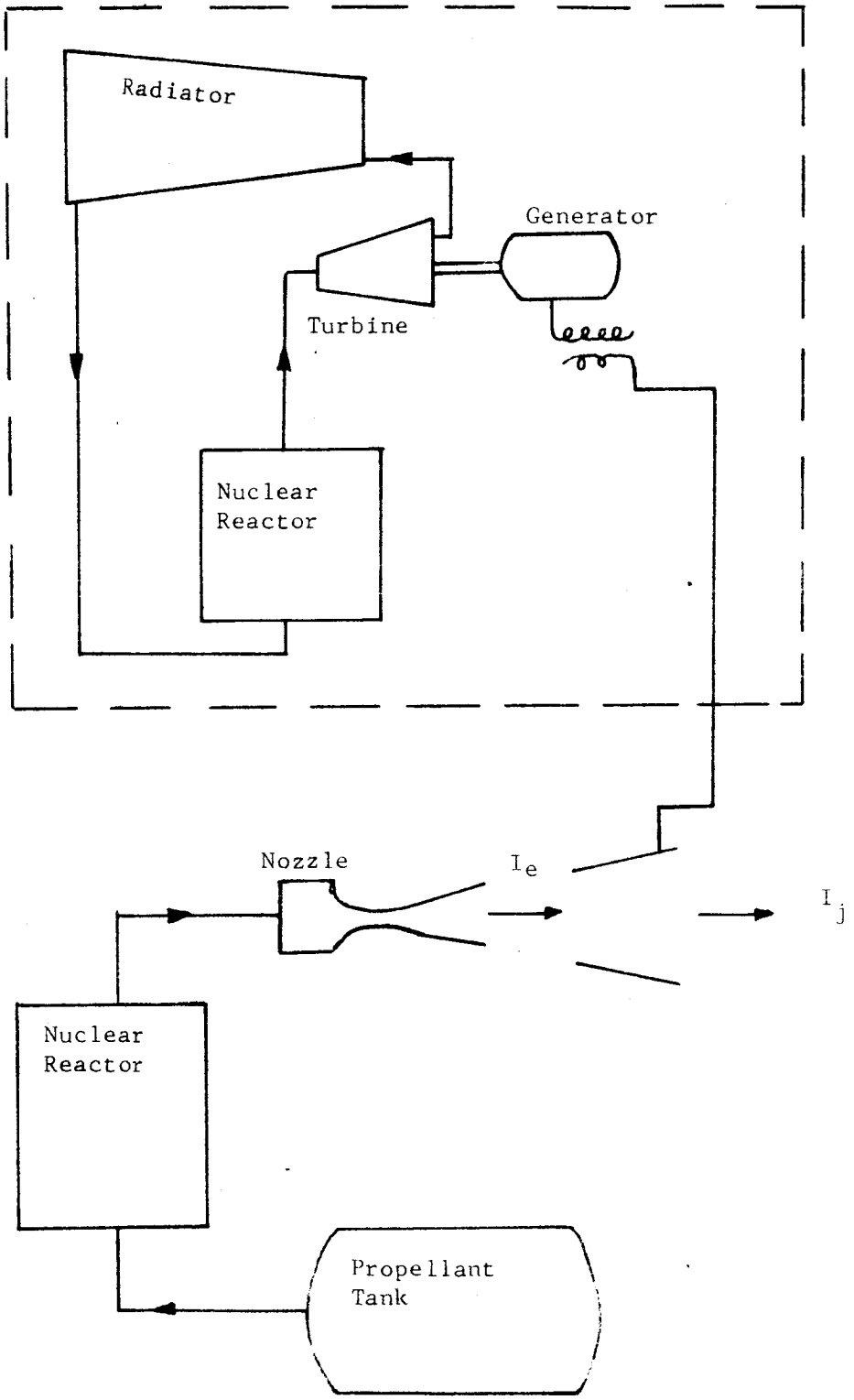

Figure 5.7.A schematic Diagram of an electrothermal thruster in an ATEP system.

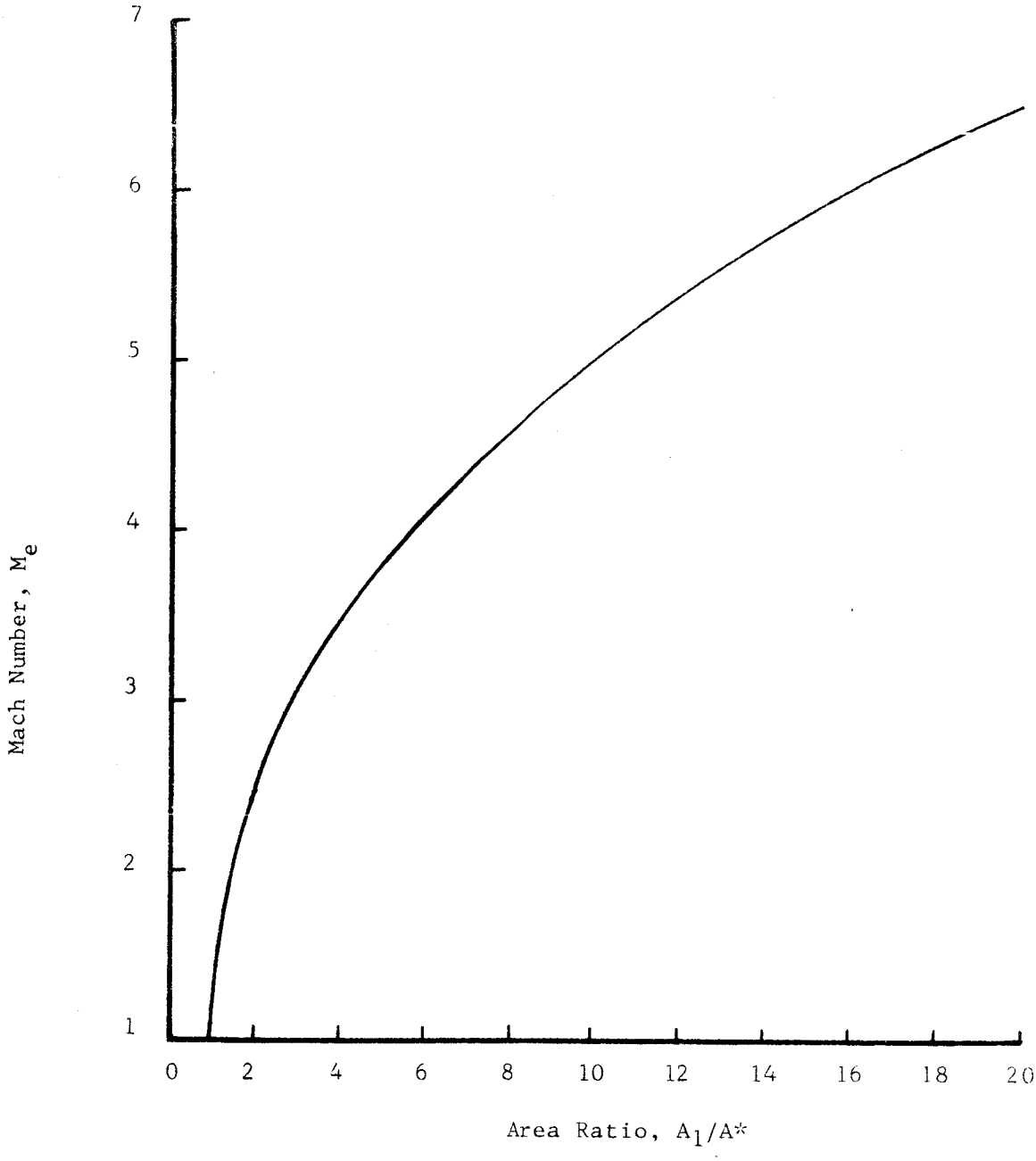

Figure 5.8. Plot of nozzle area ratio versus exit Mach number for an isentropic nozzle, for $\gamma = 1.66$.

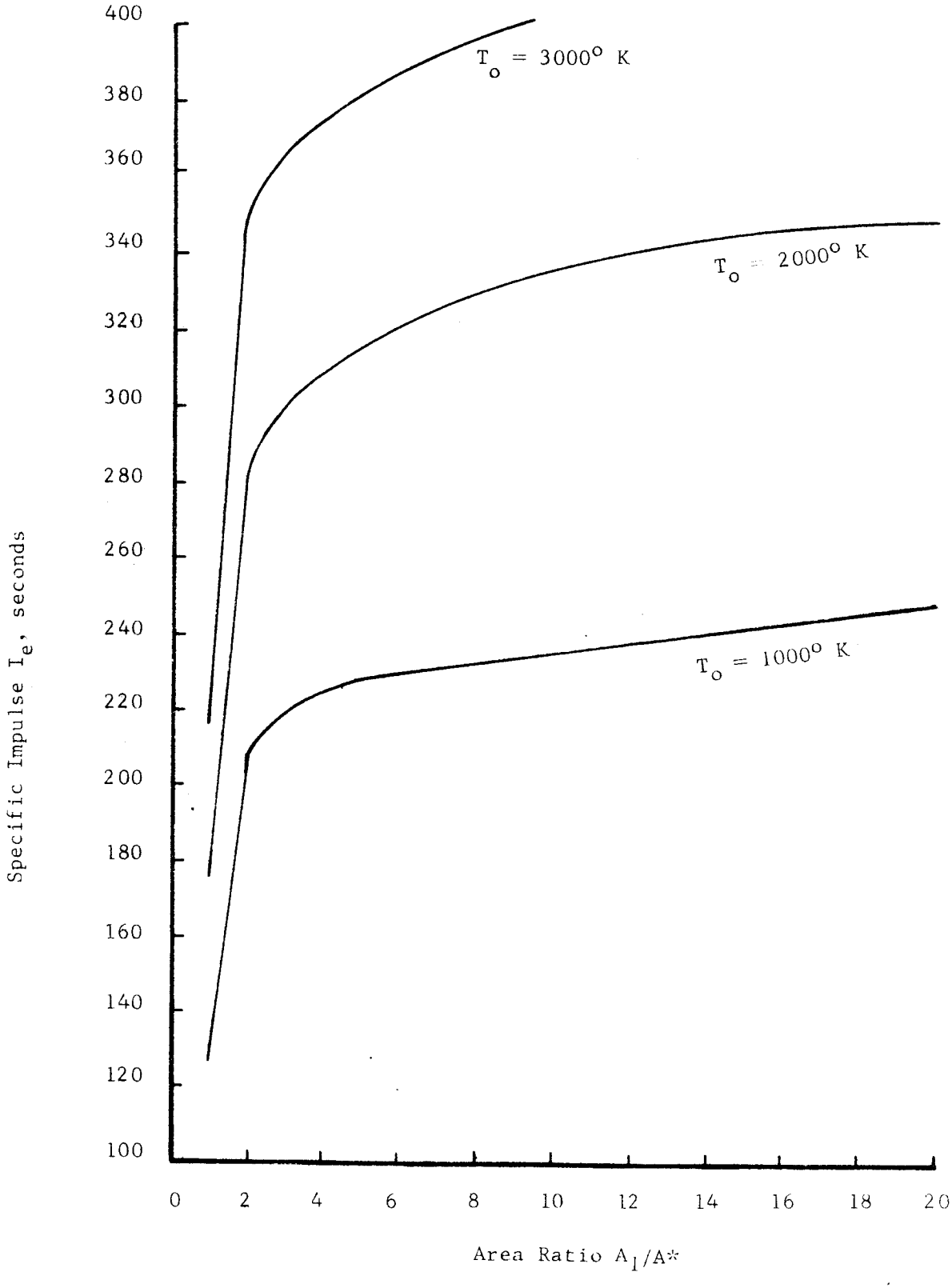

Figure 5.9. Nozzle specific impulse versus area ratio for the isentropic case, for $\gamma = 1.66$

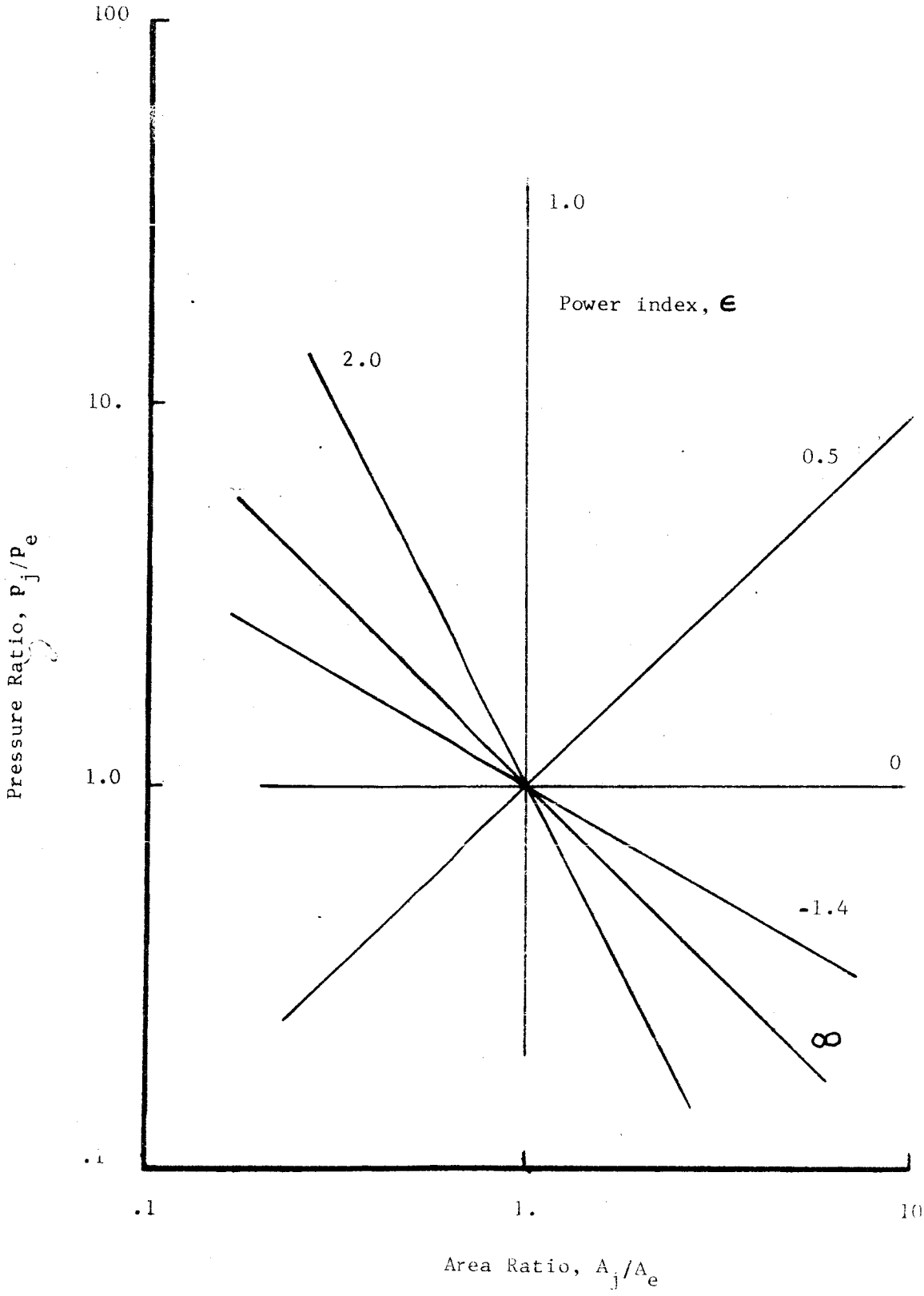

Figure 5.10. The Crocco pressure-area relation.

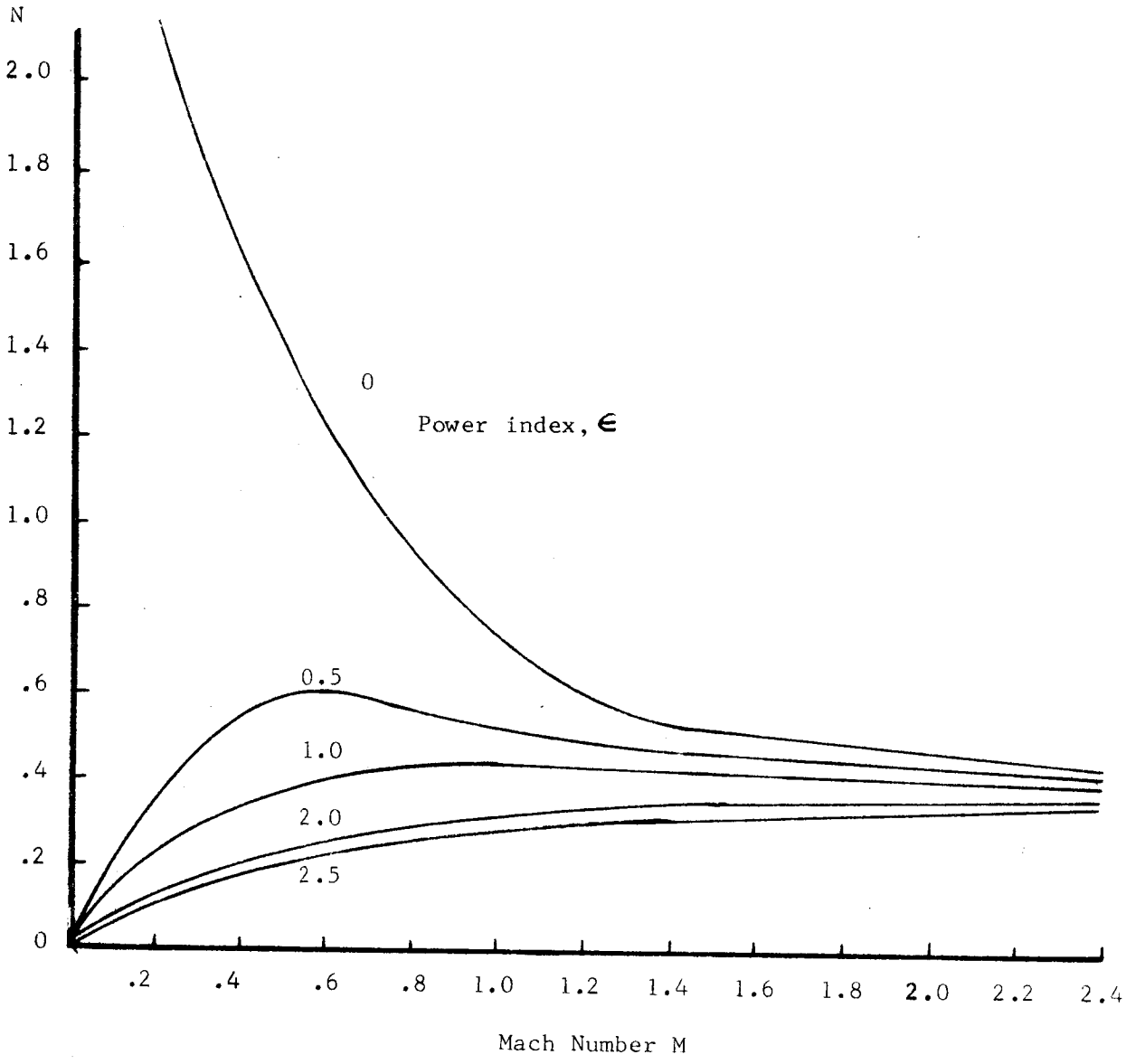

Figure 5.11. Plot of Mach number versus N for positive power index ϵ, with $\gamma = 1.66$

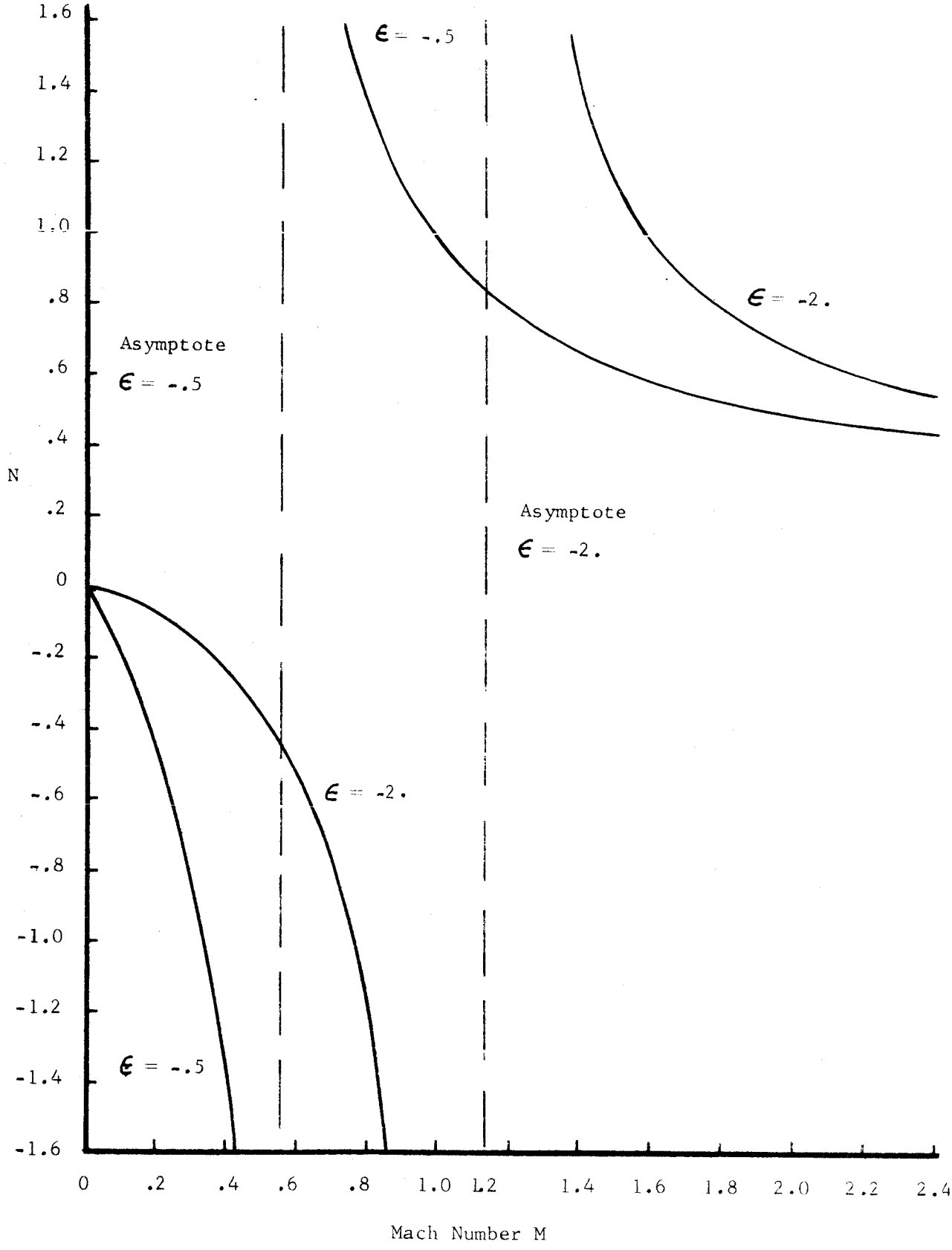

Figure 5.12. Plot of Mach number M versus N for negative power index ϵ, with $\sigma = 1.66$

N67 20515

ALUMINUM COLLOID FORMATION BY HOMOGENEOUS NUCLEATION

By W.R. Mickelsen

The use of final-booster stage spent tankage for propellant in electric spacecraft has been analyzed in Section 3. This generalized mission analysis has shown that payload could be doubled or tripled for many missions if spent tankage could be used for propellant. If upper booster stage tanks are made of aluminum, then it might be possible that the spent tanks could be used as propellant for electric thrusters. Because of payload increases predicted by this preliminary analysis, it is of interest to investigate the feasibility of generating aluminum colloid particles in the size range needed for electrostatic thrusters.

The Frenkel theory of nucleation has been modified and is in good agreement with the condensation of nitrogen in supersonic nozzles having a linear area increase. Nucleation rate as a function of axial distance in a conical supersonic nozzle has been calculated with this theory and is shown in Figure 6.1. Negligible nucleation is predicted until a high degree of supersaturation is reached. Then the calculated nucleation rate rises rapidly to a maximum, and quickly decreases again. This rapid decrease in nucleation rate is attributed to the rise in static stream temperature and pressure resulting from the release of latent heat of vaporization from condensing particles as illustrated in Figure 6.1. If the stream temperature and pressure could be prevented from rising to the saturation line, the nucleation rate should remain high. It seems reasonable that heat rejected to the supersonic stream by the condensing particles could be absorbed in such a way that the stream temperature and pressure would not rise to the saturation line. For example, it seems reasonable

that the cross-sectional area of the duct could be varied such that the temperature and pressure of the stream could be kept well below the saturation line. This situation would be analogous to that encountered in supersonic combustion where heat is added to a supersonic stream.

Modifications are being made to the existing digital computer program to allow calculation of the nozzle shape, which should provide maintenance of high nucleation rate in a greater axial distance than shown in Figure 6.1.

Stream temperatures where theoretical nucleation rate is maximum have been calculated and are shown in Figure 6.2. It is reasonable to expect that nucleation will be much less in very low density flows. Norgren and Goldin have found that nucleation rate is greatly reduced when the nozzle flow is in the slip or free-molecular flow regimes. For laboratory experiments with a 5 milliamp thruster beam current (5 ma is the laboratory power supply limit) and a mean particle diameter of 30 angstroms, a plenum pressure of 0.005 atmospheres or more will be necessary to avoid slip flow. At this pressure, a temperature of about 1800^{o} K would provide slightly superheated conditions in the plenum. For the particle size and beam current specified, nozzle throat diameters would be as shown in Figure 6.3. Nozzle designs for two plenum pressures are shown in Figures 6.4 and 6.5. Also shown are conceptual designs for the charging chamber and the electrostatic accelerator.

Experiments done with nozzles such as these should serve to test the nucleation theory. Particle size distribution would be measured with the quadrupole mass spectrometer. Beam current would be a measure of the rate of formation of nuclei in the nozzle. Nozzle flow calibration would provide

measurement of total flow rate. A wall pressure gage would determine the residual uncondensed vapor leaving the nozzle. These measurements should provide an adequate test of the nucleation theory, and should also be a test of feasibility of colloid particle generation from aluminum vapor.

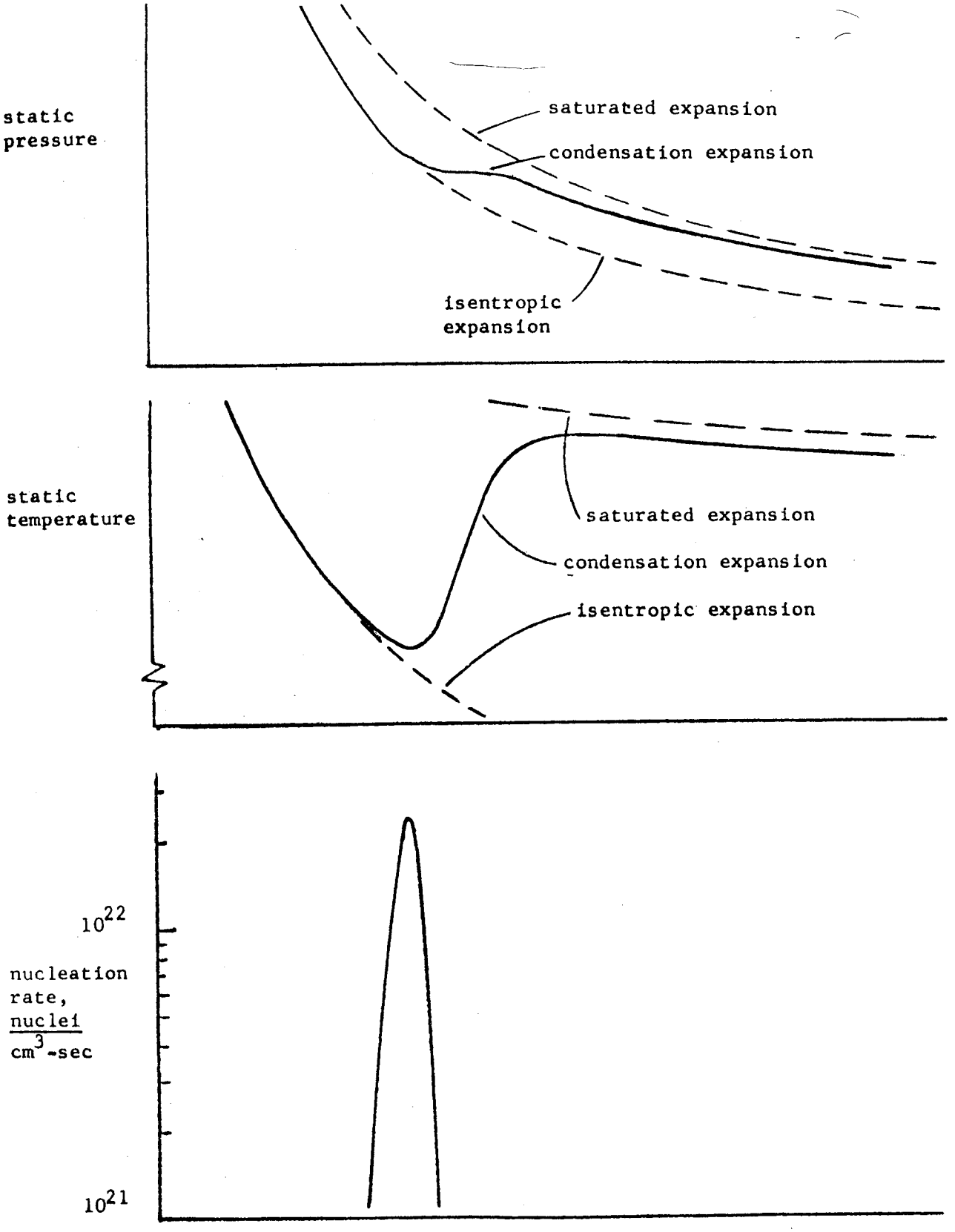

Figure 6.1 - Pressure, temperature, and nucleation rate in homogeneous condensation in conical supersonic nozzles.

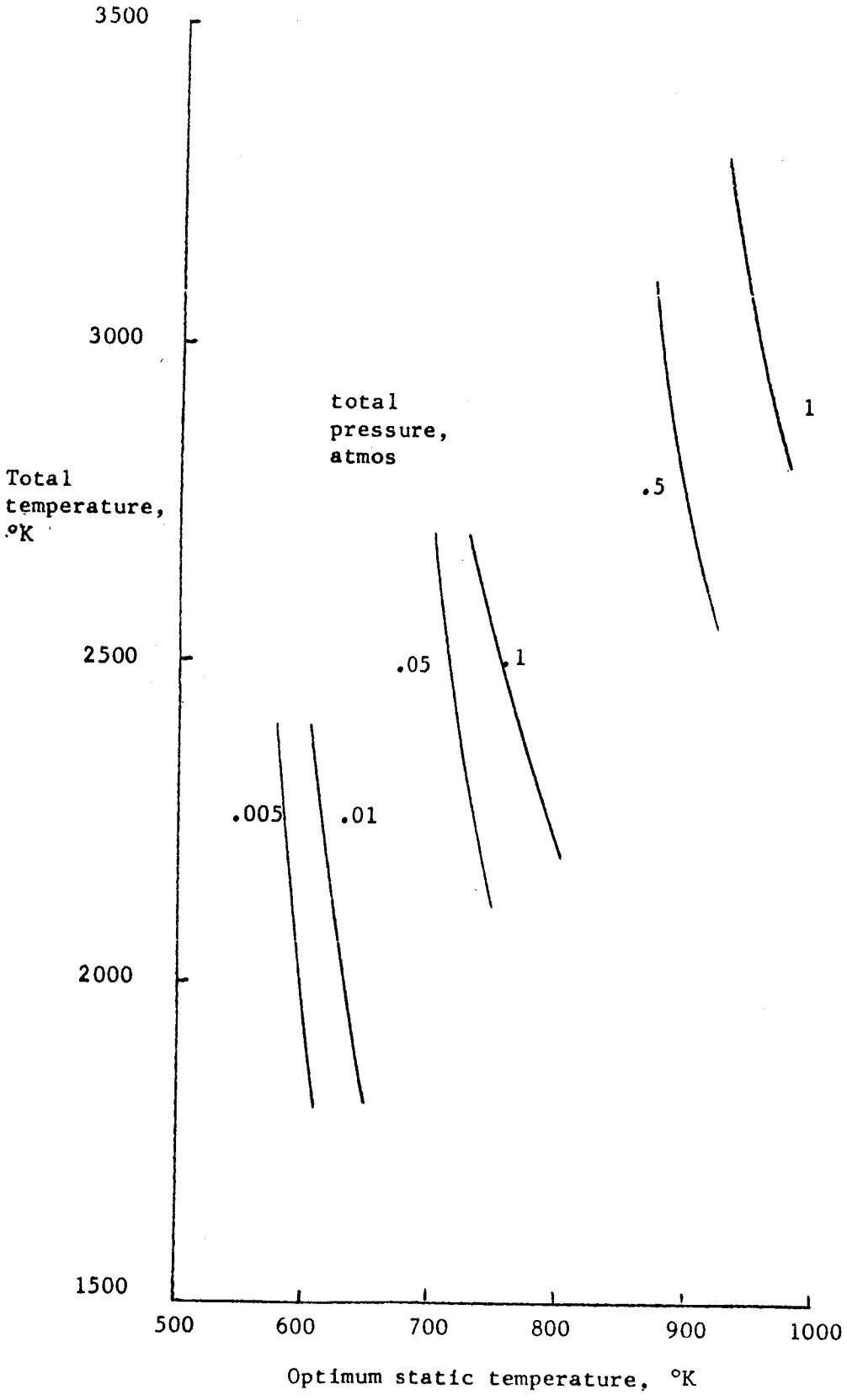

Fig. 6.2 - Optimum static temperature for maximum nucleation rate of aluminum vapor.

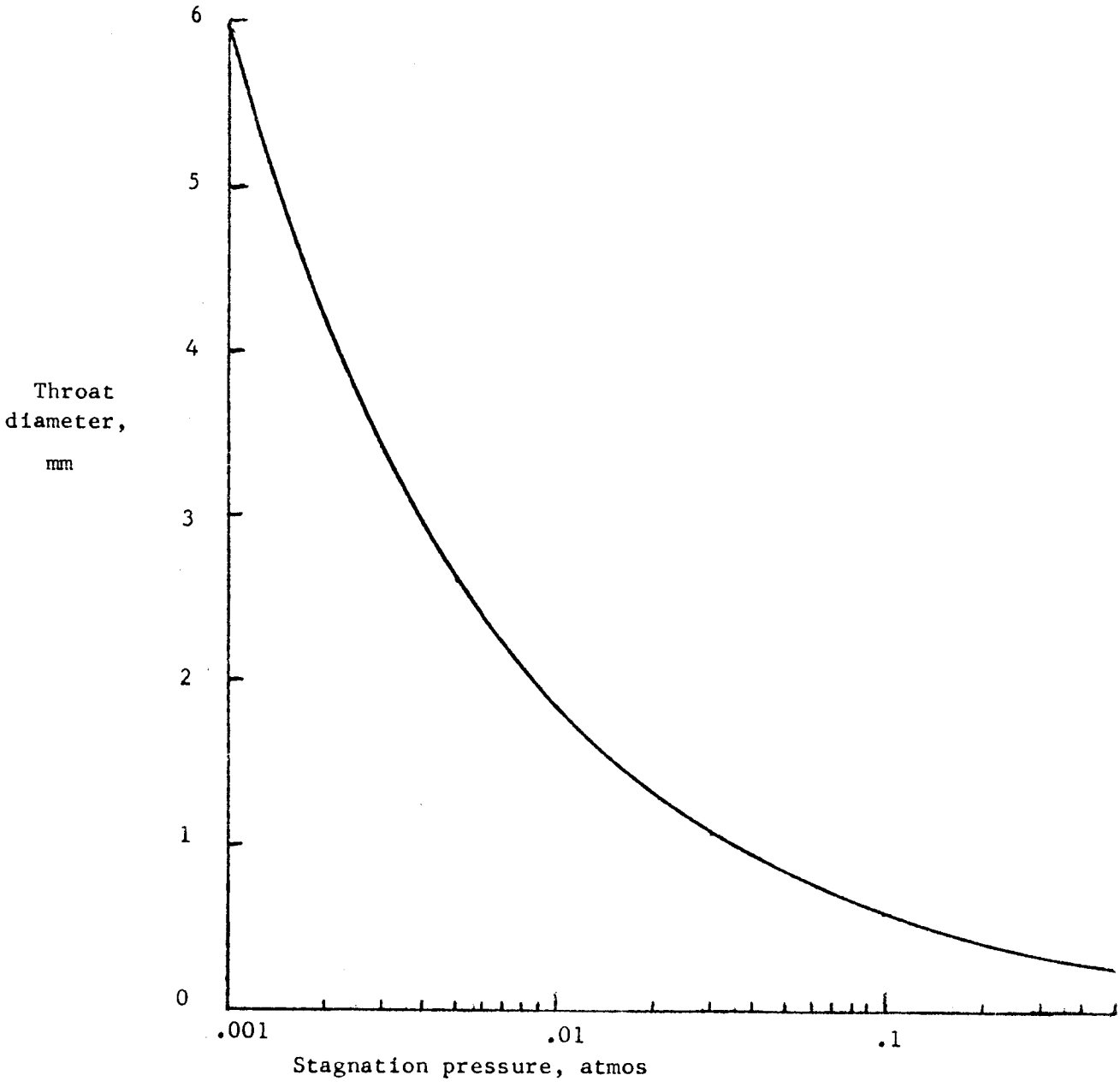

Figure 6.3 - Nozzle throat diameters for aluminum-vapor supersonic nozzle stagnation temperature, 2000°K.

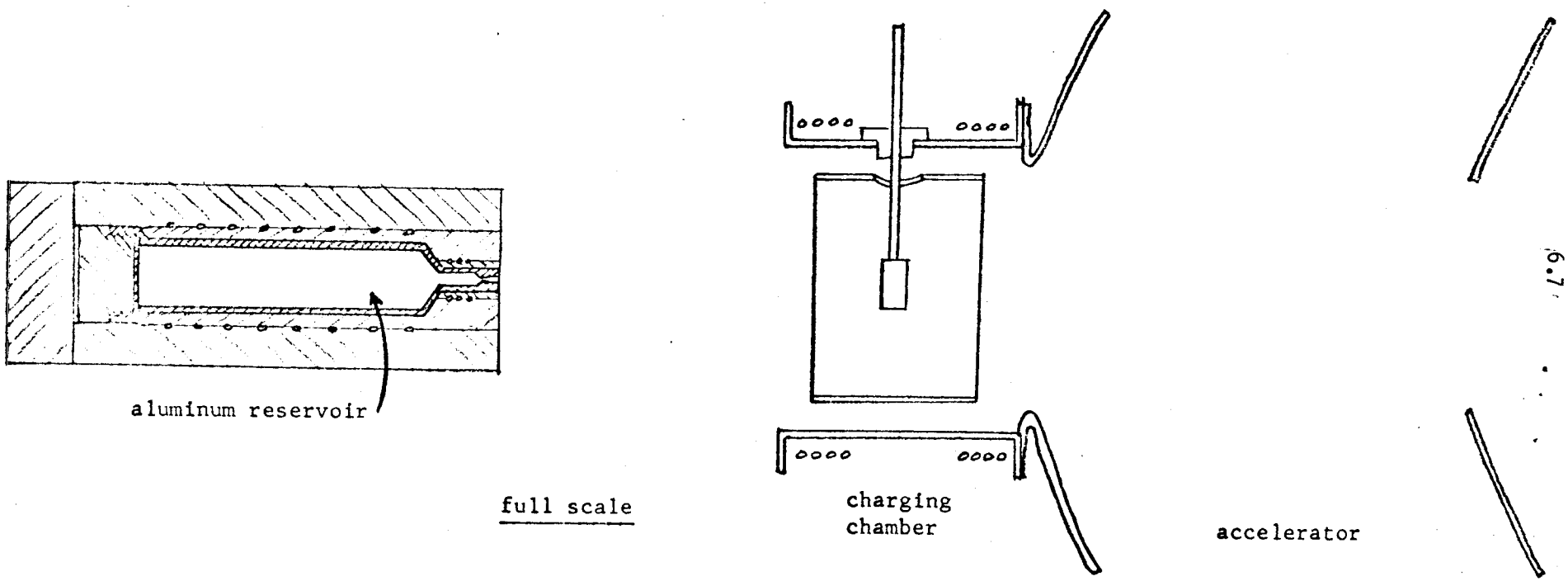

Figure 6.4 - Preliminary design of aluminum colloid thruster. Design paramters: 5 ma beam current, 0.1 atmos plenum pressure, 2200°K plenum temperature, 0.62 mm throat diameter.

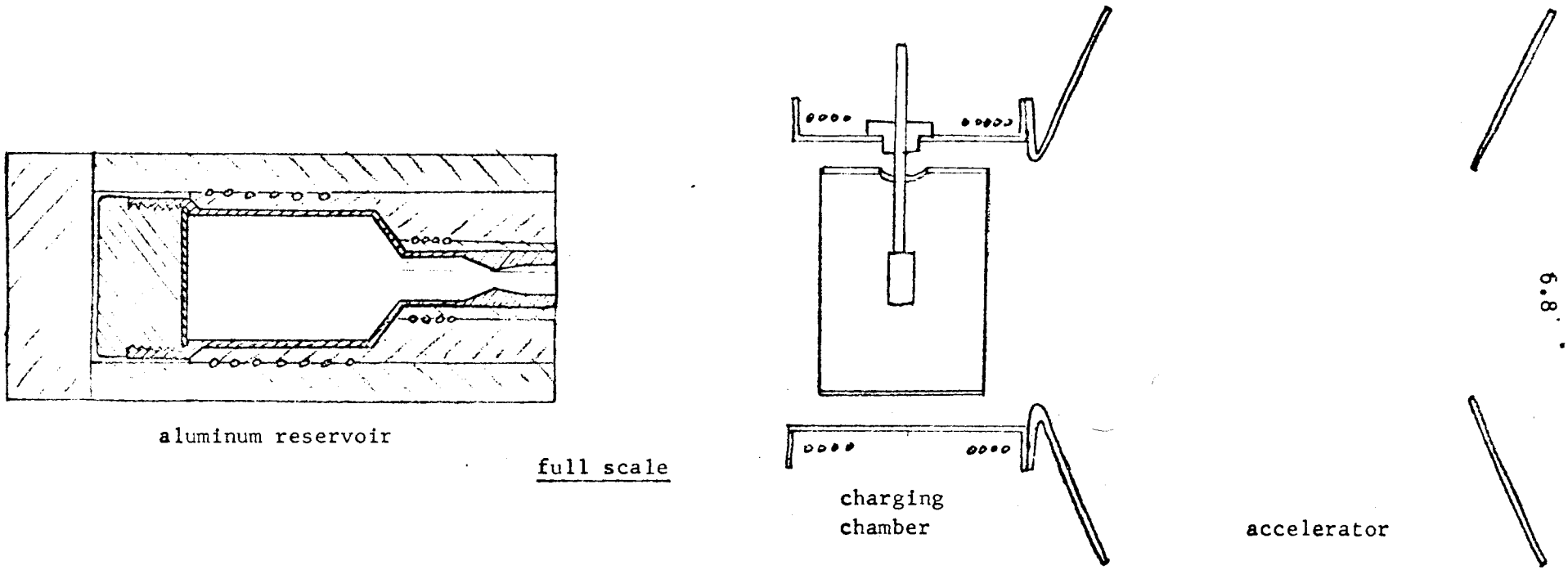

Figure 6.5 - Preliminary design of aluminum colloid thruster. Design parameters: 5 ma beam current, 0.005 atmos plenum pressure, 1800°K plenum temperature, 2.6 mm throat diameter.

ALUMINUM-OXIDE COLLOID FORMATION BY VAPOR-PHASE CHEMICAL REACTION

by S. W. Shin, G. W. Tompkin, Jr., and W. R. Mickelsen

Another possible method for colloid-particle formation in colloid thrusters is by chemical reaction. Of particular interest is the chemical reaction between aluminum vapor and oxygen and/or water vapor. Aluminum would be available from spent tankage, and the oxidant would be available from open cycle life maintainance systems.

Existing theories [1-5] are for homogeneous nucleation and therefore none of them can be applied to the Al-O combustion system, since the vapor state Al_2O_3 does not exist at the limited maximum flame temperature (= b. p. of Al_2O_3). A spectroscopic investigation of Al-O flame shows that the vapors consist of AlO, Al_2O, Al, and atomic oxygen. Therefore, it can be easily seen that the nucleation is achieved through a rather complex reaction among those chemical species. It is also apparent that the condensation is heterogeneous. Courtney[1], in his comments on the nucleation in combustion system, indicated that there has been no quantitative data on nucleation in combustion and that the rate of complex nucleation in a combustion system is only of academic interest at present, because vapor phase chemical reactions preceding condensation will usually be rate controlling.

In the absence of a verified theory, there are two avenues of investigation: experimental and analytical. The history of combustion research teaches that both of these avenues should be pursued simultaneously, and this past experience appears to be fully perti-

nent to the present situation. Research should be done to formulate a theory of heterogeneous nucleation of chemically reacting species. Formulation of this theory should depend to a large degree on information obtained from experiments on chemical-reaction-nucleation of aluminum, water, and oxygen systems.

There appears to be no quantitative data on, nor a theory or model for, heterogeneous condensation nucleation which is predicted in the case of Al-O combustion. A condensation theory will be sought which can explain the product particle size experienced by operation of the above system and various conditions. A very small (50A) particle size is predictable because of the creation of a high degree of supersaturation. A quadrupole mass spectrometer provides a means of determining the distribution of particles.

If the chemical species existing in the burning gases are identified through the spectroscopic method, the flame temperature and the composition at that temperature can be reconciled from thermodynamic calculation.

A quantitative analysis of flame composition needed for the development of a heterogeneous nucleation model results from iteration of equilibrium and enthalpy calculations. The first step is to calculate the composition of the flame gases for an adiabatic flame temperature.

Adiabatic Flame Temperature and Chemical Species

Wolfhard and Parker[6] compared flame temperatures measured by line-reversal and absolute-intensity methods with color temper-

atures. The former methods gave temperatures of about 3273°K, whereas the color temperature was 3873°K for aluminum. The discrepancy was explained by anomalous absorptivity of the small aluminum oxide particles which was found to increase from small values in the visible to unity at about 3000 Angstrom. Based on the value of the aluminum oxide boiling point (3253°K) available at the time of their work, the authors concluded that the true flame temperatures were those determined by the line-reversal and the absolute-intensity methods, whereas the color temperature had no physical significance. In comparison with currently accepted value of aluminum oxide boiling point[7] of 3800°K, the boiling point of aluminum oxide is closer to the measured color temperature (3873°K at 1 atmos.). A plausible explanation might be that the temperature of aluminum flame was reduced below the theoretical maximum by ratiation losses.

In contrast to Wolfhard and Parker, Rautenberg and Johnson[8] identified the color temperature with the true flame temperature. In any case, the flame temperature cannot exceed the oxide boiling point because of the restrictions, i.e. (1) large heat of vaporization of oxide (2) the limited stability of condensed oxide product, that is, oxide begins to decompose significantly at high flame temperature. Therefore, a higher environmental pressure would give a slightly higher flame temperature because of a slightly higher boiling point at that higher pressure and because of lesser decomposition. This occurance of dissociation at high temperature complicates the calculation of theoretical flame temperature. This theoretical temperature to which the flame may rise after the com-

bustion can be calculated from thermodynamic data. It is necessary to know the temperature to be able to calculate the amount of dissociation to get the gas composition, but on the other hand the temperature itself depends on the composition.

The theoretical flame temperature can be obtained on the assumption that there is no heat loss or gain by radiation, thermal conduction, or convection. The first step is to calculate the composition of the flame products for an assumed temperature. The next step is to find the amounts of heat produced by the chemical reaction and heat consumed to heat the flame products of the composition at the assumed temperature from room temperature to the assumed flame temperature. The assumption of flame temperature is repeated until the heat balance between heat production and heat consumption is achieved.

The identification of chemical species existing at the flame temperature is still in doubt. Friedman and Macek in their experimental work of aluminum particle combustion showed the presence of decomposition products, Al, AlO, Al_2O, O, and O_2 at 1 atmosphere. However, Glassman argued the Al_2O species does not exist. In Glassman's spectroscopic investigation of burning aluminum wires in oxygen-inert gas mixtures, all bands and lines on the aluminum flame spectrograms are identifiable as Al, AlO, and impurities, and none can be attributed to Al_2O. The only possiblility that could resolve this disagreement would be for Al_2O to be present as a short-lived intermediate under the condition that aluminum flame experiments are carried out. From a vapor pressure study of aluminum-oxygen system under reducing and under neutral conditions, Brewer

and Searcy[7] concluded that under reducing conditions Al and Al_2O are the principal vapor species while under neutral conditions AlO and O are the principal vapor components. In the reducing conditions, Al_2O_3 is heated with aluminum or another reducing metal. On the other hand, Al_2O_3 is heated alone under the neutral conditions.

Following Glassman and Brewer and Searcy's observations, it can be assumed that one mole of Al_2O_3 (ℓ) dissociates into four moles of the fragments AlO, Al, and 2 [O] upon decomposition. No information is available on the form in which oxygen appears as a dissociation product. The assumption that atomic rather than molecular oxygen is the remaining fragment was made following Ackermann, Thorn, and Winslow[9]. The formation and the decomposition reactions of Al_2O_3 (ℓ) are as follows. Formation of Al_2O_3 (ℓ):

$$2Al\ (g) + \frac{3}{2}\ O_2\ (g) \longrightarrow Al_2O_3\ (\ell)$$

Decomposition of Al_2O_3 (ℓ):

$$Al_2O_3\ (\ell) \longrightarrow AlO\ (g) + 2O(g)$$

At the equilibrium between liquid phase and gaseous phase of burnt products, the number of moles of undecomposed Al_2O_3 (ℓ) is $n(1-\beta)$ whereas the numbers of noles of AlO(g), Al(g), and O(g) are $n\beta$, $n\beta$, and $2n\beta$ respectively. β is defined as the degree of dissociation and n is the total number of moles of Al_2O_3 (ℓ) initially produced by combustion. Then, the sum of moles of each species at equilibrium gives the total number of moles, that is $n(1+3\beta)$ moles.

The adiabatic flame temperature can be found in stages by successive approximation. First trial calculation is attempted using the flame temperature of 3800°K. The equilibrium constant K_p is expressed for the decomposition reaction of Al_2O_3 (ℓ) in terms of the partial pressures of each species:

$$K_p = P_{AlO}\, P_{Al}\, (P_O)^2$$

$$= 4(P_{Al})^4$$

The value $P_{Al} = 8.9 \times 10^{-2}$ atm can be obtained using $\text{Log}_{10} K_p = -3.6$ at T = 3800°K (Figure 1). The partial pressure is proportional to mole fraction and therefore, $P_{Al} = \frac{n\beta}{n(1+3\beta)} \cdot p$ where p is the total pressure.

The degree of dissociation at T = 3800°K thus found from the above relation is $\beta = 0.12$. The numbers of moles of burnt products on the basis of one mole Al_2O_3 (ℓ) formation are as follow:

Burnt Product	Number of Mole
Al_2O_3 (ℓ)	0.88
Al (g)	0.12
AlO (g)	0.12
O (g)	0.24
Total	1.36

It is noted here that the true mole number of burnt products is $n(1 + 3\beta) = 1.36n$, and increase of 0.36 n moles over the mole number of burnt products without decomposition. This directly indicates that the dissociation uses up a significant amount of

energy and limits the flame temperature. The dissociation energy of Al_2O_3 (ℓ) is indirectly determined by the use of thermochemical data.[10]

$$\begin{array}{lll} Al\ (g) + O(g) \longrightarrow AlO\ (g) & & \Delta H^o_{f1} \\ \underline{2Al\ (g) + 3O(g) \longrightarrow Al_2O_3\ (\ell)} & & \underline{\Delta H^o_{fz}} \\ Al_2O_3\ (\ell) \rightarrow AlO\ (g) + Al\ (g) + 2O\ (g) & & \Delta D^o \end{array}$$

Thus, the dissociation energy per mole of Al_2O_3 (ℓ) is $\Delta D^o = \Delta H^o_{f1} - \Delta H^o_{fz} = -119.96 - (-682.55) = 562.59$ Kcal/mole, where ΔH^o_f is the heat of formation from elements in an atomic gas state. The energy consumed upon the decomposition of 0.12 moles (β) of Al_2O_3 (ℓ) is therefore 67.51 Kcal ($= \beta \Delta D^o$). Next to be calculated is how much heat would be required to heat the burnt products from room temperature to T = 3800°K. The heat content of the total true moles of burnt products thus calculated is 135.25 Kcal.

In addition to the heat content of burnt products and to the decomposition energy, heat is also consumed to vaporize aluminum if aluminum is not vaporized prior to chemical reaction and to dissociate the oxygen molecule into oxygen atom. By adding the heat of sublimation of 2Al (77.48 Kcal/mole, reference 11) to the dissociation energy of $\frac{3}{2}\ O_2$ (7.02 eV = 161.7 Kcal/mole, reference 12), the sum of these two values becomes 397.5 Kcal. Therefore, the total heat consumed is 600.27 Kcal on the basis of one mole Al_2O_3 (ℓ) formation.

Next the heat produced in the flame must be determined. The main source of heat liberated is in the formation of Al_2O_3 (ℓ) and is equal to one molar heat of formation of Al_2O_3 (ℓ) from the elements in an atomic gas state (ΔH^o_f = -682.55 Kcal/mole at 3800°K, reference 10) on the same basis as the heat consumed. The value of ΔH^o_f = -682.55 compares with 600.27 Kcal of heat consumtion: Thus the true temperature of the flame, assuming no heat loss, will be higher than 3800°K, and the whole calculation must be repeated for composition at a higher temperature and then the heat balance test must be done and so on until a temperature is found for which the heat consumed is equal to the heat produced in forming a burning mixture with the composition at that temperature.

The computations of compositions of aluminum-oxygen flame at various temperatures and the heat balance computations are summarized in Table I. From the table, it can be concluded that the theoretical adiabatic flame temperature lies near 3930°K. This discrepancy between the reported flame temperature, 3800°K, and the temperature in this calculation, 3930°K, probably results from the extrapolation to high temperatures of thermodynamic data in reference 10. This flame temperature is in a good agreement with the flame temperature of 3908°K in Table II calculated by Fassel. However, the actual flame due to the great emissivity of the particles in the flame.

The thermodynamic data relavent to the calculations in this section are from the literature.[10] The plots of the Gibbs free energy change(ΔG^o_T), the enthalpy change (ΔH^o_T), and the entropy change (ΔS^o_T) against the absolute temperature in Kelvin are shown

in Figures 2, 3, and 4, for the decomposition reaction, Al_2O_3 (ℓ) $AlO(g) + Al(g) + 2O(g)$ based upon the literature[10]. From these figures, the $Log_{10} K_p$ versus T^oK graph is plotted in Figure 1 by the thermodynamic relationship, $Log_{10} K_p = -\Delta G_T^o/2.303\ RT$.

Particle Size Distribution

Fein[14] developed a particle volume distribution equation for aluminum oxide particles resulting from the burning of aluminum metal cylinders through which oxygen is passed. He compared his distribution analysis with the actual distribution of Al_2O_3 product and found excellent agreement. The normalized number average volume distribution function is converted below to a number average mass distribution function and renormalized. The resulting distribution function is then analyzed for ideal thrustor efficiency. The ideal thrustor efficiency analysis method of Mickelsen and Kaufman[15] was used. The indicated efficiency was 30%.

The proceeding efficiency analysis is based on the number average volume (proportional to mass) and the particle size distribution as predicted by Fein and confirmed by a microscopic size analysis. Certain significant model parameters and associated assumptions for Fein's treatment are listed: (1) Complete radial mixing is assumed throughout the chamber except within a thin low-temperature region immediately adjacent to the propellant surface. In the main gas stream, plug flow (no axial mixing) of combustion products is assumed to prevail from the head end of the chamber to the nozzle entrance. (2) Steady state is assumed to to prevail, and the pressure and temperature are constant throughout

the main gas stream. (3) It is assumed that propellant burning rate does not vary with the distance from the head end of the chamber, that the decrease in the moles of gas from condensation of the oxide is small compared to the total moles of gas, and that the chamber diameter does not change significantly with time. Thus, the velocity of the combustion products is directly proportional to the distance from the head end of the chamber. (4) It is assumed that preformed nuclei are introduced into the main gas stream at the constant rate of n_o (nuclei/sec/cm of chamber length). The initial volume of a nucleus is assumed to be constant and is designated by v_o (cm^3). v_o is assumed to be very small compared to the number average particle volume. (5) It is assumed that the rate of growth of a particle is given by the mass transfer law and that the mass transfer coefficient, σ, is independent of particle radius. The mass transfer law is:

$$\frac{dv}{d\theta} = \sigma (C - C_e) \alpha \frac{M}{\rho}$$

where

σ = an empirical rate constant which will be referred to as the growth constant, cm/sec

C = Concentration of the oxide in the gas phase, moles/cm^3

C_e = Equilibrium concentration of the oxide in the gas phase at the chamber temperature and pressure, moles/cm^3

α = Surface area of a single particle assuming that the particles are spherical, cm^2

v = Volume of a single particle, cm^3

M = Molecular weight of the oxide, g/g-mole

ρ = Density of the oxide in the condensed state, g/cm^3

θ = Time, sec

Procedure for Obtaining Improved Ideal Thrustor Efficiency. The physical system to be analyzed for particle size distribution and subsequently compared with experimental results at Colorado State University will differ from the system model of Fein. A promising model expected to produce a much narrower particle size distribution is described below. A central jet of aluminum vapor is enclosed in an annular jet of oxygen or water vapor to produce a flame. This model, in contrast to Fein's, will therefore have a linearly diminishing aluminum or aluminum oxide vapor pressure. The oxygen pressure can be assumed constant throughout the length of the flame and condensation zone. This changes the situation from that listed as Fein's assumption (2). The volume of the particle nucleus divided by the volume of the fully grown particle will be in the range of 1/100 to 1/50, but will still be assumed to satisfy Fein's assumption (4) that the initial volume of particle nucleus is much smaller than the number average particle volume. Other assumptions used by Fein are suitable for the above model for which a new size distribution will be derived prior to experiment.

References

1. Courtney, W. G.: "Recent Advances in Condensation and Evaporation" ARS J. 31, p. 751-756.

2. Frenkel, J.: "Kinetic Theory of Liquids". Dover Publications, Inc., 1955.

3. Christiansen, J. A., Nielsen A.: Acta Chem. Scond. 5 673-675., (1951).

4. Cahn, J. W. and Hilliard, J. E.: "Free Energy of a Nonuniform System. Nucleation in a Two-Component Incompressible Fluids". J. Chem. Phys. Vol. 31, p. 688, 1959.

5. Taylor, H. S., Eyring, H., and Sherman, A.: "Binding Energies in the Growth of Crystal Nuclei from Metallic Atoms". J. Chem. Phys. Vol. 1, p. 68, 1933.

6. Wolfhard, H. G., and Parker, W. G., "Temperature Measurements of Flames Containing Incandescent Particles," Proceedings of Pyhsical Society (London), 62B, pp. 523-529 (1949)

7. Brewer, L., and Search, A. W., "The Gaseous Species of the Al-Al_2O_3 System", Journal of American Chemical Society, Vol. 73, pp. 5308-5314, 1951.

8. Rautenberg Jr., J. H., and Johnson, P. D., "Light Production in the Aluminum-Oxygen Reaction", Journal of American Optical Society, 50, pp. 602-606, June, 1960.

9. Ackermann, R. J., Thorn, R. J., and Winslow, G. H., "Systematic Trends in Vaporization and Thermodynamic Properties of Oxides", Planetary and Space Science, Vol. 3, February, 1961.

10. McBride, B. J., Heimel, S., Ehlens, J. G., and Gordon, S., Thermodynamic Properties to 6000°K For Z10 Substances Involving the First 18 Elements. NASA SP-3001, National Aeronautics and Space Administration, Lewis Research Center, Cleveland, Ohio, 1963.

11. Kubaschewski, O., and Evans, E., Metallurgical Thermochemistry, Pergamon Press Ltd., 1958.

12. International Critical Tables of Numerical Data, Physics, Chemistry, and Technology, National Research Council of the United States of America, Vol. V, McGraw-Hill Book Company, Inc., 1933, pp. 418-

13. Fassell, W. M., Papp, C. A., Hildenbrand, D. L, and Sernka, R. P., "The Experimental Nature of the Combustion of Metallic Powders", Summerfield, M. (ed.), Solid Propellant Rocket Research, Academic Press, New York, 1960, pp. 259-269.

14. Fein, H. L., "A Theoretical Model for Predicting Aluminum Oxide Particle Size Distributions in Rocket Exhausts", AIAA Journal, Vol. 4, No. 1, January 1966, pp. 92-98.

15. Mickelsen, W. R. and Kaufman, H. R., "Status of Electrostatic Thrustors For Space Propulsion," NASA TN D-2172, May, 1964.

TABLE I

THE COMPOSITIONS AND HEAT BALANCE IN $Al-O_2$ FLAME AT VARIOUS ASSUMED TEMPERATURES

TEMPERATURE, °K	3900	3910	3920	3930	3940	3950
$LOG_{10}K_p$	-3.0	-2.9	-2.8	-2.7	-2.6	-2.5
β	0.202	0.222	0.245	0.272	0.303	0.338
COMPOSITION, MOLE						
$Al_2O_3(l)$	0.798	0.778	0.755	0.728	0.697	0.662
Al(g)	0.202	0.222	0.245	0.272	0.303	0.338
AlO(g)	0.202	0.222	0.245	0.272	0.303	0.338
O(g)	0.404	0.444	0.490	0.544	0.606	0.676
HEAT CONTENTS OF PRODUCTS, Kcal	134.51	133.2	131.8	129.9	130.6	128.9
HEAT OF SUBLIMATION OF 2 Al(Kcal)	144.2	144.2	144.2	144.2	144.2	144.2
DISSOCIATION ENERGY OF O_2, Kcal	253.3	253.3	253.3	253.3	253.3	253.3
DISSOCIATION ENERGY OF $Al_2O_3(l)$, Kcal	113.8	125.0	138	153	170	190
TOTAL HEAT CONSUMPTION, Kcal	645.8	655.6	667.2	680.5	698.1	716.4
TOTAL HEAT PRODUCTION, Kcal/1 MOLE Al_2O_3	682.55	682.55	682.55	682.55	682.55	682.55

TABLE II

ADIABATIC FLAME TEMPERATURE OF SOME METALS

$$X\ M(s) + Y/2\ O_2(g)$$

METAL	X	Y	T°K	COMBUSTION PRODUCTS, MOLE FRACTION
Al	2	3	3908	Al=0.064, AlO=0.094, Al_2O=0.209, O=0.366 O_2=0.097, Al_2O_3=0.172*
Mg	1	1	3229	Mg=0.171, MgO=0.484, O=0.053, O_2=0.059, MgO=0.233*
Li	2	1	2846	Li=0.370, LiO=0.041, Li_2O=0.164, O=0.015, O_2=0.075, Li_2O=0.334*
Be	1	1	4210	Be=0.218, BeO=0.033, $(BeO)_2$=0.012, $(BeO)_3$=0.012, O=0.189, O_2=0.014, BeO=0.522*
B	2	3	3786	B_2O_3=0.264, BO=0.500, B_2O_2=0.011, O=0.189, O_2=0.035

*marks denote the condensed phase; all other products are gaseous

Figure 7.1 $LOG_{10}K_p$ versus Temperature, K

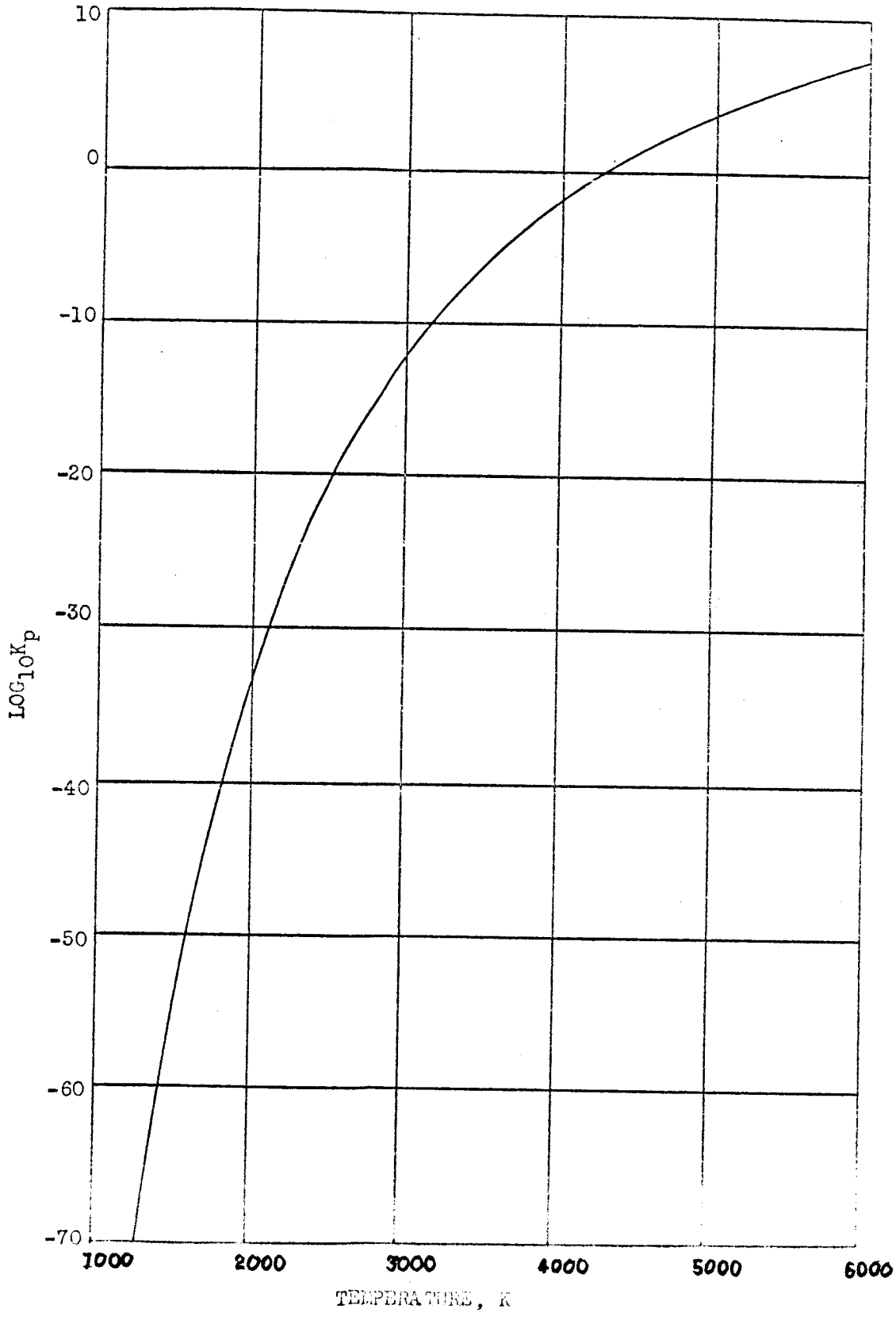

Figure 7.2 ΔG°_{T} versus T°K

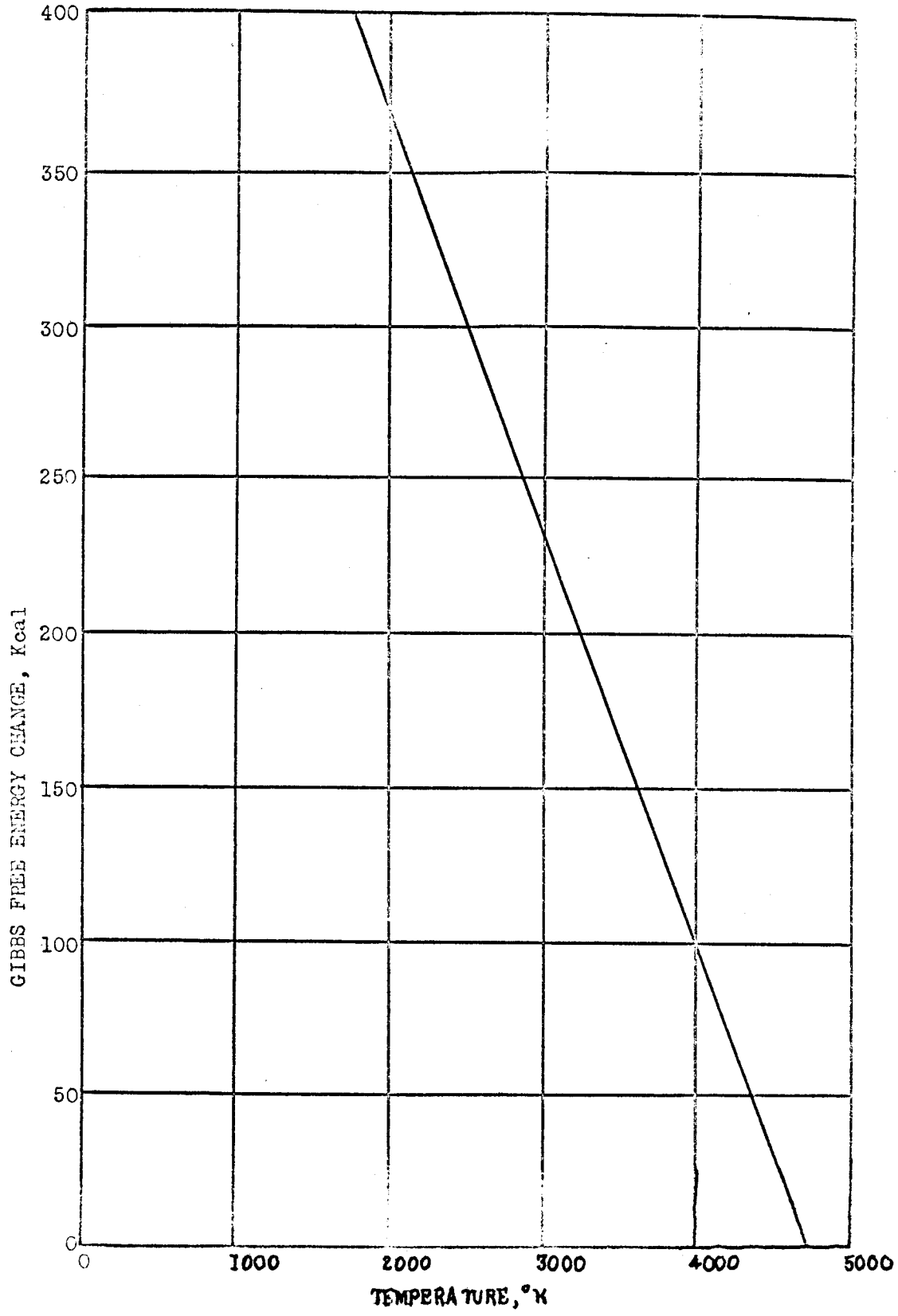

Figure 7.3 $\Delta \dot{H}_T$ versus T °K

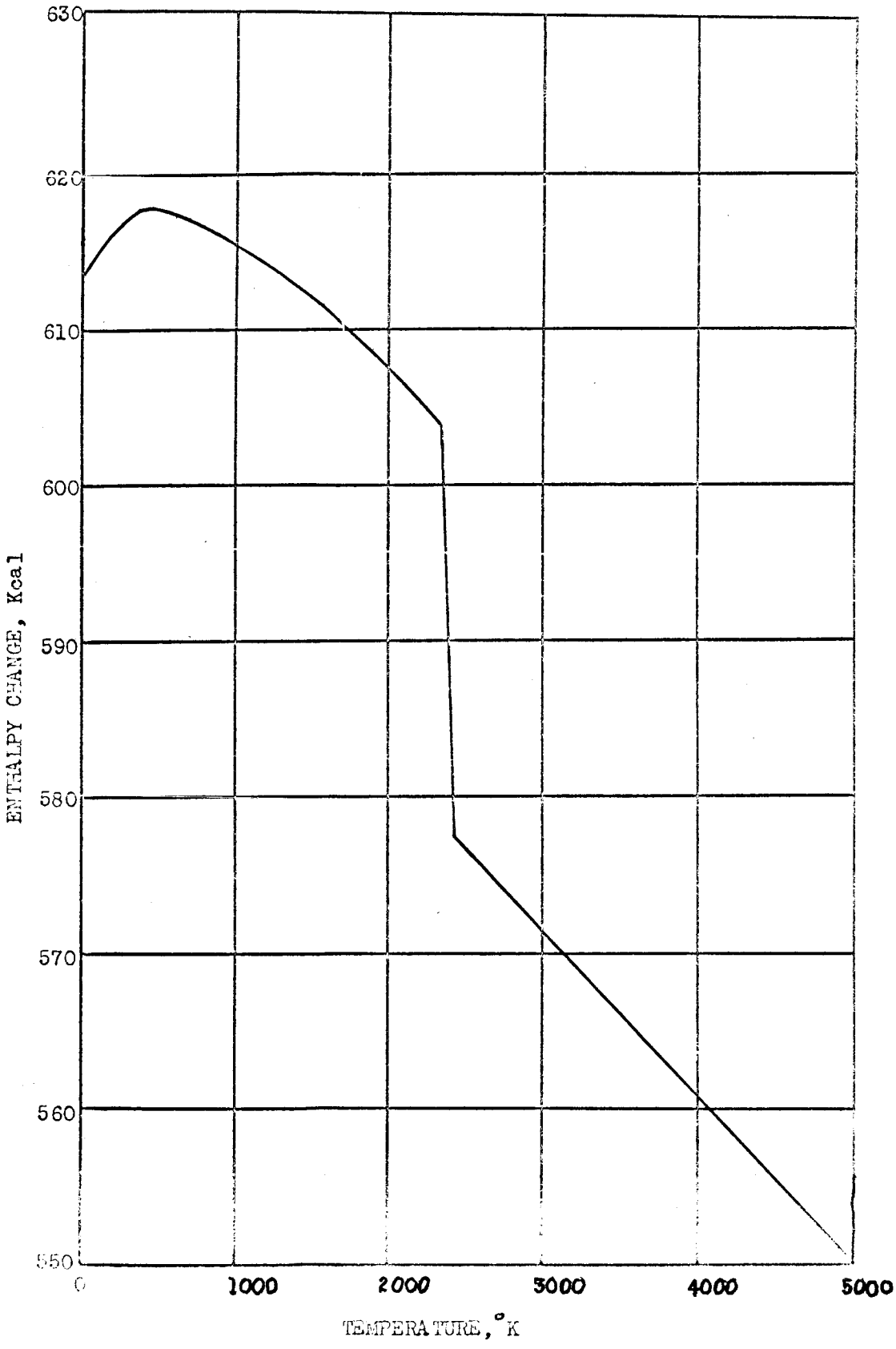

Figure 7.4 ΔS_T° versus $T\,^\circ K$

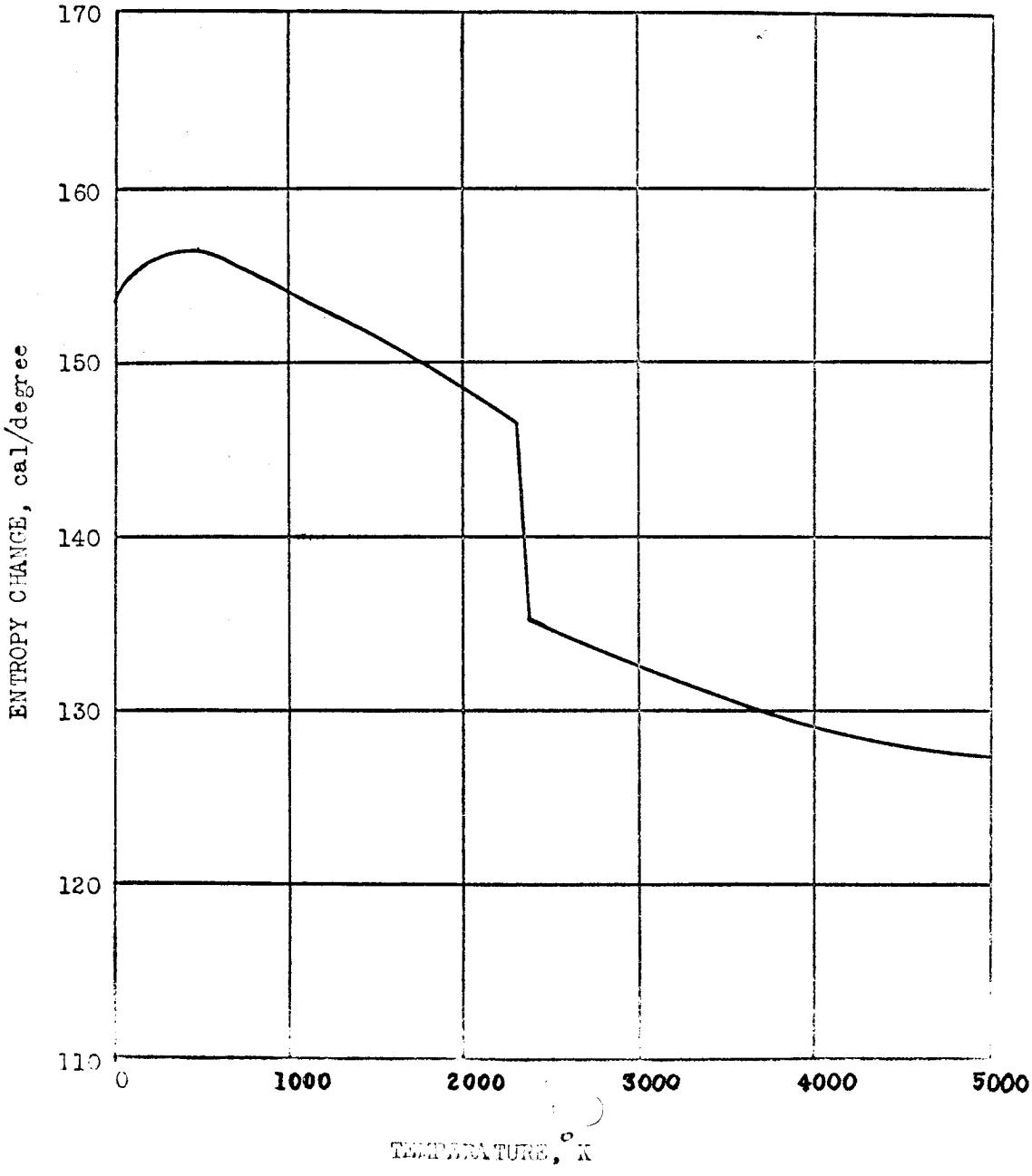

COLLOID PARTICLE FORMATION FROM BIOLOGICAL WASTES

By G. W. Tompkin, Jr.

To provide the characteristics desired in the colloid thruster, the particles must meet certain requirements: (1) at accelerating potentials which can be achieved practically, particles of less than approximately 100,000 amu are required to produce the desired specific impulse,[1] (2) to achieve the promised efficiency of the colloid thruster, the particles must be of narrow size distribution,[1] (3) the production of a monodisperse aerosol of the particles is required, for if any appreciable agglomeration occurs then efforts to satisfy the first two requirements will be negated.

The study described here would investigate the feasibility of the production of colloid particles from organic macromolecules from the standpoint of the three requirements discussed above. The size range of interest can be set somewhat arbitrarily at convenient modal weights between 1000-100,000 amu.

Several factors favor the use of organic macromolecules in the colloid particle thruster. First is the availability of molecules of the appropriate size. For example, insulin (molecular weight 6000 amu), pepsin (molecular weight 35,000 amu) human serum albumin (molecular weight 68,000 amu), and others all have molecular weights within the range of interest. In addition, several proteins are known to exist as distinct polypeptide chains joined only by readily broken chemical bonds (e.g. insulin and α-keratin) or by noncovalent bonds of an as yet undetermined nature (e.g. hemoglobin and probably many other globular proteins[2]). In at least some cases these subunits would be of appropriate size for use in the thruster. It appears

likely that the methods of particle formation proposed here will provide for rather precise control of particle size. Yet another factor favoring the use of organic macromolecules is their possible availability as bio-wastes.

In addition to the use of molecules of the appropriate size, at least three methods exist for the production of particles of the appropriate molecular weight from larger molecules.

The first of these is the chemical rupture of the peptide bonds within the polypeptide chain. This method has the disadvantage that it is less amenable to control of the product size than are the other two. Bovine pancreatic trypsin however, exhibits high specificity for peptide bonds whose carboxyl group is contributed by an arginine or a lysine residue.[3] This method could be employed if a protein were found which had arginine and/or lysine residues spaced at more or less regular intervals along the polypeptide chain separating it into units of the appropriate molecular weight. Enzymic digestion with trypsin would be especially promising if the fragments were of molecular weight of 20,000-25,000 amu, since then the trypsin which has a molecular weight of 23,000-24,000 amu would not have to be separated from the solution, but could be used as part of the propellant.

Insulin is characteristic of the several proteins known to exist as distinct polypeptide chains joined by dissulfide bonds between cystine residues in adjacent chains. Sanger has developed a method for separating these chains (see reference 4 for details). The method is characterized by the rupture of the disulfide bonds through their oxidation to cysteic acid using performic acid as the oxidizing

agent. Once oxidized in this manner, the bond cannot be reformed. Although differing slightly in weight, both polypeptide chains of the insulin molecule have a weight of about 3000 amu.

The hemoglobin molecule which has been extensively studied is representative of the group of proteins composed of distinct chains linked by noncovalent bonds. The exact nature of these bonds is not definitely known. The normal hemoglobin molecule is composed of two identical halves and each half-molecule in turn is composed of two similar polypeptide chains (generally designated α and β in normal hemoglobin). The total molecular weight of hemoglobin is approximately 67,000 amu and that of each chain is about 15,000-17,000 amu. The hemoglobin molecule is observed to sisociate into half-molecules under a variety of conditions, for example, high pH[5,6], low pH[7,8], and the influence of certain chemicals, notably urea and guanidine[5]. In all cases the dissociation is aided by increased dilution and/or the presence of salts. The initial dissociation which takes place rapidly even under mild conditions is completely reversible. However, upon standing or under slightly more severe conditions the dissociation becomes at least partly irreversible, probably due to the denaturation of the protein. Under still more severe conditions (e.g. pH less than 2.5 or guanidine concentrations of 6 moles per liter) a partly irreversible dissociation to the quarter-molecule occurs. In all of the above cases recombination can be retarded or prevented by the application of heat which denatures the protein. From the above it can be seen that the hemoglobin molecule is capable of producing three particles whose weight is within the range of interest.

A method for producing homogeneous, millimicron aerosols from virus particles has been described by Stern et al.[9] Dilute hydrosols of T3 E. coli phage or Type 3 poliomyelitic virus were sprayed through a filtered-air operated glass nebulizer which had been modified to eliminate large droplets. The aqueous droplets were subsequently evaporated, leaving a monodisperse aerosol of the virus particulates. The concentration of the hydrosols was adjusted by dilution with particle-free distilled water until the chance of two virus particulates being present in a single evaporating droplet was about 1 in 100. The size distribution of the aerosols was in close agreement with the previously determined size distributions for the phage and virus. Figure 8.1 shows the size distrubution of a Type 3 poliomyelitic virus aerosol. Special care was taken to remove both soluble and particulate impurities from the hydrosols and to remove suspended matter from the air used in generating the aerosols.

The work done in producing nuclei for cloud seeding indicates that an organic solution or dispersion of organic molecules sprayed into the atmosphere yields many nuclei from each droplet. This would suggest that the amount of carrier fluid which would have to be flashed off per organic macromolecule is small. It is also possible that some types of solvents could remain with the nuclei as a part of the colloid particle.

The use of organic macromolecules in the colloid particle electrostatic thruster appears promising. Existing information shows that it is possible to obtain particles covering the whole range from 1000 to 100,000 amu. A method exists for producing a monodisperse aerosol of the virus particulates, and close control of particle size appears likely.

Experimental investigation of this method of colloid particle formation should proceed directly with apparatus designs based on electrostatic spraying experience.[10]

REFERENCES

1. Mickelsen, W. R., and H. R. Kaufman: "Status of Electric Thrusters for Space Propulsion." NASA TN D-2172. May, 1964.

2. Low, B. W. and J. T. Edsall: "Aspects of Protein Structure," in Currents in Biochemical Research, David E. Green ed., Interscience Publishers, Inc., New York (1956) p. 407.

3. Canfield, R. E. and C. B. Afinsen: "Concepts and Experimental Approaches in the Determination of the Primary Structure of Proteins," in The Proteins, I. Hans Neurath ed., Academic Press, New York (1963) p. 330.

4. Harris, J. I. and V. M. Ingram: "Methods of Sequence Analysis in Proteins," in A Laboratory Manual of Analytical Methods of Protein Chemistry Including Polypeptides, II, P. Alexander and R. J. Block eds., Pergamon Press, New York (1960) pp. 426-427.

5. Kurihara, Kenzo and Kazuo Shibata: "Dissociation of Horse Hemoglobin at High pH," Archives of Biochemistry and Biophysics, 88 (1960) 298-301.

6. Hasserodt, Ulrich and Jerome Vinograd: "Dissociation of Human Caobonmonoxyhemoglobin at High pH," Proceedings of the National Academy of Sciences, 45 (1959) 12-15.

7. Field, E. O. and J. P. R. O'Brien: "Dissociation of Human Haemoglobin," Biochemical Journal, 60 (1955) 656-661.

8. Reichman, M. E. and J. Ross Colvin: "The Number of Submits in the Molecule of Horse Hemoglobin," Canadian Journal of Chemistry, 34 (1956) 411-425.

9. Stern. Sidney C., John S. Baumstark, Alfred I. Schekman, and Richard K. Olson: "Simple Technique for Generation of Homogeneous Millimicron Aerosols," Journal of Applied Physics, 30 (1959) 952-953.

10. Cohen, E., Somol, C. J. and Gordon, D. A.: A 100-kv, 10-w Heavy Particle Thrustor. AIAA Paper No. 65-377. July, 1965.

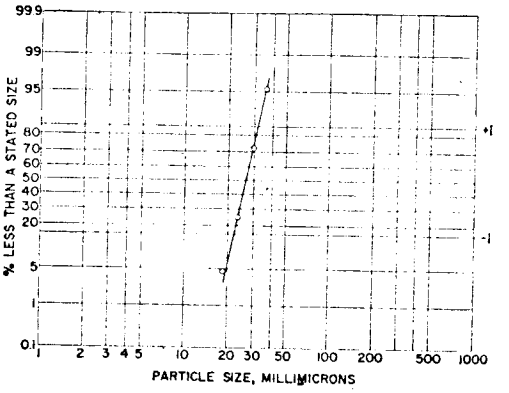

Size distribution of Type 3 poliomyelitic virus aerosol. Number median of 26 mμ with a geometric standard deviation of ± 1.3 mμ. Compares with independently determined average size of 30 mμ for Type 3 poliomyelitic virus.

FIGURE 8.1

PUBLICATIONS

Research done under the Grant has been reported in several publications, and several more papers have been submitted.

Journal and Symposium Papers

Mickelsen, W. R.: Colloid-Particle Electrostatic Thrusters. Presented at DGRR Symposium on Electric Propulsion, West Germany, February 24, 1966. Published in Raumfahrtforschung, Heft 4, Oktober-Dezember, 1966.

Mickelsen, W. R.: Future Trends in Electric Propulsion. AIAA Paper No. 66-595. June, 1966.

Mickelsen, W. R.: Advanced Concepts in Electric Propulsion. To be presented at AIAA Third Joint Propulsion Specialists Conference, July, 1967.

REPORTS

Mickelsen, W. R.: Advanced Electric Propulsion Research. Semi-annual report on NASA Grant NGR06-002-032. Report No. 1, Space Propulsion and Energy Conversion Program, College of Engineering Colorado State University. June, 1966.

Fehr. T. D.: Electric Propulsion for Lunar Missions. M.S. Thesis. Report No. 2, Space Propulsion and Energy Conversion Program, College of Engineering, Colorado State University. December, 1966.

FACILITIES AND EXPERIMENTAL EQUIPMENT

by V.A. Sandborn, J.P. Rybak, and R.L. Moore

During this grant period the NASA-CSU vacuum system has been improved to allow thrustor operation at potential differences up to 300,000 volts. The complete facility was enclosed in a plastic room to provide better control of the atmosphere, see Figure 10.1. Two, 150,000 volt, 5 milliampere power supplies were obtained under the grant. A new control console shown in Figure 10.2 was installed to better handle the high voltage and insure the safety of operating personnel.

A small surplus liquid nitrogen plant was installed during the grant period. This plant should supply sufficient liquid nitrogen for most of the research needs. The system will supply the small amount of nitrogen for the diffusion pump cold trap. It has proven uneconomical to buy small quantities of LN_2 needed to operate the cold trap only. For extensive testing where the LN_2 cryopump liner of the vacuum system is operated over long periods, the output will be supplemented with commercial LN_2. The small plant will supply sufficient nitrogen for filling the cryopump liner inside the facility, however, large heat loads on the liner may require an external liquid nitrogen supply.

Current research in the facility is directed toward the development of the components required in the production and ionization of charged colloidal particles. The first program is in the production and charging of aluminum colloidal particles. A feasibility study of the production of aluminum colloid particles by homogeneous condensation is the main effort in the vacuum facility. Aluminum will be heated to approximately $2000^{\circ}K$ and the vapor passed through a nozzle to accelerate it to supersonic velocities.

In the supersonic flow the rapid cooling produces a condensation shock, which in turn produces aluminum particles. Figure 10.3 is a plot and tabulation of the nozzle contour involved in the first feasibility tests. The nozzle expansion beyond station 6 is expected to be increased to take into account temperature increase due to the formation of colloidal particles.

Due to the extreme high temperature boron nitride will be used for the nozzle and aluminum supply reservoir. At 2000°K it is found that aluminum forms nearly a 50% alloy with the refractory metals. The feasibility study is presently concerned with developing the heater system necessary to operate at 2000°K.

Colloid-Particle Charging

The charging of the colloid-particles can, in theory, be accomplished in many different ways. Some of the possible ways include:[1] (1) negative charging by electron attachment; (2) positive charging by electron bombardment; (3) positive charging by ion attachment; (4) static charging by particle rupture; (5) static charging by contact with surfaces having high surface field strengths; (6) field emission of electrons from particles; (7) field emission of ions from particles; and (8) radiation of particles from a radioactive source. As yet, no one method of particle charging has demonstrated marked superiority.

It has been proposed[2] that the present study should include an investigation of the charging of the colloid particles by electron bombardment. The ionization chamber to be used is basically that of the Kaufman thrustor as described in references 3, 4, 5 and 6.

The ionization chamber, which is presently being constructed is shown schematically in Figure 10.4 and a photograph at the present stage of

development is shown in Figure 10.5. The anode is 5 cm. in diameter and 10 cm. long. The magnetic field windings are designed to provide a non-uniform magnetic field of 30-35 gauss as described in reference 6. The filament-cathode is a piece of tantalum ribbon 2.0 by 0.32 by 0.005 centimeter and is positioned axially at the center of the anode. The colloid-particle beam will pass through the anode region between the axis of symmetry of the anode and the anode wall. This will be done to prevent the colloid particles from impinging upon the filament assembly which would scatter the particles and would probably cause them to break up.

As pointed out in reference 2, the operation of this ionization chamber will be significantly different from that of the Kaufman ion source due to the fact that grossly different particles and particle densities are involved. Consequently, the ionization chamber performance will be investigated as a function of the magnetic field strength, magnetic field shape, anode length and discharge voltage.

Quadrupole Mass Filter

A quadrupole mass filter is being built to be used in the analysis of the beam produced by the colloid thrustor. Such an instrument is very important in evaluating the performance of a colloid thrustor because, as has been previously shown,[3] severe efficiency losses occur if the charge to mass ratio of the particles in the exhaust beam of the thrustor is not constant. Also, the quadrupole mass filter is indispensible as a diagnostic tool for analyzing the operation of the colloid particle generation system as a function of the controllable parameters of the system.

The quadrupole mass filter is based on that described in reference 7. In fact, the physical components are those previously used at NASA

Lewis. New electronics components are being fabricated at CSU. It was designed for a resolution of 10 for particles accelerated through a 14,000 volt potential, a constant r-f voltage of 1050 and operates in the variable frequency mode which allows it to be used over an amu/z range of 10 to 10^9. The maximum design error is 7 percent.

References

1. Norgren, Carl T., "Onboard Colloidal Particle Generator for Electrostatic Engines", ARS Paper 2380-62.

2. Mickelsen, W.R.: Colloid-Particle Electrostatic Thrustors. Raumfahrtforschung, Heft 4, Oktober-Dezember, 1966.

3. Mickelsen, William R. and Kaufman, Harold R., "Status of Electrostatic Thrustors for Space Propulsion", NASA TN D-2172, 1964.

4. Kaufman, Harold R., "An Ion Rocket with an Electron-Bombardment Ion Source", NASA TN D-585, 1961.

5. Kaufman, Harold R., and Reader, Paul D., "Experimental Electron-Bombardment Ion Sources", Program in Astronautics and Rocketry, Vol. 5 - Electrostatic Propulsion, D.G. Langmuir, E. Stuhlinger, and J.M. Sellen, Jr., eds., Academic Press, Inc., 1961, pp. 3-20.

6. Reader, Paul D., "Investigation of a 10-Centimeter-Diameter Electron-Bombardment Ion Rocket", NASA TN D-1163, 1962.

7. Norgren, Carl T., Goldin, Daniel S., and Connolly, Denis J., "Colloid Thrustor Beam Analysis", "Design and Operation of a Suitable Quadrupole Mass Filter", NASA TN D-3036, October, 1965.

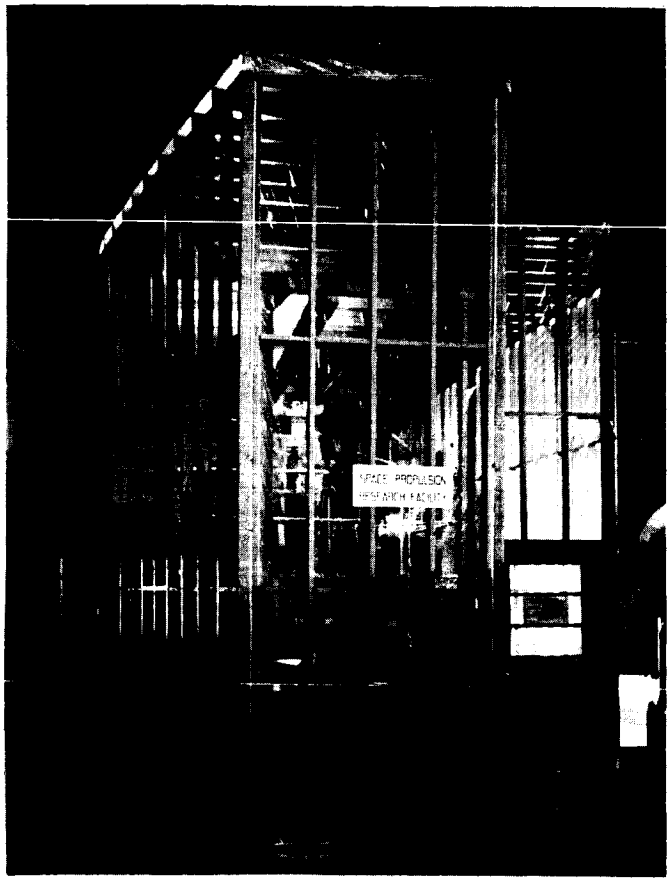

Fig. 10.1 Vacuum facility enclosure.

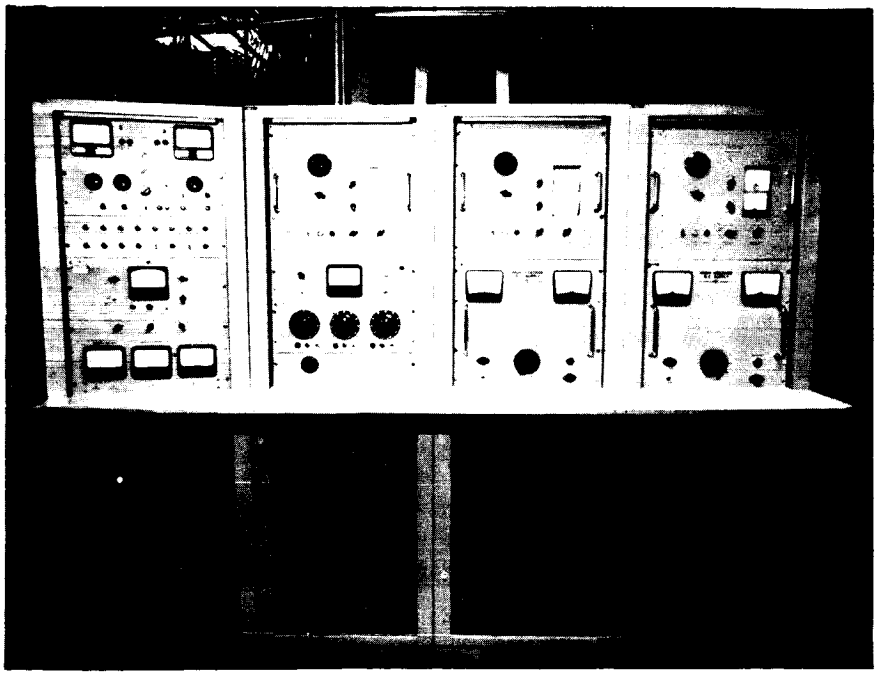

Fig. 10.2 Control and high-voltage console for vacuum facility.

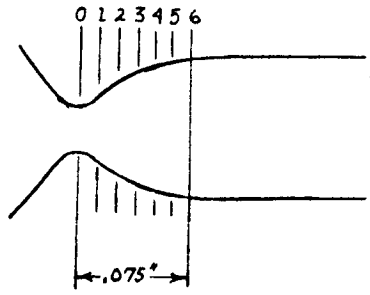

Station	x(inches)	Diameter(inches)
0	0	.066
1	.030	.072
2	.045	.075
3	.054	.076
4	.061	.0765
5	.068	.077
6	.075	.078

Fig. 10.3 Approximate aluminum vapor nozzle dimensions.

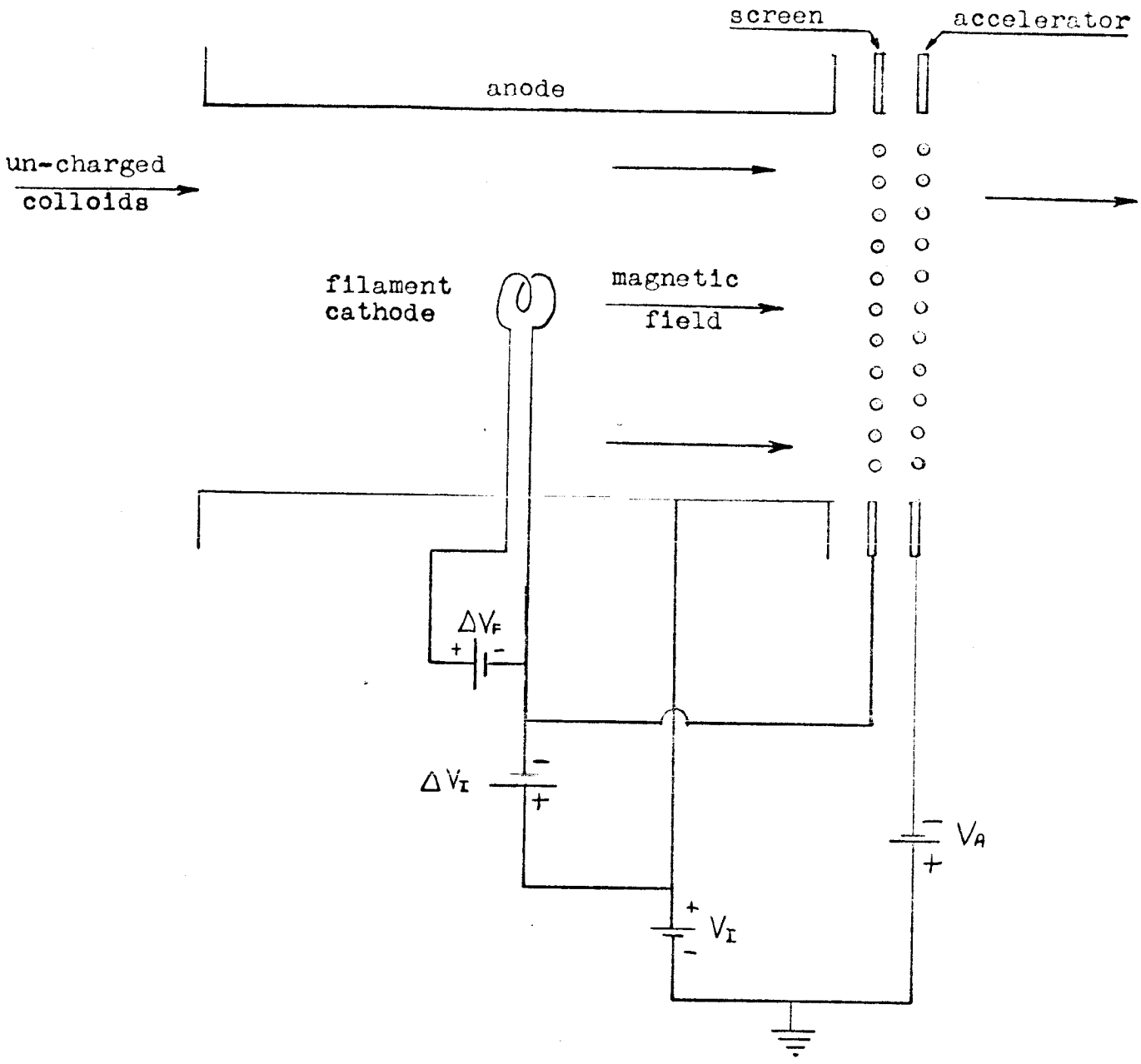

Fig. 10.4 Schematic diagram of ionization chamber.

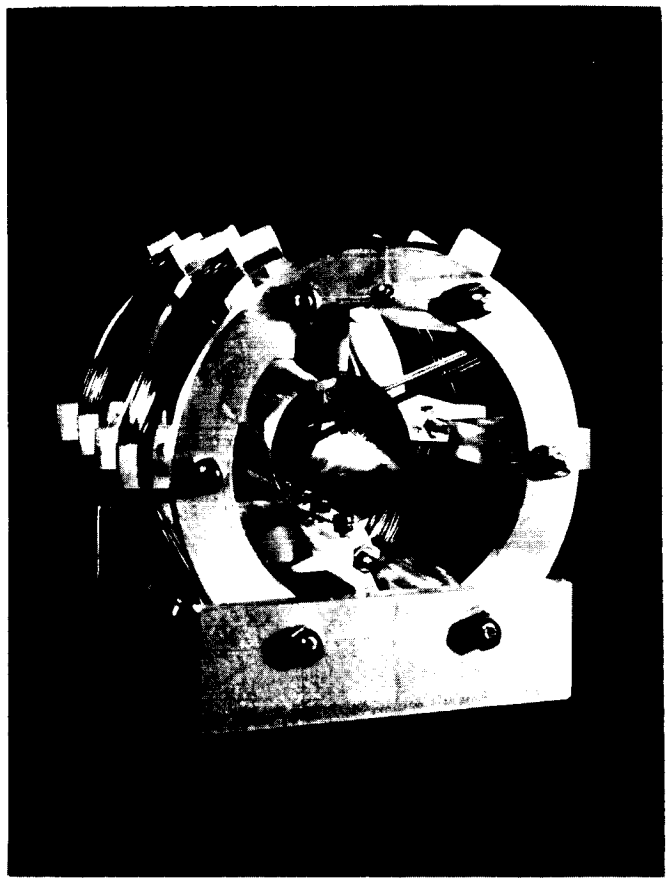

Fig. 10.5 Fabrication status of ionization chamber.

Harry I. Leon, candidate for Ph.D., Mechanical Engineering.

Tentative dissertation topic: electro-colloidal-dynamic power generation for colloid thrusters.

Roger M. Roberge, candidate for Ph.D., Electrical Engineering.

Tentative dissertation topic: ionization of heavy-molecule propellants in electric thrusters.

James P. Rybak, candidate for Ph.D., Electrical Engineering.

Tentative dissertation topic: charging of colloid particles in electric thrusters. Experimental equipment for this research is reported in section 9 of this report.

Vivian Steadman, candidate for Ph.D., Chemistry.

Tentative dissertation topic: colloid particle formation from biological wastes. Preliminary work on this research is reported in section 8 of this report.

Dennis J. Fitzgerald, candidate for M.S., Mechanical Engineering.

Tentative dissertation topic: fundamental performance correlations for electron-bombardment thrusters.

GRADUATE RESEARCH ASSISTANT THESES AND DISSERTATIONS

Graduate students associated with the Grant research program are listed here. One Master of Science Thesis has been completed, and another has received a preliminary review. Thesis and dissertation topics for the other students have been formulated, at least tentatively.

Timothy D. Fehr, candidate for M.S., Electrical Engineering.

Thesis title: "Electric Propulsion for Lunar Missions". This thesis has been completed and has been reproduced as Report No. 2, Space Propulsion and Energy Conversion Program, College of Engineering, Colorado State University.

Mr. Fehr has completed the requirements for the degree of Master of Science, Colorado State University. Mr. Fehr is presently at the Boeing Aircraft Company, Seattle, Washington.

Seong, W. Shin, candidate for M.S., Chemistry.

Thesis title: The Combustion of Aluminum. This thesis has been submitted to his major professor, and has received a preliminary review. Portions of this thesis have been used in section 6 of this report. When completed, the thesis will be reproduced as a Report from the Space Propulsion and Energy Conversion Program.

Daniel C. Garvey, candidate for Ph.D., Mechanical Engineering.

Dissertation topic: electric thrusters with thermal power augmentation. Preliminary work on this research is reported in section 5 of this report.